

Biomimetic Sensor Modeling and Simulations for Flight Control of a Micromechanical Flying Insect

Wei-Chung Wu



Electrical Engineering and Computer Sciences
University of California at Berkeley

Technical Report No. UCB/EECS-2006-53

<http://www.eecs.berkeley.edu/Pubs/TechRpts/2006/EECS-2006-53.html>

May 12, 2006

Copyright © 2006, by the author(s).
All rights reserved.

Permission to make digital or hard copies of all or part of this work for personal or classroom use is granted without fee provided that copies are not made or distributed for profit or commercial advantage and that copies bear this notice and the full citation on the first page. To copy otherwise, to republish, to post on servers or to redistribute to lists, requires prior specific permission.

**Biomimetic Sensor Modeling and Simulations for Flight Control of a
Micromechanical Flying Insect**

by

Wei-Chung Wu

B.S. (University of Maryland, College Park) 1998

M.S. (University of California, Berkeley) 2001

A dissertation submitted in partial satisfaction of the
requirements for the degree of
Doctor of Philosophy

in

Engineering - Electrical Engineering and Computer Sciences

in the

GRADUATE DIVISION

of the

UNIVERSITY OF CALIFORNIA, BERKELEY

Committee in charge:

Professor S Shankar Sastry, Chair

Professor Ronald S Fearing

Professor Kameshwar Poolla

Spring 2006

**Biomimetic Sensor Modeling and Simulations for Flight Control of a
Micromechanical Flying Insect**

Copyright 2006

by

Wei-Chung Wu

Abstract

Biomimetic Sensor Modeling and Simulations for Flight Control of a
Micromechanical Flying Insect

by

Wei-Chung Wu

Doctor of Philosophy in Engineering - Electrical Engineering and Computer Sciences

University of California, Berkeley

Professor S Shankar Sastry, Chair

Inspired by the exceptional flight capabilities of flying insects, the UC Berkeley Micromechanical Flying Insect (MFI) project entails the development of a flapping wing micro aerial vehicle that will be capable of sustained autonomous flight. It has a target size of 25 *mm* wing span and a mass of 100 *mg*. Biological principles are used for actuation, transmission, sensing, and control of the MFI so that the device will exhibit the same performance merits as those observed in real flying insects.

This dissertation first describes the sensing mechanisms used by real insects and then presents formal models of biologically inspired sensory systems including optic flow sensors, angular position sensors, and angular rate sensors. The analysis and simulations of the proposed sensor models suggest the feasibility of using these biomimetic sensors for flight control of a robotic flying insect. It is also demonstrated that a number of insect flight behaviors can be reproduced using simple control schemes based on these sensors. An example of attitude stabilization is given in which a proportional control law using the outputs from the ocelli and halteres as feedback is able to steer the insect toward the upright posture from any initial body orientation and angular velocities.

This dissertation also includes the design of an optic flow sensor, an ocelli sensor, a haltere sensor, and a magnetic field sensor for use on the MFI. Preliminary experimental results of these prototype sensors show promising performance. Compared to existing commercial micro sensors, these devices have the advantages of simple structure, easy implementation, simple signal processing, and low power consumption. Therefore, these sensors are particularly appropriate for micro robotic platforms that have limited computational

resources, little power budget, and small payload capacity.

Dedicated to my parents

Contents

List of Figures	iv
List of Tables	x
1 Introduction	1
1.1 An Introduction to the Micromechanical Flying Insect Project	4
1.2 The Architecture of the Virtual Insect Flight Simulator	9
1.3 Dissertation Outline and Contributions	12
2 Optic Flow Sensors	14
2.1 Hassenstein-Reichardt Correlation Algorithm	17
2.2 Reichardt Motion Sensor Model	17
2.3 Characteristics of Reichardt Motion Sensors	19
2.3.1 Response to Simple Image Motion	19
2.3.2 Robustness to Noisy Stimuli	21
2.3.3 Spatiotemporal Frequency Tuning	22
2.3.4 Image Speed Tuning	24
2.4 Simulations of Insect Flight Behaviors Using Reichardt Motion Sensors . . .	26
2.4.1 Centering Response	28
2.4.2 Regulation of Flight Speed and Visual Odometry	29
2.4.3 Obstacle Avoidance	33
2.4.4 Landing Response and Terrain Following	36
2.5 Elementary Motion Detectors for Obstacle Avoidance	38
2.6 Chapter Summary and Discussion	40
3 Orientation Sensors	43
3.1 Observations of Ocellar Contribution	43
3.2 Ocelli Modeling	46
3.2.1 Orientation Estimation	50
3.2.2 Simulation	54
3.3 Ocelli System Design	61
3.4 Magnetic Field Sensor	63
3.5 Chapter Summary and Discussion	67

4	Angular Rate Sensors	70
4.1	Haltere Morphology	72
4.2	Haltere Modeling	74
4.2.1	Simulation	77
4.3	Haltere System Design	80
4.3.1	Simple Vibrating Haltere	81
4.3.2	Fourbar-actuated Haltere	84
4.4	Attitude Stabilization for the MFI Using Ocelli and Halteres	87
4.5	Chapter Summary and Discussion	90
5	Conclusions	92
5.1	Future Direction	93
	Bibliography	95

List of Figures

1.1	(<i>Left</i>) Artist's conception of future autonomous MFI. Courtesy of R.J. Wood. (<i>Right</i>) Photo of the blowfly <i>Calliphora</i> . Courtesy of W.P. Chan. Also shown are the three sensory systems: compound eyes, ocelli, and halteres whose modeling and simulations will be presented in this dissertation.	4
1.2	The design architecture of the MFI consists of five units: the locomotory unit, the sensory system unit, the control unit, the communications unit, and the power supply unit. Courtesy of L. Schenato.	6
1.3	(<i>Left</i>) Exploded view of the MFI showing the relevant components of the locomotory unit. (<i>Right</i>) Recent two-wing version of the MFI. Courtesy of R.J. Wood.	7
1.4	The VIFS architecture. It can be decomposed into five modules: the aerodynamics module, the body dynamics module, the sensory system module, the control system module, and the electromechanical system module. . . .	10
1.5	Hierarchical control and sensory modality architecture for the MFI.	11
2.1	Resolution of biological eyes and man-made devices. Today's high-end digital cameras have numbers of pixels reaching the level of the human retina. The eyes of flying insects have orders of magnitude fewer pixels. Retina data from [104]; insect data from [52].	15
2.2	One dimensional Reichardt motion sensor and the elementary motion detector (EMD) architecture.	18
2.3	Directional selectivity of the sensor. A stimulus of sinusoidal grating moves along the sensor axis in alternating directions (<i>left</i>). The rightward motion of the stimulus produces a positive output, while the leftward motion of the stimulus produces a negative output (<i>right</i>). Pattern dependent oscillations are observed in the output of a single EMD. Also note the differences between the transient responses and the decay rates at the onset and offset of the stimulus motion.	20
2.4	Directional tuning of the sensor. A sinusoidal grating moves at different angles ϑ relative to the sensor axis. Normalized sensor response is shown and the dashed section indicates negative sensor output.	21
2.5	Snapshots of noisy sinusoidal grating at various levels of SNR (<i>left</i>). Sensor responses to the noisy stimuli (<i>right</i>).	22

2.6	Robust directional discrimination of the sensor under noisy conditions. The curves represent the means of the chattering sensor outputs at various levels of SNR.	22
2.7	Sinusoidal gratings with three different spatial frequencies are presented to the Reichardt correlation sensor. Normalized responses of the sensor as a function of the stimulus speed (<i>left</i>) and as a function of the temporal frequency of the stimuli (<i>right</i>) are shown. It can be seen that the Reichardt correlation sensor is tuned to the temporal frequency of the stimulus.	23
2.8	Spatiotemporal frequency response of the Reichardt correlation sensor. The location of the peak in the spatiotemporal frequency space depends on the parameters of the EMDs.	24
2.9	Contour plot for three correlation detectors, each producing a maximum response at a different spatiotemporal frequency. Detector 3 responds strongly to a high image speed V_3 , Detector 2 responds strongly to an intermediate image speed V_2 , and Detector 1 responds strongly to a low image speed V_1	25
2.10	Half-detector architecture (<i>left</i>). The half-detector produces a strong output for the preferred motion direction and a weak output for the null motion direction. Two half-detectors in an anti-symmetrical configuration can avoid the biased response to the direction of the stimulus movement (<i>right</i>).	26
2.11	Sinusoidal gratings with three different spatial frequencies are presented to the half-detector. The responses are tuned to the stimulus speed (<i>left</i>). However, the sensitivity of the half-detector to the stimulus moving directions ϑ is greatly reduced (<i>right</i>). Different from the output of the standard Reichardt detector, the output of the half-detector is always positive regardless of the direction of the stimulus movement.	27
2.12	The insect flies through a tunnel whose walls carry black and white gratings. When the trajectory of the insect shifts toward either side, one of the insect's eyes would see a higher image motion than that seen by the other eye. Thus, the insect would return to the midline in order to balance the image motion on its two eyes (<i>left</i>). Even when the spatial frequencies of the gratings on the two walls differ by a factor of three, the insect still exhibits this centering behavior (<i>right</i>).	29
2.13	The insect flies through a tunnel whose walls carry gratings that can be made to move in either direction. When the grating on one wall moves in the direction of the insect's flight, the insect's trajectory would shift toward that side (<i>left</i>). However, when the grating moves in the direction opposite to that of the insect's flight, the insect's trajectory would shift away from that side (<i>right</i>). In effect, the insect maintains the balance between the outputs of the two sensors.	30

2.14	The insect regulates its flight speed in a tapered tunnel by holding constant the image speed of the environment. As the tunnel narrows, the insect decreases its speed so as to maintain the same image speed on its eyes. In the section of uniform width, however, the insect flies at a constant speed irrespective of the spatial content of the gratings on the walls. The dashed line at the bottom plot indicates the sensor output if the insect were to fly at a constant speed through the tunnel.	31
2.15	Visual odometry of flying insects. The distance flown by an insect is gauged by the integral over time the motion of the image that is experienced during its journey. The insect, flying at different speeds, travels roughly the same distance when its flight path is straight. However, Distance_1 becomes inconsistent when the flight path is meandered. Moreover, the actual travel distance becomes shorter when the insect flies in a narrower tunnel even though the calculated travel distance remains the same.	32
2.16	The insect flies inside a flight arena whose wall carries a pattern of sinusoidal grating (<i>left</i>). The eyes of the insect see different scenes and hence register different optic flows. The optic flow signals on the left and right eyes are integrated over time (<i>right</i>). When the accumulated signal on one eye exceeds a specified threshold, the insect generates a saccade in the opposite direction in order to prevent a collision into the wall on that side.	34
2.17	The insect initiates saccades at different frequencies dependent on the spatial content on the arena wall. The insect makes turns more quickly when the grating on the wall has a higher spatial frequency (<i>left</i>). The insect makes turns less frequently when the grating on the wall has a lower spatial frequency (<i>right</i>). The circle indicates the initial location of the insect.	35
2.18	The insect initiates saccades at different frequencies dependent on the specified threshold for the time-integrated optic flow signals. The insect responds quickly to the rising optic flow signal and generates turns more frequently if the threshold for the accumulated sensor output is set to a smaller value (<i>left</i>). If the threshold is increased to a larger value, the insect has a slower response and hence generates turns less frequently (<i>right</i>).	36
2.19	The insect releases a landing response when the time-accumulated optic flow signal exceeds a threshold. The insect decelerates such that the perceived optic flow reduces quickly as it approaches the landing site.	37
2.20	The insect follows the topography of the terrain based on the perceived optic flow during its flight. The insect ascends when the accumulated signal exceeds an upper threshold and descends when the accumulated signal drops below a lower threshold. As a result, the insect is able to maintain a fairly constant distance above the ground.	38
2.21	Photo of the EMDs consisting of a two-by-two photodiode array (<i>left</i>). Test setup for the EMDs to a simulated obstacle (<i>right</i>). A black stripe on a white background is moving toward the EMDs, mimicking an approaching object.	39
2.22	Signals registered by the individual photodiodes as the black stripe approaches the EMDs (<i>left</i>). The resulting optic flow measurement by the EMDs (<i>right</i>).	40

3.1	Ocelli of the blowfly <i>Calliphora</i> . (<i>Left</i>) Upper part of the head viewed from the front with a pair of large multi-faceted compound eyes at either side and three simple eyes (ocelli) arranged in a triangle on top of the head between the compound eyes. Courtesy of D.A. Kendall; http://www.kendall-bioresearch.co.uk/ . (<i>Right</i>) The stippled areas represent the visual fields of the median ocellus (top) and right lateral ocellus (bottom) in a blowfly. On the left is represented the part of the visual field within the anterior hemisphere, and on the right the part in the posterior hemisphere. Adapted from [80].	44
3.2	(<i>Left</i>) Four photoreceptors, P_1, P_2, P_3 , and P_4 , are fixed with respect to the insect's body frame (x^b, y^b, z^b) . The shadowed area, A_3 , represents the receptive field of P_3 . (<i>Right</i>) The projection of the light source onto the $x - y$ plane of the insect's body frame. The shadowed area represents the region enclosed by the inequalities in Equation (3.10).	47
3.3	Light intensity distributions over the celestial sphere: indoor environment (<i>top</i>), urban environment (<i>middle</i>), and open space environment (<i>bottom</i>). Data is obtained from the measurements using a single photodiode, shown in Figure 3.12, faced at different orientations. The plots on the right hand side are generated by interpolating (but not smoothing) the light intensity data on a uniform grid of 100 points collected at locations marked by "X" in the pictures on the left hand side.	49
3.4	Longitude estimation error, $\Delta\psi^b = \psi^b - \hat{\psi}^b$, and the magnitude of the ocellar output vector, $\ \mathbf{y}_O\ $, as a function of the latitude θ of the light source position relative to the insect body for the light intensity $I(\theta) = \cos^5(\theta)$. Each trace corresponds to a different longitude ψ . The thick line in the lower plot is given by the function $f = a \sin \theta^b$ in Equation (3.11).	54
3.5	Light intensity distributions and the corresponding force fields relative to the insect's body frame induced by the ocellar outputs. The force field is uniform for the light intensity function $I(\theta) = \cos \theta$ (<i>upper plots</i>). However, the magnitude and direction of the vectors vary for the light intensity function $I(\theta) = \cos^5 \theta$ (<i>lower plots</i>).	56
3.6	Induced force fields for different light intensity distributions: indoor environment (<i>top</i>), urban environment (<i>middle</i>), and open space environment (<i>bottom</i>). The plots on the right hand column show the close-up view around the brightest region in each case. The light intensity distributions in these real world environments are the same as those shown in Figure 3.3.	57
3.7	Light intensity $I(\theta) = \cos \theta$ with random noise at SNR = 0 dB (<i>upper left</i>), and the light intensity profiles at adjacent longitudes (<i>upper right</i>). The dashed line in the plot represents the noiseless intensity profile. The induced force field under the noisy condition (<i>lower left</i>), and a close-up view of the field from the north pole (<i>lower right</i>). The circle represents the region of convergence in which vectors inside this circle essentially point to random directions.	58

3.8	The response of an ocelli sensor to multiple light sources. The sensor produces only weak output when it is far away from the light sources. However, when the sensor is in the neighborhood of the light sources, it produces strong response due to the unequal illumination of the photoreceptors. Therefore, the insect would be attracted toward the bright region according to the ocellar outputs. The left plot shows the light distribution generated by two light sources. The asterisks in the right plot indicate the positions and relative brightness (3:1) of these two light sources.	59
3.9	Snapshots of an insect being attracted toward the light source according to the output from the ocelli sensor. The trajectory of the insect is generated by the VIFS.	60
3.10	Schematic of the ocelli system design (<i>left</i>). Each face of the pyramidal structure contains one photodiode. The output voltages from these photodiodes are subtracted pairwise to give the two ocellar outputs. Photo of a prototype ocelli (<i>right</i>).	61
3.11	Sensitivity of the ocelli system. The ocelli sensor is allowed to move in a 6×8 cm region centered at the origin. The y_1^o (<i>left</i>) and y_2^o (<i>right</i>) measurements of the ocelli structure with $\alpha = 40^\circ$	62
3.12	Customized photodiode containing two receptive areas of different sizes (<i>left</i>). The desired signals of either regions can be obtained directly from the corresponding built-in resistors. The miniaturized ocelli structure using the customized photodiodes (<i>right</i>).	63
3.13	(<i>Left</i>) The setup for ocelli verification. Courtesy of R.J. Wood. The ocelli structure is rotated around one axis only and the signals from the pairwise photodiodes are recorded. (<i>Right</i>) The individual photodiode signals (broken lines) and the resulting ocellar output (solid line) in one dimension.	64
3.14	Schematic of the magnetic field sensor design (<i>left</i>). Photo of the prototype magnetic field sensor with three metal loops (<i>right</i>).	65
4.1	Halteres of the blowfly <i>Calliphora</i> . There are about 335 campaniform sensilla embedded in the haltere joint to detect the Coriolis force exerted on the haltere. During flight the halteres beat up and down through an angle of approximately 180° anti-phase to the wings at the wingbeat frequency. Adapted from [62].	71
4.2	Components of the force acting on the haltere during flight.	72
4.3	The roll, pitch, and yaw axes of the fly. The force acting on the haltere can be decomposed into three components: the lateral force is orthogonal to the haltere stroke plane, the radial force is along the longitudinal axis of the haltere, and the tangential force is in the direction of the instantaneous haltere motion.	73
4.4	Coriolis force signals for rotations about the roll, pitch, and yaw axes.	74
4.5	Demodulation scheme of haltere forces. The roll, pitch, and yaw angular velocities are decoupled by utilizing the phase, frequency, and modulation of the left and right Coriolis force signals. The box integrators average out the periodic disturbances caused by wing rotational motion.	77

4.6	Simulation of angular velocity detection by halteres. The insect is under hovering flight mode (<i>top</i>) and recovering from the upside down orientation (<i>bottom</i>). The halteres are beating off the stroke plane of the wings and therefore the lateral directions of the halteres are not orthogonal to the wing stroke direction. It can be seen that the halteres detect false signals as a result of the common-mode body oscillations due to wing motion.	78
4.7	Simulation of angular velocity detection by halteres. The insect is under hovering flight mode (<i>top</i>) and recovering from the upside down orientation (<i>bottom</i>). The halteres are beating in the stroke plane of the wings and therefore the lateral directions of the halteres are orthogonal to the wing stroke direction. Compare to Figure 4.6, the common-mode error due to wing motion is greatly reduced.	79
4.8	Schematic of the simple vibrating haltere (<i>left</i>). Photo of the completed haltere with half bridge strain sensor and its wires (<i>right</i>).	82
4.9	Test setup for the simple vibrating haltere (<i>left</i>). Angular velocity detection by the simple vibrating haltere (<i>right</i>).	83
4.10	Schematic of the fourbar actuated haltere. Courtesy of R.J. Wood.	84
4.11	Photo of the completed fourbar actuated haltere.	86
4.12	Angular velocity detection by the fourbar actuated haltere (<i>left</i>). Zoomed in to show accuracy (<i>right</i>).	86
4.13	Simulation result of insect dynamics using control law (4.13). It can be seen that the insect stabilizes toward the orientation of the light source (i.e., $\theta_z = 0$ and $\boldsymbol{\omega} = [0, 0, 0]^T$).	89

List of Tables

1.1	Relevant parameters of the blowfly <i>Calliphora</i> and the MFI. Data adapted from http://robotics.eecs.berkeley.edu/~ronf/MFI/index.html	5
2.1	Summary of the visual sensing schemes in the simulations of the insect flight behaviors.	41
3.1	Design specifications of a magnetic field sensor using copper as the material. Fixed parameters are on top and optimized variables are at bottom.	67
4.1	Comparison of the fourbar-actuated haltere to commercially-available silicon micromachined angular rate sensors.	91

Acknowledgments

First I would like to thank my family, especially my parents. As a person with physical disabilities, getting education has never been easy. For the past fifteen years, from Taiwan to the United States, from my undergraduate study at the University of Maryland to my graduate study at UC Berkeley, my mother has always been staying with me taking care of my daily activities. My parents have shared the difficulties and challenges I have faced as I pursued higher education. Despite these frustrations, they have never lost faith in me. Their unconditional love and patience are definitely my greatest support and have encouraged me to go forward. I would certainly attribute to them for anything that I could possibly achieve.

I would also like to thank my research advisor, Professor Shankar Sastry. His guidance and support have been nurturing my graduate study and opening up my vision in the exciting research fields. I also thank Professor Ronald Fearing for his valuable comments regarding this work and Professor Kameshwar Poolla for reading this dissertation.

Many people have contributed to this work, as well as enriched my academic experience. I will definitely remember the time I spent with my partners, Luca Schenato and Xinyan Deng. For years, we have worked together in the development of the Virtual Insect Flight Simulator. I am especially grateful to Luca who has been more than generous in offering his ideas and suggestions regarding many aspects of this work. His enthusiasm in the project and sharing of his knowledge with me made this achievement possible. Thanks are also given to my colleagues in the MFI group, Robert Wood, Joseph Yan, Srinath Avadhanula, and Metin Sitti. Rob has contributed much to constructing and testing the sensors presented in this dissertation. I also want to express my thanks to Cedric Ma, Lance Tammero, and all those people whose names are not listed here for their assistance and helpful discussions on the subject matter.

Finally, I want to thank all my friends, faculty and staff in this department, and those who had helped me in any aspect. Their friendliness and kindness have created a supportive environment and made my life at Berkeley a truly rewarding one.

Chapter 1

Introduction

The development of unmanned aerial vehicles (UAVs) has been an active area of research during the past several decades because they are indispensable for various applications where human intervention is considered difficult or dangerous. UAVs are remotely controlled or autopilot aircraft that can carry cameras, sensors, communications equipment or other payloads. They have been used mainly in military operations, such as reconnaissance, communications relay, and intelligence-gathering missions, since the 1950's. At the tactical level, UAVs can provide their users with instantaneous video and radar images of a target. At the strategic level, they have some advantages over reconnaissance satellites such as being able to monitor one area for an extended period of time. Between 1964 and 1998, the U.S. Department of Defense has developed eleven different UAVs, only three entered production ¹. Many of those development programs were canceled due to technological immaturity and high cost of acquisition and deployment in early years. Nevertheless, the development of UAV systems has gained momentum since the late 1980's because of the advances in technology and in the near future they are expected to take part in more challenging operations, some of those including combat missions (e.g., they can be used in electronic warfare and air strike missions).

Although UAVs have been proven to be a safe means to carry out many missions, their use in some tasks is limited by their size and maneuverability. Additionally, enabling technologies in the recent past allow the creation of many small scale devices which have

¹Pioneer (1986 – 2003) has retired, Hunter (1988 – 1996) was terminated after low rate initial production, Predator (1994 – present) has been deployed, and Global Hawk (1994 – present) and Shadow 200 (1999 – present) are in production. Sources: Congressional Budget Office, <http://www.cbo.gov/showdoc.cfm?index=917&sequence=0>; U.S. Department of Defense, <http://www.defenselink.mil/specials/uav2002/>

performance comparable to that of their large scale counterparts. These have motivated the development of miniaturized UAVs, termed micro aerial vehicles (MAVs). According to the requirement specified by the U.S. Defense Advanced Research Projects Agency (DARPA), the size of an MAV can not exceed 15 *cm* in any dimension [56]. Because of the small size, MAVs offer the advantages of being able to move through small passage and operate in small space, greater agility in flight, and portability. Also they have low cost of fabrication and can be operated with limited resources. Therefore, MAVs may be deployed in a large quantity in an operation and they are generally considered expendable. The applications envisioned for MAVs include search and rescue within collapsed buildings, inspection of sites containing hazardous material, and security monitoring in addition to many of the applications identified for UAVs.

Despite the remarkable achievements obtained with the development of larger aircraft, the development of MAVs is still a challenging task. Directly scaling down the design of larger aircraft will not create an MAV because factors that are not of major concerns for the operation of macro-scale aircraft may have significant effects on the operation of micro-scale aircraft. For example, an important consideration in the design of MAVs is that they are operated in the aerodynamic regime of small Reynold's numbers (the Reynold's number is defined to be the ratio of inertial to viscous forces of a fluid flow). This means that the surrounding air feels like a viscous fluid to the wings of an MAV and drag forces from the air become more dominant players in affecting the aerodynamics of the MAV. In order to increase the lift-to-drag ratio, the wings of an MAV need to have a higher velocity relative to the air. This, in effect, puts greater demands on the propulsion system of the aircraft. Furthermore, as the size of a device is reduced, frictional forces between moving parts of the device will have increasing influences on the performance of the system due to the increased percentage of contacting surface area. Therefore, mechanical components such as joints, bearings, and electromagnetic motors become less feasible for micro robots on the centimeter scale for reasons of efficiency.

Since it is not possible to meet all of the design requirements of an MAV system with current technology, research is proceeding. To date, a number of prototyped MAVs has been developed and many of them have demonstrated stable flight for limited duration. AeroVironment, Inc. built the Black Widow, a six-inch fixed wing MAV, which can fly at 30 *mph* with an endurance of 30 *min* [33]. This company also made a prototype of a vertical take-off and landing (VTOL) MAV, called Hoverfly VTOL, which has a hover endurance of

7 *min* and a cruise endurance of 13 *min*. A group at Drexel University is developing a light weight (26 *g*) indoor flying robot [34]. Although its 46 *cm* wing span is large compared to the 15 *cm* specification, this flyer is capable of very slow flight at 2 *m/s* and has a turning radius of 2.5 *m*. Thus, it is suitable for operations in urban and some enclosed environments. Kroo at Stanford University is leading a project aimed at creating a very small rotary wing MAV called the Mesicopter [50]. This rotocraft, with dimensions of 2.5 *cm* and a weight of 3 *g*, consists of four motor-rotor assemblies mounted on an airframe. Prototypes of Mesicopter showed the ability to generate sufficient lift force to carry the airframe and battery. Engineers at the University of Maryland at College Park are constructing a class of rotary wing MAVs with either a single or coaxial counter-rotating rotors [10, 84]. Their prototypes have a hover endurance of several minutes.

Except the Mesicopter, almost all of the current fixed and rotary wing MAVs have dimensions exceeding or reaching the upper bound of the 15 *cm* specification. It is believed that the best solution to building even smaller MAVs may come from nature where many flyers of centimeter size exist. Throughout creation, animals that are capable of initiating lift-generating flight do so through the flapping of wings. The reason for wing flapping as a universal means of biological flight propulsion may be related to the scale. A flapping wing design relies on lift generated by airflow created by both vehicle speed and wing flapping to support the weight of the vehicle. If the scale is reduced, the frequency of wing flapping can be increased without affecting the minimum velocity of the vehicle. Thus, this design is inherently forgiving to scale changes. In an attempt to imitate the flight mechanisms used by flying animals, several groups have worked on MAV platforms using flapping wings. Cox *et al.* at Vanderbilt University built a flapping wing device which mimicked the functionality of a dragonfly using piezoelectrically actuated wings [18]. Michelson at Georgia Tech developed an entomopter using a chemically actuated mechanical muscle to drive its wings [58]. Researchers at the California Institute of Technology, UC Los Angeles, and AeroVironment created an ornithopter, called the Microbat, using an electromagnetic motor to generate wing motions [67, 68]. Another ornithopter developed by SRI International uses electrostrictive polymer actuators to drive its wings [43].

The Micromechanical Flying Insect (MFI) at UC Berkeley is another miniature ornithopter under development. Inspired by the superior flight capabilities of flying insects, the MFI is modeled entirely upon typical two wing flies. It has a target size of 25 *mm* wing span and a mass of 100 *mg*. An autonomous robotic flyer at this size scale will provide

exceptional maneuverability. Also, biological principles are used not only for actuation but also for sensing and control of the MFI so that the device will achieve similar performance merits observed in nature. Therefore, it is important to establish an understanding of insect morphology both from a functional aspect and from an evolutionary point of view. While the final goal of the MFI project is to create a robotic flying insect capable of sustained autonomous flight, current work has been focusing on the development and integration of major components of the system including actuators, thorax, wings, biologically inspired sensors, and control algorithms.

1.1 An Introduction to the Micromechanical Flying Insect Project

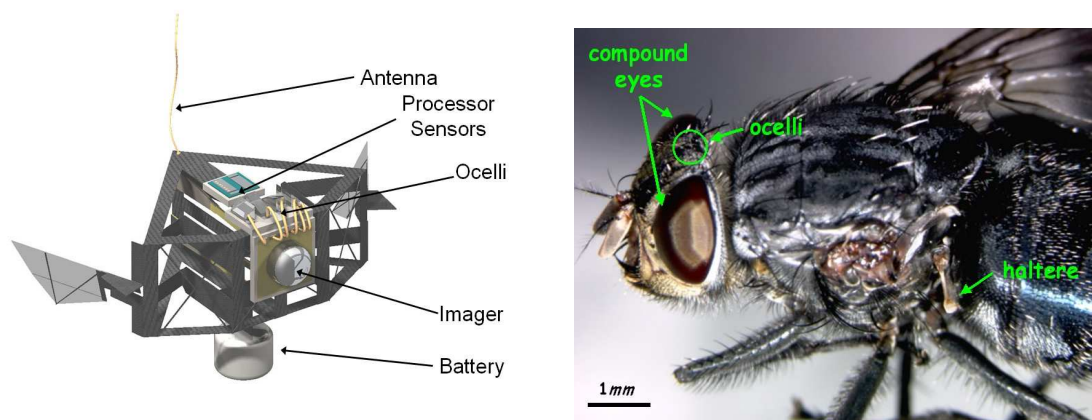


Figure 1.1: (Left) Artist's conception of future autonomous MFI. Courtesy of R.J. Wood. (Right) Photo of the blowfly *Calliphora*. Courtesy of W.P. Chan. Also shown are the three sensory systems: compound eyes, ocelli, and halteres whose modeling and simulations will be presented in this dissertation.

The blowfly *Calliphora erythrocephala* (order Diptera) is used as a design target for the MFI since it is large enough for relatively easy assembly of actuators, thorax, wings, and on-board electronics (see Figure 1.1). A set of the relevant parameters of the *Calliphora* and the MFI is given in Table 1.1. Wings of dipterous insects have three degrees of freedom: flapping, rotation, and out-of-stroke-plane motion. It is known that insect flight can not be explained by steady state aerodynamics, and this led to the elucidation of non-steady state aerodynamics which account for the large lift force generated by insect wings [21, 25].

Parameter	Blowfly	MFI
Mass (mg)	100	100
Wing length (mm)	11	10
Actuator	muscle	piezoelectric
Actuator mass (mg)	50	50
Actuator power (mW)	10	12
Wing power (mW)	5	10
Wing inertia ($mg\text{-}mm^2$)	20	20
Quality factor (Q)	1 – 3	2
Resonant frequency (Hz)	150	150
Wing stroke (deg)	160	120
Wing rotation (deg)	120	90

Table 1.1: Relevant parameters of the blowfly *Calliphora* and the MFI. Data adapted from <http://robotics.eecs.berkeley.edu/~ronf/MFI/index.html>.

Using a dynamically scaled model of *Drosophila* wings, known as the Robofly which can closely mimic the wing stroke kinematics of most flying insects, Dickinson *et al.* [21] were able to identify the three key aerodynamic mechanisms used by flying insects: delayed stall, rotational lift, and wake capture. The delayed stall occurs at the onsets of the translational phases (upstroke and downstroke) of the wing stroke and lasts for a distance of a few wing chord lengths. During this mode, large lift is produced at large angles of attack due to the growth of a leading edge vortex on the wing [25]. The rotational lift is the result of simultaneous wing translation and rotation. This mode is similar to the Magnus effect in which a spherical object simultaneously spinning and translating would experience a force perpendicular to both the velocity vector and the axis of rotation [5]. It occurs at the ends of upstroke and downstroke when the wing decelerates and rotates. The wake capture occurs

during the stroke reversal when the wing collects the kinetic energy which was imparted to the fluid in the wake from the previous half stroke. Since these three modes of force generation can be realized by wing flapping and rotation, the MFI wings will need only two degrees of freedom to exploit the unsteady aerodynamics. The out-of-stroke-plane motion does not appear to contribute much to the lift generation [105]. It may, however, have a significant effect on the maneuverability.

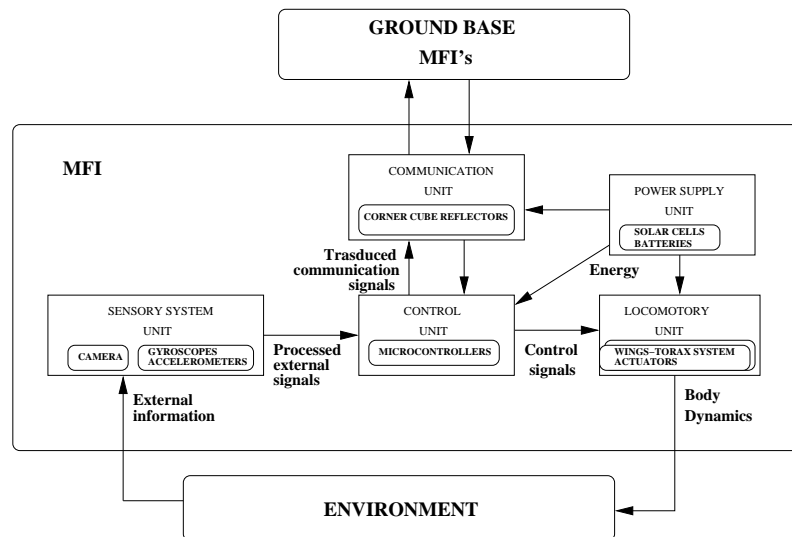


Figure 1.2: The design architecture of the MFI consists of five units: the locomotory unit, the sensory system unit, the control unit, the communications unit, and the power supply unit. Courtesy of L. Schenato.

Figure 1.2 illustrates the design architecture of the MFI. It is possible to identify five main units, each of which is responsible for a distinct task: the locomotory unit, the sensory system unit, the control unit, the communications unit, and the power supply unit. The locomotory unit of the MFI consists of piezoelectric bending actuators, thorax, and polymer wings [28]. The actuators are analogous to the flight muscles of real insects. However, the displacement generated by piezoelectric actuators is too small with respect to the desired MFI wing motion. In order to transform the small actuator deflection into large stroke amplitude and wing rotation, a flexural fourbar mechanism is used. The fourbar accepts a rotary input and yields an amplified rotary output. Furthermore, a slider-crank mechanism is used to convert the approximately linear motion of the actuator to a rotation at the input link of the fourbar mechanism. For each wing, two actuators, fourbars, and slider-cranks are used. Effectively, such a two-stage mechanical amplification technique can

convert the $\pm 1^\circ$ motion range of the two actuators to the $\pm 45^\circ$ wing rotation and $\pm 60^\circ$ wing flapping. Moreover, the two fourbars drive a wing differential in such a way that one controls the leading edge while the other controls the trailing edge of the differential element [28, 113]. The wing has pure flapping when both fourbars move in phase, and the wing rotates when there is a phase difference between the two fourbars. Two of this compound kinematic mechanism are symmetrically arranged to form the thorax of the MFI. Figure 1.3 shows the relevant components of the locomotory unit and the completed two-wing version of the MFI.

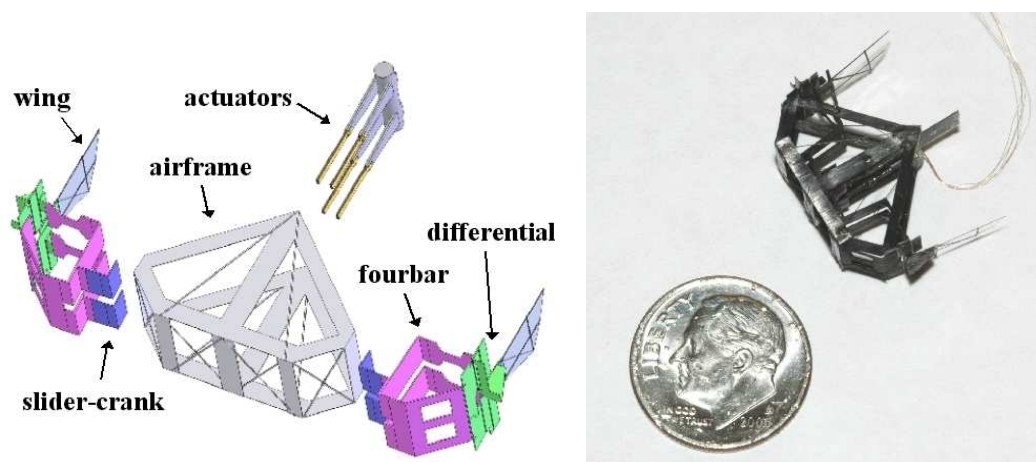


Figure 1.3: (*Left*) Exploded view of the MFI showing the relevant components of the locomotory unit. (*Right*) Recent two-wing version of the MFI. Courtesy of R.J. Wood.

The control unit, embedded in the computational circuitry of the MFI, has a hierarchical control architecture. At the top level, the trajectory planner selects appropriate flight modes (e.g., hover, forward flight, turn left, and land) to accomplish the mission of the MFI. At the middle level, the flight controller is responsible for realizing the required flight modes as well as stabilizing flight. Based on the current states (position, orientation, angular velocity, etc.) of the MFI, the flight controller determines a set of necessary wing motion and wing force to generate thrust and body torque that steer the MFI to the desired states. For example, the flight controller updates the wing kinematics so that the MFI changes from forward flight to hovering while compensating for external disturbances. At the bottom level, the wing controller is responsible for tracking the wing motion and producing the wing force specified by the flight controller. Based on the measured forces on the wings and positions of the actuators, the wing controller generates electrical signals

(input voltages) for the actuators so that the desired wing kinematics can be controlled on a stroke-by-stroke basis.

The sensory system unit contains various types of sensing devices that provide the necessary information to the control unit for navigation and flight stabilization. Due to the size constraint, conventional inertial navigation system (INS) and global positioning system (GPS) are not options for the MFI. Commercial off-the-shelf sensors such as silicon micromachined gyroscopes, accelerometers, and cameras used by MAVs are generally not suitable because of the limited computation and power available to the MFI. In addition, with a flapping frequency of 150 Hz , the MFI needs sensors and processing algorithms with bandwidth and sensitivity much higher than those needed by fixed and rotary wing MAVs. To this end, a class of biologically inspired sensors, which exhibit advantages in terms of device structure, signal processing, and power consumption over existing commercial sensors to be used on the MFI, has been designed and fabricated: an optic flow sensor for obstacle avoidance, ocelli for angular position estimation, and halteres for angular velocity estimation [111, 112]. Also, semiconductor strain gauges mounted on the wing spars and at the base of the wings are analogous to the campaniform sensilla of real insects which measure the aerodynamic forces and positions of the wings during strokes and rotations [110]. Other types of sensors, such as thermal and chemical sensors, may be carried depending on the mission of the MFI.

The communications unit of the MFI will use either a low-power RF transceiver or an optoelectronic transceiver, such as micro corner cube reflectors (CCRs) as described in [116]. The communications unit allows the MFI to exchange information with the ground station or with other communications platforms.

Currently, it is planned that the power required by the actuators, sensors, and other on-board electronics of the MFI will be supplied by a battery. However, for a robotic flyer as light-weight as the MFI, it is possible to be driven by solar cells. Since the solar power is roughly 100 mW/cm^2 on Earth surface under the full sunlight condition, solar panels consisting of cells with 10% efficiency can generate power up to 10 mW/cm^2 in outdoor environments. Therefore, solar panels can be installed on the airframe to provide necessary power for the MFI. Solar cells may also be used to charge the battery to extend the operation time and for operations under dark conditions.

1.2 The Architecture of the Virtual Insect Flight Simulator

In accordance with the major components of the MFI project, a software tool has been implemented to simulate the dynamics of a two-wing robotic flying insect and test different control strategies. This simulator, called the Virtual Insect Flight Simulator (VIFS), can help evaluate and understand the performance of the MFI design. The VIFS can be decomposed into five functional modules: the aerodynamics module, the body dynamics module, the sensory system module, the control system module, and the electromechanical system module [77]. Each of these functional modules is responsible for modeling a specific aspect of the MFI. The VIFS architecture has been modularized so that each module can be developed independently and modification of one module has minimum influence on other modules. For example, when the designs of the wings and thorax are changed, the electromechanical system module can be modified to analyze their effects on flight stability, power efficiency, and maneuverability. Moreover, the aerodynamics module can be updated to improve accuracy as better knowledge about insect flight becomes available.

In addition to the five functional modules, a three dimensional virtual environment simulation module has been implemented for the VIFS. Using the data generated by the VIFS, this graphical visualization tool animates not only the MFI body motion but also the motions of the two independent wings with three degrees of freedom (i.e., flapping, rotation, and out-of-stroke-plane motion). Moreover, the instantaneous aerodynamic forces produced by the wings during each stroke are also visualized as arrows (indicating both magnitude and direction) fixed at the center of each wing. The VIFS architecture is illustrated in Figure 1.4.

The electromechanical system module consists of models of the thorax structure, actuator dynamics, and aerodynamics of the wings. It takes as input the electrical control signals generated by the control system module and gives as output the corresponding wing kinematics. The aerodynamics module takes as input the motion of the wings and the MFI body velocities, and gives as output the corresponding aerodynamic forces and torques. This module includes a mathematical model for the non-steady state aerodynamic mechanisms. It uses a combination of an analytical model based on quasi-steady state equations and an empirically matched model based on Roboffly data. The body dynamics module takes the aerodynamic forces and torques and integrates them along with the dynamical model of the MFI body. This module computes the position and orientation of the MFI body as a function of time using equations of rigid body motion. The sensory system module takes

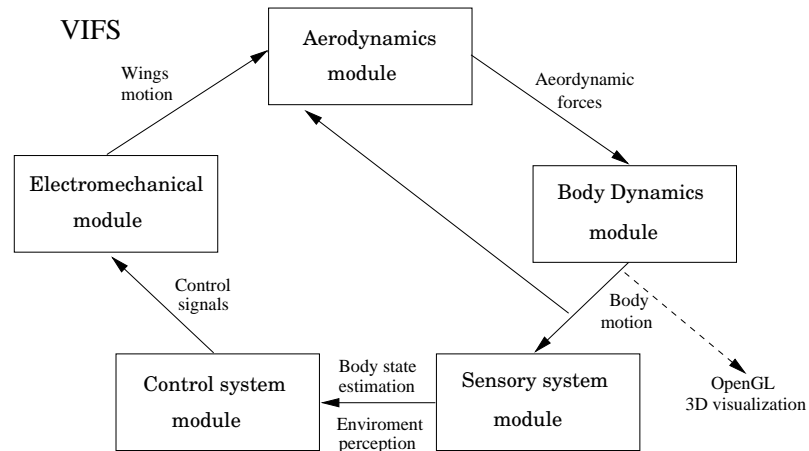


Figure 1.4: The VIFS architecture. It can be decomposed into five modules: the aerodynamics module, the body dynamics module, the sensory system module, the control system module, and the electromechanical system module.

as input the body dynamics and generates corresponding sensory information which is used to estimate the states of the MFI. This module also includes a simple description of the environment (e.g., visual background and light intensity distribution in the surrounding) so that it allows the MFI to perceive and interact with the external world. The control system module accepts signals from the sensory system module. Based on the desired mission, this module determines a flight trajectory and generates control signals for the electromechanical system module.

How real insects accomplish flight control is not fully understood at present. Experimental evidence suggests that there are at least two levels of control in real insects [15, 27]. At the low level, the halteres and ocelli directly control, respectively, the wing and neck muscles in order for the insect to maintain a stable posture during flight. This type of controllers seems to be local and reactive since they mediate corrective reflexes to compensate for external disturbances. At the high level, the brain, stimulated by visual and physiological stimuli, plans a flight trajectory based on the insect’s goal. Unlike the low level controllers, the visual system of the insect is connected directly to the haltere-steering muscles rather than to the wing muscles. It can, therefore, indirectly control flight patterns by influencing the haltere kinematics and the sensitivity of the halteres, creating “virtual” flight disturbances for which the halteres would try to compensate [15, 20]. This kind of control mechanisms seems to be an effective way to avoid potential conflicts between flight stability reflexes and voluntary maneuvers.

Inspired by the flight control scheme observed in real insects and that used in Berkeley UAV research [48], a hierarchical control architecture is proposed for the MFI control unit (see Figure 1.5). This approach can break a complex control problem into a multi-level set of smaller control schemes, each of which is responsible for a clearly defined task. Also, the controller at each level can be designed independently of those in other levels, allowing the possibility to incrementally construct a more articulated control structure. For the MFI control unit, it is reasonable to define three levels: the trajectory planner, the flight controller, and the wing controller. This control architecture is built in a top-down fashion such that the controller at each level can interact only with the controller at the level directly below it, but not vice versa. The trajectory planner is voluntary and acts like a switcher, as it simply selects one flight mode at a time. Nevertheless, the flight and wing controllers are more reactive. They continuously update the wing kinematics and track the wing trajectory in the presence of external disturbances to achieve the desired flight mode. Such a hierarchical control architecture presents a mixture of discrete events and continuous dynamics, making the MFI control unit a hybrid control system.

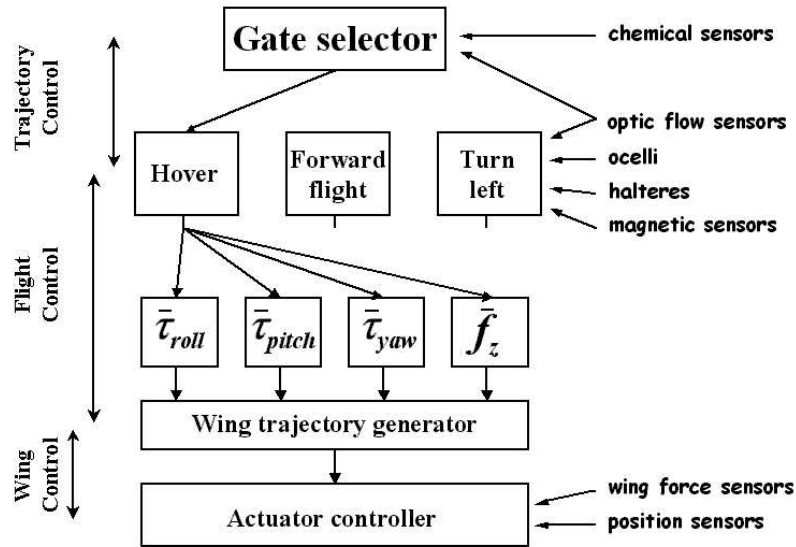


Figure 1.5: Hierarchical control and sensory modality architecture for the MFI.

Moreover, it has been suggested that insects use different subsets of their sensors for different flight modes depending on the bandwidth of the sensors and the desired motion [22, 81]. For example, during forward flight the insect may use ocelli for stabilization with

respect to the horizon while observing optic flow on its eyes for obstacle avoidance. When an object is approaching, the insect generates a saccade (a turn of 90° in less than 100 ms) during which the halteres are used to stabilize the turn because the angular velocity of a saccadic maneuver is too large for the optic flow mediated response [81]. Therefore, the proposed hierarchical control combined with sensory modality integration allows the reproduction of many insect-like behaviors, such as optomotor response, obstacle avoidance, and phototaxis, for the MFI.

1.3 Dissertation Outline and Contributions

This dissertation presents the modeling and simulations of biologically inspired sensory systems for flight control of a robotic flying insect. It also addresses the design and implementation issues of these biomimetic sensory devices. Chapter 2 describes a low-complexity visual system which detects optic flow in the insect's image plane. Chapter 3 presents an orientation referencing system from which information on the bank, pitch, and heading of the insect body can be obtained. Chapter 4 describes a biological gyroscope by which the insect's rotational velocities about the roll, pitch, and yaw axes can be measured. The purpose of this work is to provide a software test bed in which sensory motor responses of real insects can be imitated by using biomimetic sensors and simple control algorithms. Particular emphases have been placed on the following topics:

1. **Sensor Modeling** – Formal models of optic flow sensors, ocelli, and halteres are developed. Based on the proposed models, the performance of these biological sensing mechanisms can be analyzed mathematically and verified through simulation. This reverse engineering process also leads to the invention of novel biomimetic sensory devices whose performance may rival that of conventional engineering systems in many aspects.
2. **Sensor-Based Behavioral Control** – A number of insect flight behaviors is reproduced using simple insect-inspired control schemes based on the developed sensor models. These simulated responses appear to be consistent with those observed in real insects. Thus, it demonstrates the utility of these sensor models for numerous applications in robot navigation.
3. **Biomimetic Sensor Design** – Low power, light weight biomimetic sensors are designed and implemented. These devices have simple structures which allow easy

integration to a robotic platform. They also require less processing of sensor signals. Thus, these devices show benefits for use on micro robots that impose constraints on size, power, payload capacity, and computation.

4. **Sensor Integration for Flight Control** – A close-loop attitude control law based on the outputs from ocelli and halteres is proposed and successfully tested on an aerodynamic model of the MFI. This serves as a first step toward combining information from different sensory modalities to achieve flight stabilization for a robotic flying insect.

Chapter 2

Optic Flow Sensors

Vision is a vitally important sense for flying insects. With a visual system that accounts for as much as 30% of the lifted mass, some flying insects invest more in vision than any other animal. Insects, nevertheless, have very limited visual acuity due to their compound eye design. Each eye of the insect consists of many tiny lenses. Each lens and its associated light-sensitive cells form a unit called an ommatidium which records one pixel of the visual hemisphere. In order to increase the spatial acuity of compound eyes, more ommatidia are required. Depending on the species, the number of ommatidia in each eye of the insect varies from a few hundreds to tens of thousands. The largest insect eye (that of the dragonfly *Anax junius*) has interommatidial angles of about 0.25° in its most acute zone [52]. This angular resolution is approximately 30 times coarser than the 0.008° resolution (20/10 vision) in the fovea of the human retina where the visual acuity is the greatest [104] (see Figure 2.1 for a comparison). Moreover, the insect brain weighs less than a tenth of a milligram and possesses five orders of magnitude fewer neurons than does the human brain [16]. This means that any information processing and computation by the insect neural system are limited in complexity. Despite the low resolution vision and the primitive neural circuitry, insects are able to perform precise tasks such as navigating in a cluttered environment, landing on the tip of an object, and chasing mates or preys through the air. These visually guided flight capabilities of insects have fascinated scientists in both the biology and engineering communities. In the past several decades, behavioral studies of tethered or freely flying insects and neurophysiological experiments on the insect nervous system have contributed greatly toward the understanding and characterization of the movement detection mechanisms underlying an insect's visual pathway [12, 24, 49, 73,

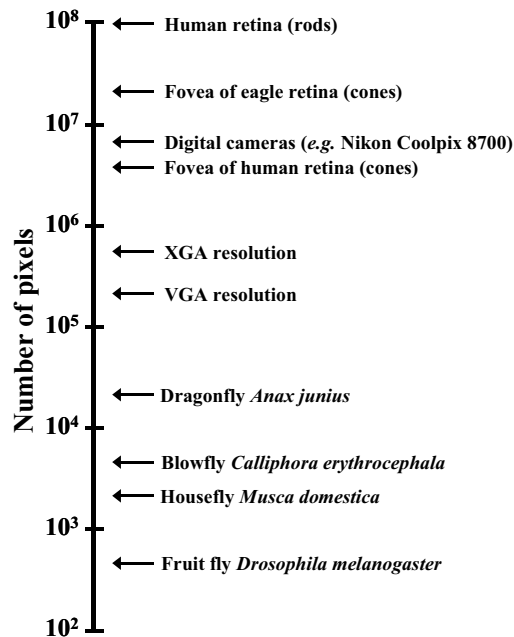


Figure 2.1: Resolution of biological eyes and man-made devices. Today’s high-end digital cameras have numbers of pixels reaching the level of the human retina. The eyes of flying insects have orders of magnitude fewer pixels. Retina data from [104]; insect data from [52].

83, 90] and artificial vision systems that are based on the motion computation algorithms in flying insects have emerged.

Conventional motion detection systems generally consist of a camera (usually a high resolution charge coupled device (CCD) imager) and a digital microprocessor. Computer vision algorithms search for features that extend both in space and time from the serially-sampled image sequence to extract motion information. Although such techniques work well under predefined conditions, they become computationally intensive and need a powerful microprocessor to run in real time for more general applications. For example, on the Sojourner rover of the Mars Pathfinder mission launched in 1996, the two CCD imagers alone consumed $0.75 W$, 5% of the total power budget at the peak solar cell output, and the Intel 8085-based CPU system consumed $3.77 W$, an additional 24% of the power budget, in processing static images [55]. Consequently, it is impractical to integrate these camera-microprocessor visual systems on micro autonomous devices because they are complex and consume too much power. Vision chips using very-large-scale-integration (VLSI) technologies, on the other hand, offer an alternative approach to the conventional motion sensing strategy. In the 1980’s, Carver Mead at the California Institute of Technology be-

gan a research effort to investigate the use of analog electronic circuits on silicon to emulate the massive parallelism in biological nervous systems (this field has become known as the neuromorphic engineering) and his group has implemented many vision, cochlea, and other neural systems using analog VLSI [57]. Neuromorphic vision sensors work by mimicking the operation of the neural circuits in biological visual systems that have been selected for by evolution for millions of years and demonstrate impressive performance in real world environments. When compared to the conventional motion detection systems, analog VLSI vision sensors provide many advantages for use on micro autonomous devices [59]:

- **Bandwidth:** In vision chip designs, high degree of interconnection among circuit elements allows signals in different components of the system to be transferred and processed in parallel.
- **Large dynamic range:** The photoreceptors of vision chips have a dynamic range over seven decades of light intensity and many vision chips have global and local adaption capabilities. Conventional cameras are at best able to perform automatic global gain control.
- **Size:** Current IC technology allows hundreds of millions of transistors to fit onto a square centimeter of silicon die. Therefore, very compact systems can be realized using VLSI implementation of vision processing algorithms.
- **Power dissipation:** Vision chips use analog circuits which operate in the subthreshold domain. There is also no energy spent for transferring information from one level of processing to another level.
- **System integration:** Vision chips may comprise most modules, such as image acquisition, signal conversion, and information processing, necessary for designing a motion detection system.

Today, a large number of vision sensors has adopted biologically-inspired models due to their VLSI friendly architectures. In particular, the simplicity and efficiency of the insect visual system have led to the development of so-called correlation-based motion detectors. Optic flow sensors based on this model or modified versions of it have been fabricated [3, 36, 53]. Sensory motor experiments showed successful use of these sensors on wheeled robotic platforms to navigate through real world environments [36, 54].

2.1 Hassenstein-Reichardt Correlation Algorithm

Studies of insect’s visually elicited flight behaviors found that flying insects are very sensitive to motion of the scene in the surrounding. When a tethered fly is presented with a leftward (or rightward) moving stimulus, it would generate a yaw torque to turn in the direction of the stimulus movement. Such a reflex, called an optomotor response, is believed to help the fly maintain a straight course by compensating for undesired deviations during flight. To account for the experimentally observed behaviors such as the optomotor response, Hassenstein and Reichardt proposed a motion detection algorithm by evaluating the spatiotemporal cross-correlation of the filtered signals (light intensity) originating from two points in the retinal image [37, 71, 72]. It turns out that this correlation-based algorithm and its variants provide an excellent description of the movement detection mechanisms not only in insects but also in vertebrates including man [2, 6, 61, 109].

The correlation algorithm accomplishes motion detection by examining what the neighboring photoreceptors perceive over time. Since the two adjacent photoreceptors are close to each other ($1^\circ - 2^\circ$ angular separation in most flying insects’ eyes [52]), they will register the same light intensity. However, if the scene is moving, the signal from one photoreceptor will lead or lag behind the signal from the other depending on the direction of the scene movement. If the signal from the left photoreceptor leads that from the right photoreceptor, then the scene is moving from left to right. On the other hand, if the signal from the left photoreceptor lags behind the signal from the right photoreceptor, the scene is moving from right to left. Therefore, one method to determine the direction of the scene movement is to first delay the signal from the left photoreceptor and compare it with the signal from the right photoreceptor, and then delay the signal from the right photoreceptor and compare it with that from the left photoreceptor. If the delayed signal from the left photoreceptor is more strongly correlated with the signal from the right photoreceptor than the delayed signal from the right photoreceptor is with the signal from the left photoreceptor, the scene is moving from left to right. Similarly, if the opposite situation is true, the scene is moving from right to left.

2.2 Reichardt Motion Sensor Model

The basic element of the Reichardt correlation motion sensor is an elementary motion detector (EMD) whose architecture is shown in Figure 2.2. In the EMD implemen-

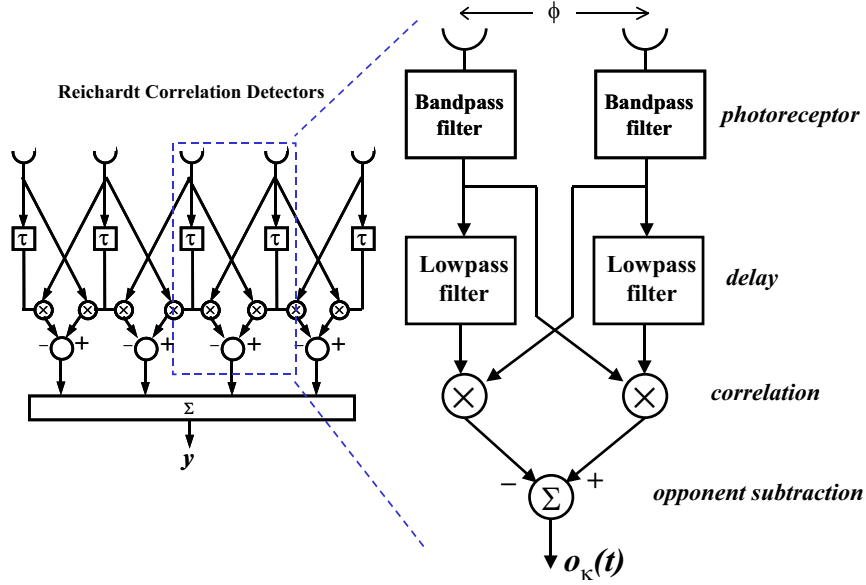


Figure 2.2: One dimensional Reichardt motion sensor and the elementary motion detector (EMD) architecture.

tation, a temporal filter is used to model the dynamics of the front end of the insect's visual system. One realization of such a temporal filter, as proposed in [36], is a bandpass filter whose frequency response is given by:

$$G_p(j\omega_t) = \frac{k_p \cdot j\omega_t\tau_H}{(j\omega_t\tau_H + 1)(j\omega_t\tau_{photo} + 1)} \quad (2.1)$$

where $\omega_t = 2\pi f_t$ is the temporal frequency of the moving stimulus, τ_H is the time constant of the DC-blocking highpass filter, τ_{photo} is the time constant defining the bandwidth of the photoreceptor, and k_p is the constant of proportionality. The low frequency zero in Equation (2.1) is used to eliminate the DC component of the illumination which contains no information about the image motion and the high frequency pole can be adjusted to prevent the photoreceptor from responding to unwanted background light sources, such as the 120 Hz signal in fluorescent lighting.

A second temporal filter is used to approximate the delay operation of the EMD. This stage is implemented using the phase lag inherent in a first order lowpass filter with time constant τ_d . The frequency response of the delay component is then given by:

$$G_d(j\omega_t) = \frac{1}{j\omega_t\tau_d + 1} \quad (2.2)$$

The correlation operation of the EMD is accomplished by multiplying the delayed signal of one photoreceptor (i.e., in one leg of the EMD) with the signal of the neighboring photoreceptor.

$$\begin{aligned} c_n(t) &= I_n(t) * g_p(t) * g_d(t) \cdot I_{n+1}(t) * g_p(t) \\ c_{n+1}(t) &= I_{n+1}(t) * g_p(t) * g_d(t) \cdot I_n(t) * g_p(t) \end{aligned} \quad (2.3)$$

where $I_n(t)$ is the light intensity perceived by the n^{th} photoreceptor in the EMD array and $g_p(t)$ and $g_d(t)$ are the impulse responses of the bandpass and lowpass filters defined in Equations (2.1) and (2.2), respectively. The strong directional selectivity of the EMD can be achieved by subtracting the correlated signals in the two adjacent legs in opponency to get the detector output:

$$o_\kappa(t) = c_{n+1}(t) - c_n(t) \quad (2.4)$$

Furthermore, the outputs of individual EMDs in the array are summed to obtain the overall sensor response:

$$y^f(t) = \sum_{\kappa} o_\kappa(t) \quad (2.5)$$

where κ is the number of EMDs in the array. This spatial summation of the outputs of many local detectors has the effect of integrating over different phases of the stimulus perceived by the sensor and hence significantly eliminating the pattern dependent oscillations observed in the output of a single EMD under the steady-state condition (see the middle plot of Figure 2.3). Alternatively, these pattern dependent oscillations can be removed by averaging the output over time, but temporal integration would decrease the response time of the sensor. Insects also perform spatial integration of the responses of their motion sensitive cells to reduce the pattern dependent oscillations [73, 83].

2.3 Characteristics of Reichardt Motion Sensors

In the following simulations, the model parameters presented in the previous section are chosen as follows: $\tau_H = 200 \text{ ms}$, $\tau_{photo} = 5 \text{ ms}$, $\tau_d = 40 \text{ ms}$, $k_p = 0.3$, and $\kappa = 19$ unless otherwise stated.

2.3.1 Response to Simple Image Motion

The sensor model is tested using a stimulus of sinusoidal grating moving along the sensor axis. Figure 2.3 shows the sensor response to a laterally drifting grating. It can be

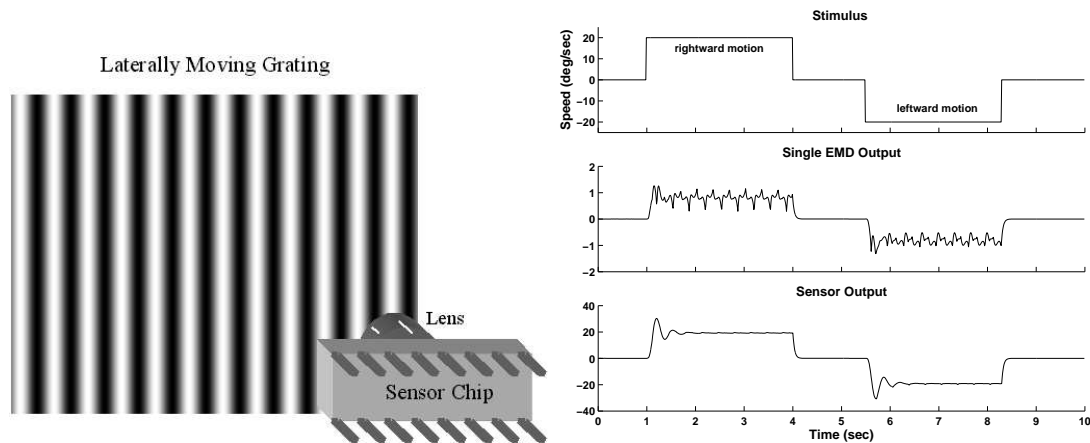


Figure 2.3: Directional selectivity of the sensor. A stimulus of sinusoidal grating moves along the sensor axis in alternating directions (*left*). The rightward motion of the stimulus produces a positive output, while the leftward motion of the stimulus produces a negative output (*right*). Pattern dependent oscillations are observed in the output of a single EMD. Also note the differences between the transient responses and the decay rates at the onset and offset of the stimulus motion.

seen that the sensor is highly directionally selective. Similar to the membrane potential of the motion sensitive neurons in insects [35], the sign of the sensor output indicates the direction of the stimulus movement. In addition, the sensor responds strongly to off-axis image motion. The sensor exhibits a *cosine* curve tuned to the stimulus moving directions ϑ relative to the sensor axis, as shown in Figure 2.4. A detector array whose axis is perpendicular to the original sensor would return a *sine* curve tuned to the same stimulus motion. Thus, a minimum of two detector arrays arranged in an orthogonal configuration are necessary to determine the direction of the stimulus movement in two dimension.

Moreover, a large transient response occurs at the onset of stimulus motion. The modulation frequency of these oscillations is equal to the temporal frequency of the stimulus. This transient response at the onset of stimulus motion is also observed in the insect's motion sensitive neurons and has been shown to be a consequence of summing the outputs of many EMDs which see different phases of a periodic stimulus [23]. This transient decays to a steady-state level at a rate given by the time constant of the EMD's lowpass filter. The response at the offset of stimulus motion, however, exhibits no oscillations and it decays to the steady-state much faster than the onset decay. The offset response in the insect's interneurons is also quick and independent of the stimulus temporal frequency.

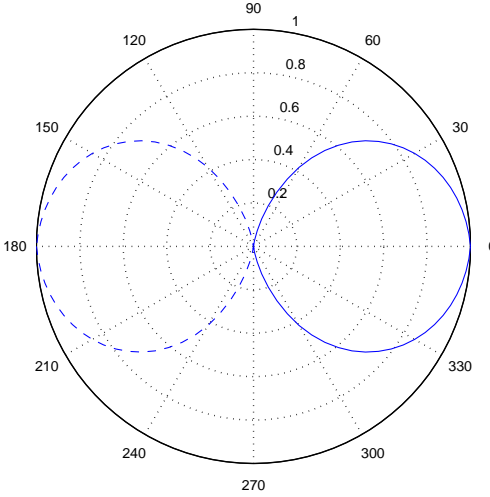


Figure 2.4: Directional tuning of the sensor. A sinusoidal grating moves at different angles ϑ relative to the sensor axis. Normalized sensor response is shown and the dashed section indicates negative sensor output.

2.3.2 Robustness to Noisy Stimuli

In order to investigate the influence of noise on the sensor performance, noise with random phase is introduced (either spatially or temporally) to a sinusoidal grating. The noisy stimuli are presented to the sensor at different levels of signal-to-noise ratio (SNR) in dB :

$$\text{SNR} = 20 \log_{10} \frac{I_{stimulus}}{I_{noise}} \quad (2.6)$$

where $I_{stimulus}$ and I_{noise} are the intensities of the stimulus and noise, respectively.

In the left panel of Figure 2.5, snapshots of noisy grating at SNR of 10 dB , 0 dB , and -10 dB are given. It can be seen that at $\text{SNR} = -10\text{ dB}$, features that can be reliably tracked from one frame to the next to reveal the direction of the stimulus movement become very faint. The right panel of Figure 2.5 shows the sensor outputs, which are not useful for providing precise visual cues of the environment at low SNR levels. However, the sensor is still able to accurately discriminate between the leftward and rightward motions of the stimulus (the signs of the sensor output) even at $\text{SNR} = -10\text{ dB}$. The directional selectivity of the sensor as a function of the SNR level is given in Figure 2.6. This result suggests that the sensor would still be useful for applications, such as the optomotor control, under noisy conditions. The robustness, in terms of directional selectivity, of this correlation-based motion detection algorithm against noisy inputs is a consequence of the opponent

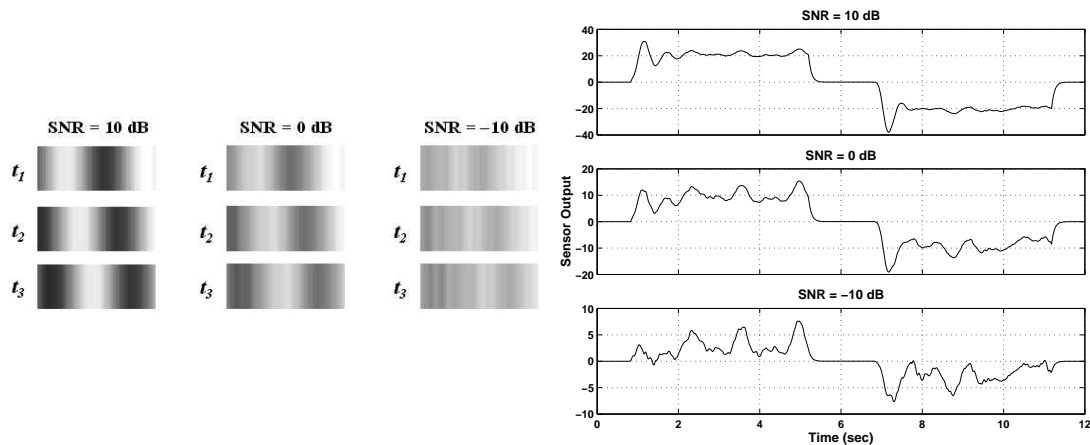


Figure 2.5: Snapshots of noisy sinusoidal grating at various levels of SNR (*left*). Sensor responses to the noisy stimuli (*right*).

subtraction that eliminates most of the common-mode signals [36].

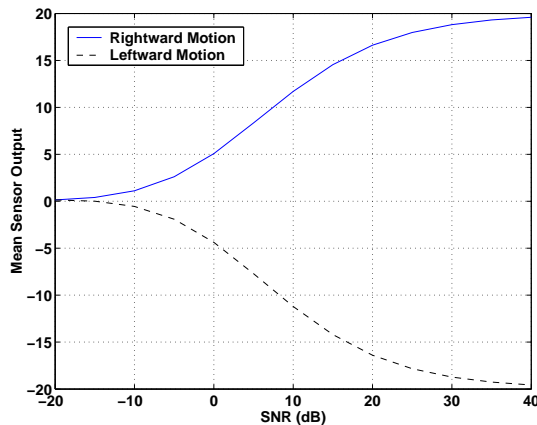


Figure 2.6: Robust directional discrimination of the sensor under noisy conditions. The curves represent the means of the chattering sensor outputs at various levels of SNR.

2.3.3 Spatiotemporal Frequency Tuning

While the Reichardt correlation sensor exhibits the property of strong directional selectivity, it does not provide an unambiguous indication of the speed of a stimulus. It confounds the speed of a stimulus with its spatial structure. A coarse, rapidly moving grating would produce the same response as that produced by a fine, slowly moving grating. To see this, sinusoidal gratings with spatial frequencies of 0.06, 0.085, and 0.12 cycles per

degree (cpd) are presented to the sensor and the normalized responses as a function of the stimulus speed are plotted in the left panel of Figure 2.7. The 0.06 cpd grating moving at $70^\circ/s$ elicits the same maximum response as that of the 0.12 cpd grating moving at $35^\circ/s$. Since the temporal frequency of a stimulus is equal to the product of the speed and spatial frequency of that stimulus, it can be deduced that the Reichardt correlation sensor is tuned to the temporal frequency of a stimulus. This is indeed the case as all three response curves peak at the same temporal frequency of the stimuli (see the right panel of Figure 2.7). A plot of the sensor response as a function of the spatial and temporal frequencies of a stimulus is given in Figure 2.8. The exact shape of this spatiotemporal frequency response and the location of the peak depend on the angular separation of the neighboring photoreceptors, the size and shape of the receptive field of the photoreceptors, and the characteristics of the temporal filters in the EMDs [90]. Biologists found that depending on the lifestyle adopted by the insect, the visual systems of different insect species possess different optima of the spatiotemporal frequency tuning [65]. For example, some hoverflies or hawkmoths need to detect very low pattern speeds while they are hovering in front of flowers and sucking nectar. They have motion detectors tuned to very low image speeds. Other insects which feed from the same flowers rarely hover and indeed some bumblebees “crash land” on a flower before feeding. Such insects have motion detectors tuned to very high image speeds.

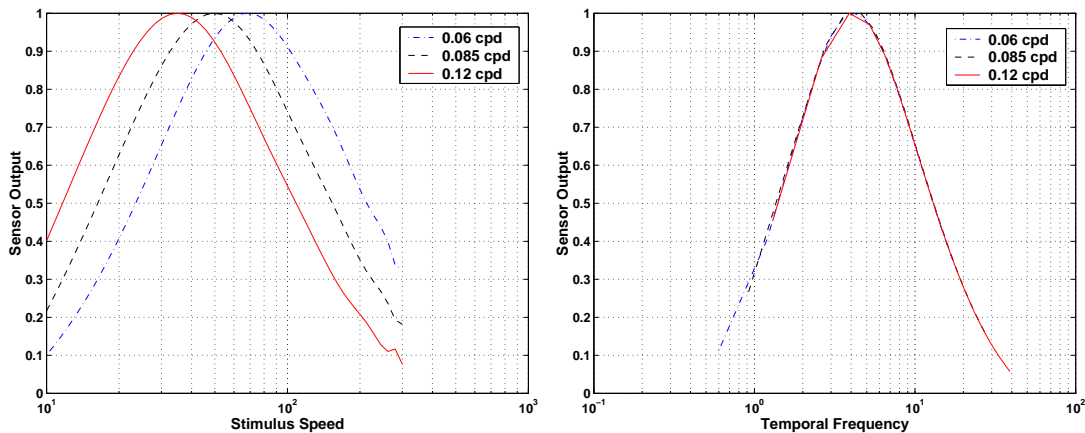


Figure 2.7: Sinusoidal gratings with three different spatial frequencies are presented to the Reichardt correlation sensor. Normalized responses of the sensor as a function of the stimulus speed (*left*) and as a function of the temporal frequency of the stimuli (*right*) are shown. It can be seen that the Reichardt correlation sensor is tuned to the temporal frequency of the stimulus.

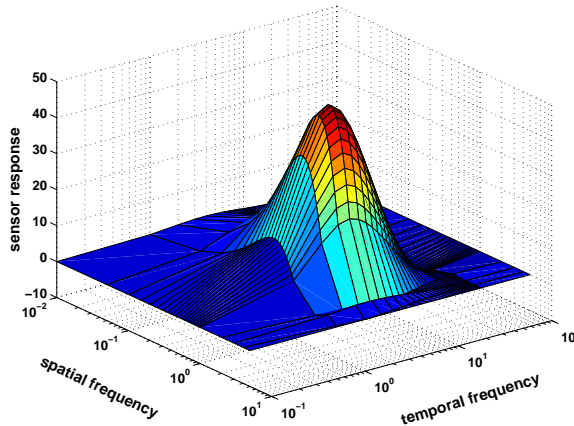


Figure 2.8: Spatiotemporal frequency response of the Reichardt correlation sensor. The location of the peak in the spatiotemporal frequency space depends on the parameters of the EMDs.

2.3.4 Image Speed Tuning

The problem of image speed ambiguity seen in the previous section can be resolved by using more than one correlation detector in the system, with each correlation detector having a different spatiotemporal frequency optimum [38]. Figure 2.9 illustrates the contour plot for the spatiotemporal frequency responses of a system comprising three detectors. A low image speed (a small temporal-to-spatial frequency ratio) preferentially stimulates Detector 1 while a high image speed (a large temporal-to-spatial frequency ratio) preferentially stimulates Detector 3. Consequently, the relative image speed can be estimated independently of the image spatial structure by determining which detector produces the greatest response. Nonetheless, such a multi-detector scheme for image speed tuning requires more hardware to be implemented in one sensor because each detector uses a different set of design parameters.

Alternatively, a simplified version of the Reichardt correlation detector, called a half-detector, has been proposed that can effectively reduce the spatial frequency dependence and hence achieve image speed tuning [114]. In the half-detector architecture, photoreceptor signal in one leg of the detector is correlated with the delayed signal in the adjacent leg, but the subsequent opponent subtraction is omitted (see Figure 2.10). This half-detector architecture is advantageous in terms of sensor implementation since it is almost identical to the architecture of a standard detector. The desired signals can be ob-

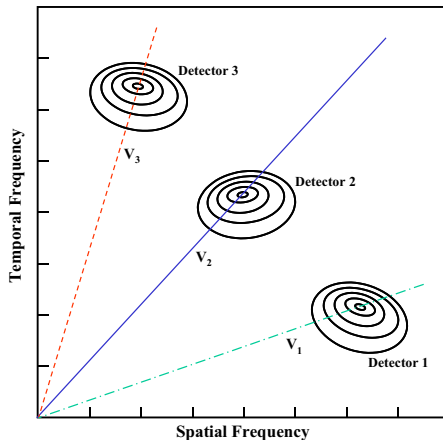


Figure 2.9: Contour plot for three correlation detectors, each producing a maximum response at a different spatiotemporal frequency. Detector 3 responds strongly to a high image speed V_3 , Detector 2 responds strongly to an intermediate image speed V_2 , and Detector 1 responds strongly to a low image speed V_1 .

tained directly from the existing components and hence no additional hardware is needed. However, due to the asymmetrical structure of a half-detector, the preferred direction of image motion would elicit a stronger output than that produced by the null (non-preferred) direction. If two half-detectors in an anti-symmetrical arrangement are used, the biased response of the half-detector to the direction of image motion can be avoided. In the following sections, such an anti-symmetrical half-detector configuration will also be referred to as a half-detector for simplicity.

To examine the image speed tuning of a half-detector, sinusoidal gratings with spatial frequencies of 0.06, 0.085, and 0.12 cpd are presented to the sensor. The normalized responses of the half-detector as a function of the grating speed are given in the left panel of Figure 2.11. Since the response curves peak at approximately the same grating speed, it is evidenced that the half detector is more sensitive to the image speed and its response is less dependent on the image spatial structure. However, as explained in Section 2.2, the primary reason for implementing the opponent subtraction in the standard Reichardt correlation detector is to achieve strong directional selectivity. Therefore, the price paid for the omission of opponent subtraction to improve image speed tuning is the loss of directional sensitivity in a half detector. This result can be seen in the right panel of Figure 2.11 (compare to Figure 2.4).

Flying insects seem to utilize both a highly directionally selective, temporal-

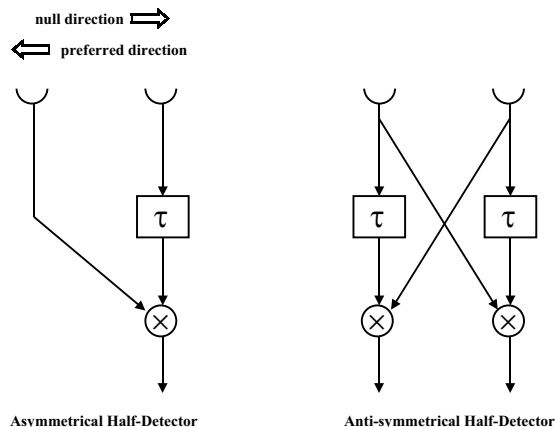


Figure 2.10: Half-detector architecture (*left*). The half-detector produces a strong output for the preferred motion direction and a weak output for the null motion direction. Two half-detectors in an anti-symmetrical configuration can avoid the biased response to the direction of the stimulus movement (*right*).

frequency tuned system for stabilizing flight and a directionally insensitive, speed-tuned system for navigation [94]. Although motion sensitive neurons with maximum sensitivities at different spatiotemporal frequencies and partially symmetrical motion detectors (i.e., only a fraction of the delayed signal in one leg of the EMD is subtracted from the delayed signal in the adjacent leg) both have been reported in the visual systems of flying insects [24, 42], it remains unclear whether the non-directional, speed-tuned system in flying insects uses a correlation type of motion detection schemes like those described in this section.

2.4 Simulations of Insect Flight Behaviors Using Reichardt Motion Sensors

Despite the fact that the principles of insect vision have been applied to robot navigation for more than a decade, most of the applications have used camera-microprocessor visual systems with off-board image processing and control. Recently, a few groups have attempted to integrate insect-inspired optic flow sensors on autonomous robots. Harrison [36] implemented an optomotor system by mounting a wide-field motion sensor on a two-wheeled robotic platform that had been configured to move in a curved trajectory. The forward-facing sensor could detect optic flow induced by the rotatory motion of the robot and trigger a compensatory torque response such that the robot would travel in straight

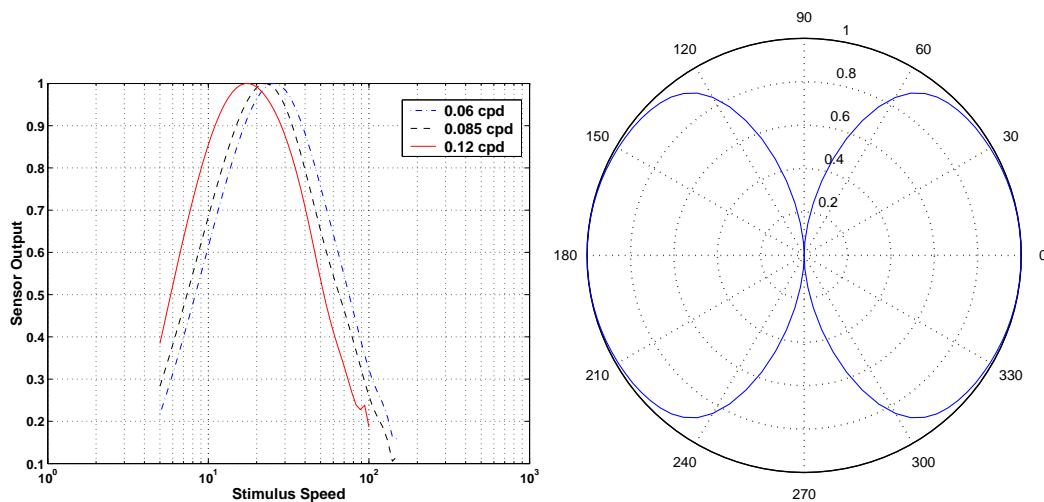


Figure 2.11: Sinusoidal gratings with three different spatial frequencies are presented to the half-detector. The responses are tuned to the stimulus speed (*left*). However, the sensitivity of the half-detector to the stimulus moving directions ϑ is greatly reduced (*right*). Different from the output of the standard Reichardt detector, the output of the half-detector is always positive regardless of the direction of the stimulus movement.

paths. Liu and Usseglio-Viretta [54] demonstrated a fixation-like behavior by using two large-field motion sensors on a wheeled robot. A black stripe was oscillated on a white background on one side of the robot. In this case, one of the two sensors would measure a greater motion energy and the robot turned accordingly toward the direction of this sensor. Centeye carried out experiments about collision avoidance and altitude control in a park with small radio-controlled aircraft equipped with mixed-mode VLSI optic flow detectors [7]. Building upon the preliminary work by Centeye, Oh *et al.* were able to demonstrate autonomous landing [34] and collision avoidance [66] with light-weight aircraft in indoor environments. Zufferey and Floreano further demonstrated continuous autonomous steering in an enclosed environment with their 30 g airplane equipped with two lateral one dimensional optic flow detectors and an angular rate sensor [117].

In the following sections, additional insect flight behaviors that have been observed in the experiments are reproduced using the Reichardt correlation motion detection model presented in Section 2.2. In the simulations, both the standard-detector and half-detector models are included because the insect visual system possesses the properties of both models. The purpose of these simulations is to further demonstrate the potential utilities of vision sensors in robot navigation.

2.4.1 Centering Response

When an insect flies through a narrow channel, it tends to fly through the center. However, insects can not estimate the range of an object precisely through binocular stereopsis because they have immobile eyes with fixed focus optics and their eyes are positioned very close together [86]. Biologists believed that insects rely on using image motion as a significant cue for estimating the distance to an object. Therefore, when flying through a tunnel, the insect simply balances the retinal image motion on its eyes to maintain equidistance from the walls. Computationally, this strategy is more amenable and efficient to real time implementation than methods that use stereo vision to calculate the distances to the walls. To simulate this centering behavior, two sensors, one on the left hand side of the insect and the other on the right, are used to represent the insect's eyes. For the hardware design consideration, the field of view of these sensors is limited to 90° although each eye of real insects can see almost the entire visual hemisphere.

The insect is assumed to fly through a tunnel whose side walls are painted with a pattern consisting of a black and white grating. As shown in Figure 2.12, the insect initially follows the middle path of the tunnel. The outputs of the left and right sensors balance and hence the insect would maintain a stable flight. However, when the insect's trajectory is perturbed toward one side of the tunnel during its flight, there would be unbalanced image motion on its two sensors. A higher image motion on one sensor indicates that the grating on that side is closer, while a lower image motion indicates that the grating is farther away. As a consequence, the insect would have to return to the middle line of the tunnel in order to restore the balance between the outputs from its two sensors. In addition, this centering response is not affected by the textural content of the walls. The insect always tries to maintain equidistance from the two walls, even when the spatial frequencies of the gratings on the two sides are different (see the right panel of Figure 2.12).

Since the insect exhibits the centering behavior irrespective of the patterns on the walls, it is necessary for the insect to use a mechanism that measures the speed of the image independently of the spatial structure. This can be demonstrated in Figure 2.13, where the two walls of the tunnel carry gratings with the same spatial frequency. When the grating on one of the walls moves in the direction of the insect's flight, the sensor on that side would perceive a lowered image speed relative to the image speed seen by the sensor on the other side. As a result, the insect would fly closer to the wall with the moving grating in order to maintain the balance between the sensor outputs. On the other hand, when the grating

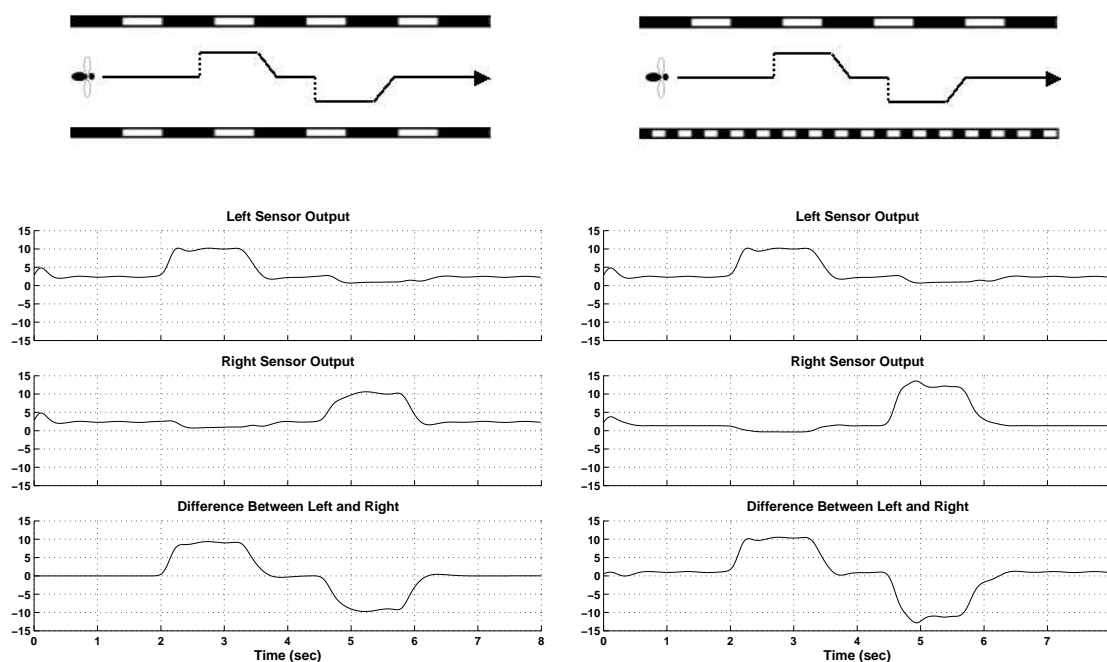


Figure 2.12: The insect flies through a tunnel whose walls carry black and white gratings. When the trajectory of the insect shifts toward either side, one of the insect's eyes would see a higher image motion than that seen by the other eye. Thus, the insect would return to the midline in order to balance the image motion on its two eyes (*left*). Even when the spatial frequencies of the gratings on the two walls differ by a factor of three, the insect still exhibits this centering behavior (*right*).

moves in the opposite direction of the insect's flight, thereby increasing the image speed on that side relative to the other, the insect's trajectory would shift away from the wall with the moving grating. It has been observed that flying insects have a tendency to keep away from rapidly moving objects during their flight [91]. From this point of view, the centering response may simply be a consequence of the reflex in which the insect is trying to avoid moving objects from all sides when flying through a narrow opening.

2.4.2 Regulation of Flight Speed and Visual Odometry

Experiments on fruit flies and honeybees have shown that insects control the speed of their flight by a visual motion detection mechanism [19, 95]. When flying upstream in a wind-tunnel whose walls were decorated with a black-and-white striped pattern, fruit flies regulated their flight speed by holding the apparent image speed on their eyes constant.

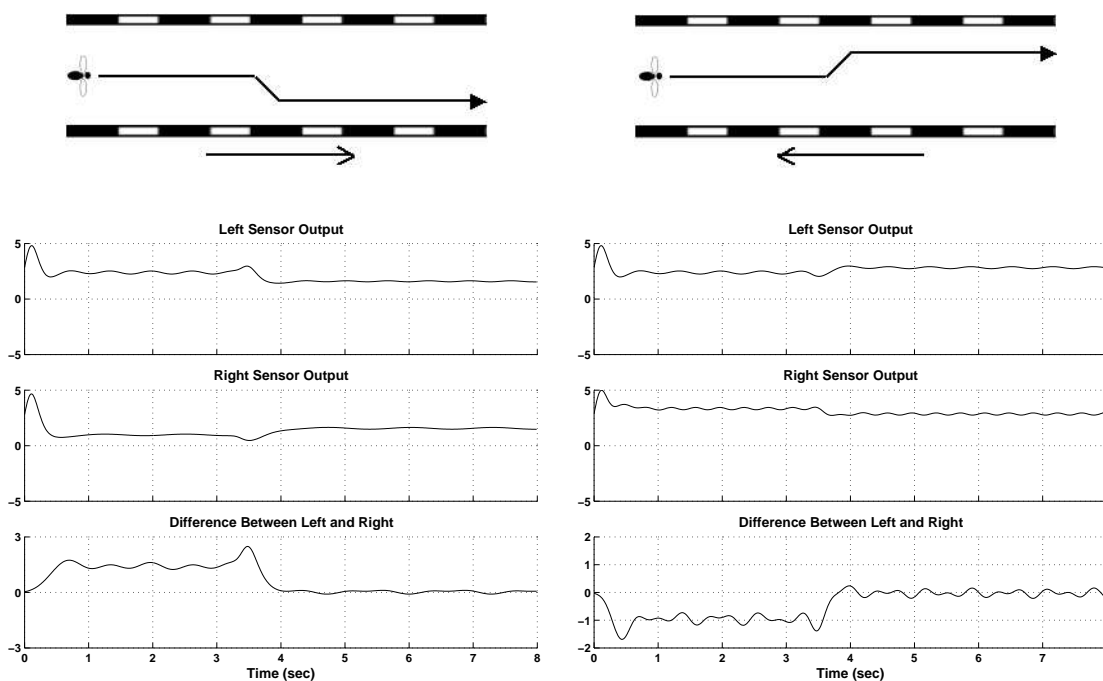


Figure 2.13: The insect flies through a tunnel whose walls carry gratings that can be made to move in either direction. When the grating on one wall moves in the direction of the insect's flight, the insect's trajectory would shift toward that side (*left*). However, when the grating moves in the direction opposite to that of the insect's flight, the insect's trajectory would shift away from that side (*right*). In effect, the insect maintains the balance between the outputs of the two sensors.

In addition, the flies also compensated for the changing headwind in the tunnel, increasing or decreasing their thrust so as to maintain the same ground speed. However, when the pattern on the walls was made to move forward or backward while the headwind remained unchanged, the flies would also adjust their thrust accordingly (and hence affecting their absolute position in the tunnel) such that the speed of the image on their eyes was always clamped at a fixed value. Experiments in which the period of the stripes was varied did not affect the flight speed of the flies. Therefore, the speed-regulating system in flying insects is similar to the centering system in this respect.

In order to simulate this visual control of flight speed, the insect is assumed to fly through a tapered tunnel whose walls carry patterns of black-and-white gratings. As seen in the previous section, the closer the insect is to the wall, the higher the perceived image speed. As a result, the insect needs to decrease its flight speed as it flies toward the

narrowed portion of the tunnel so as to keep the speed of the image on the eyes constant. Conversely, the insect increases its flight speed as the tunnel widens. On the other hand, the insect flying through a tunnel of uniform width does not change its speed even when the spatial frequency of the gratings on the walls is abruptly changed. These behaviors are demonstrated in Figure 2.14.

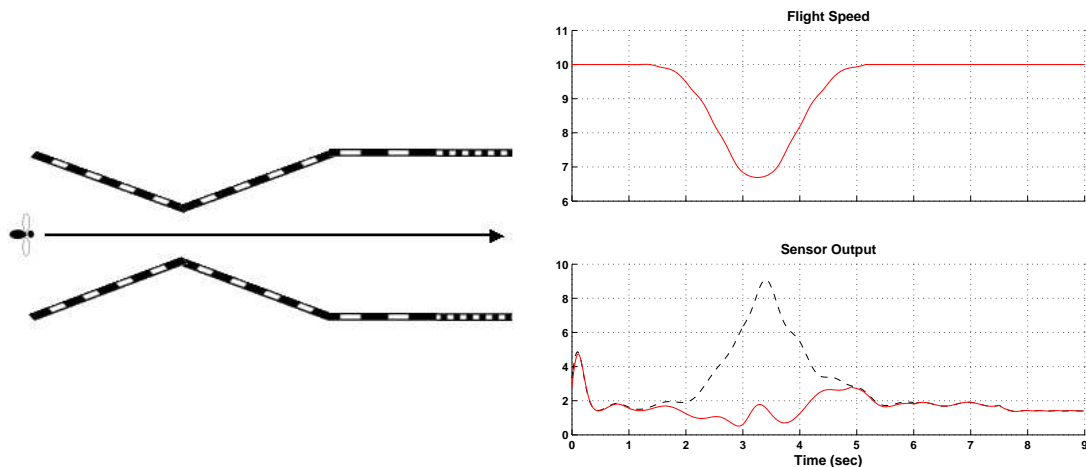


Figure 2.14: The insect regulates its flight speed in a tapered tunnel by holding constant the image speed of the environment. As the tunnel narrows, the insect decreases its speed so as to maintain the same image speed on its eyes. In the section of uniform width, however, the insect flies at a constant speed irrespective of the spatial content of the gratings on the walls. The dashed line at the bottom plot indicates the sensor output if the insect were to fly at a constant speed through the tunnel.

It is known that honeybees have the ability to learn and estimate short distances travelled because they can navigate accurately and repeatedly to a food source. However, the methods by which honeybees gauge the distance flown to a goal remained enigmatic. By investigating a variety of cues such as flight duration, energy consumption, image motion, inertial navigation, and landmarks, it has been shown that the bees measure the distance flown in terms of the integral over time the motion of the image that is experienced on the way to the goal (i.e., visual odometry) [92, 95]. Therefore, the distance travelled by the bees can be determined by:

$$\text{Distance}_1 = \int (V_L + V_R) dt \quad (2.7)$$

where V_L and V_R are the image speeds seen by the left and right eyes, respectively. Although this method provides a good estimate of distance travelled by real insects due to their

centering response, it is not robust to be used in robot navigation, especially if the robot is meant to move close to one side of a tunnel at some point during its journey. This is because the integrand of Equation (2.7) is proportional to the sum of the reciprocals of the distances to the two walls. When the robot's trajectory is close to one of the walls, the integrand becomes very large at these points, resulting in a less consistent calculation. A better distance measure, as suggested in [88], would be:

$$\text{Distance}_2 = \int \frac{4}{(1/V_L + 1/V_R)} dt \quad (2.8)$$

This approach tends to be independent of the robot's position along the width of the tunnel because the denominator of the integrand is proportional to the sum of the distances to the two walls, which is a fairly constant value irrespective of the robot's lateral position. The results of calculating distance travelled using both distance measures are seen in Figure 2.15. In the simulations, the insect is meant to stop after a fixed amount of signal has been accumulated. When moving in a straight trajectory in the tunnel, both Distance_1 and Distance_2 give a good estimate of the distance travelled. However, Equation (2.8) shows a better performance than that of Equation (2.7) when the insect is made to move in a meandering trajectory.

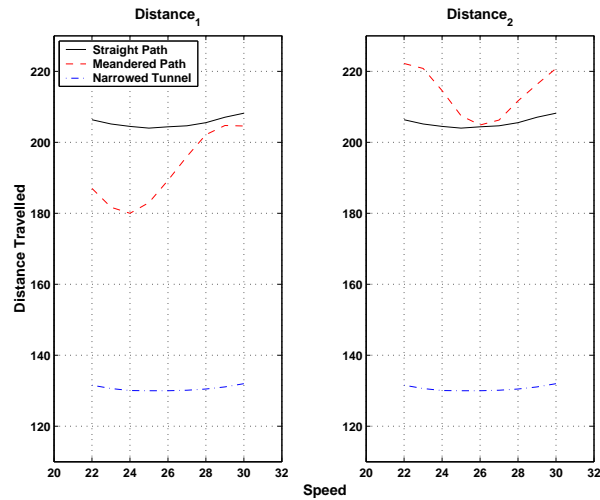


Figure 2.15: Visual odometry of flying insects. The distance flown by an insect is gauged by the integral over time the motion of the image that is experienced during its journey. The insect, flying at different speeds, travels roughly the same distance when its flight path is straight. However, Distance_1 becomes inconsistent when the flight path is meandered. Moreover, the actual travel distance becomes shorter when the insect flies in a narrower tunnel even though the calculated travel distance remains the same.

It should be pointed out that both Equations (2.7) and (2.8) do not yield the travel distance in an absolute sense because the perceived image motion depends on the environment through which the robot navigates and on the lateral distances of objects to the robot. A higher image motion seen by the robot (e.g., when moving through a narrower tunnel) will cause the signal to accumulate to the stopping point faster and therefore resulting in a shorter actual travel distance (see the dash-dotted lines in Figure 2.15). These equations, nonetheless, provide indicative measures that a fixed distance has been travelled, provided the robot traverses in the same environment.

2.4.3 Obstacle Avoidance

Flying insects have to quickly and reliably detect approaching objects during their flight in order to avoid head-on collisions as well as lateral impacts. Because the two eyes of an insect see different visual fields, they register different optic flows from the scenes. If the insect's left eye sees a greater optic flow than that seen by its right eye, it means that the insect is flying closer to an object on its left side. On the other hand, if its right eye sees a greater optic flow, the insect is closer to an object on its right side. This type of left versus right comparison is similar to the scheme seen in the centering response. However, flying insects use the time-accumulated optic flow signals, instead of the instantaneous optic flow signals as those used in the centering response, on their individual eyes to determine which side is approaching an object. The dynamics of the optic flow accumulation on either eye of the insect can be approximated by a differential equation of the form:

$$\frac{dY^f}{dt} = y^f - k_l \cdot Y^f, \quad Y^f = 0 \text{ at } t = 0 \quad (2.9)$$

where Y^f is the accumulated signal, y^f is the output from the eye, and k_l is the leak rate. For physiological reasons, such integration needs to be leaky in order to prevent long-term accumulation of weak signals that trigger reactions [11]. Furthermore, when the response of motion sensitive cells reach a steady-state level, the output from such physiological integrators is given by a solution of Equation (2.9):

$$Y^f = \frac{y^f}{k_l} (1 - \exp(-k_l t)) \quad (2.10)$$

Temporal integration of the optic flow signal has the benefit of conditioning the signal, making the input to the subsequent threshold detector less sensitive to high frequency noise. More importantly, it yields a signal that increases very rapidly due to the quick

expansion of images across the insect's eyes as it flies close to an object, resulting in a more precise and reliable indication of an immediate collision.

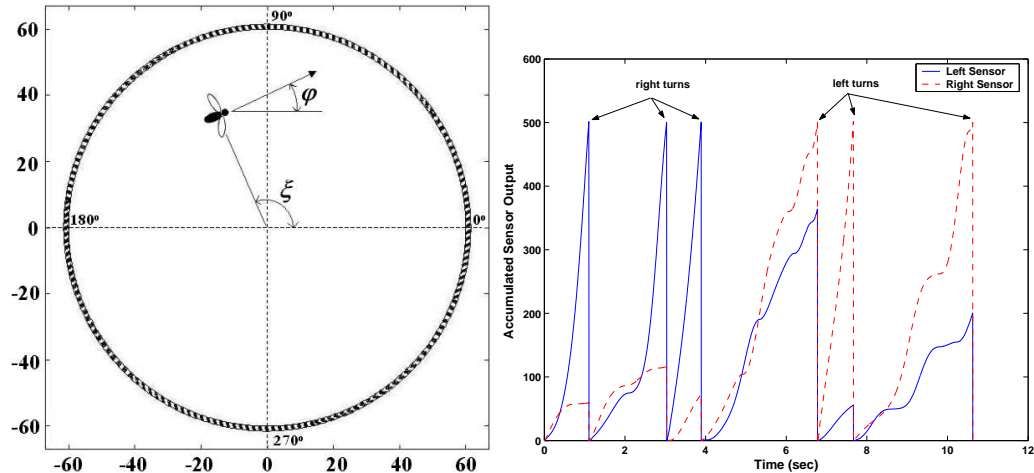


Figure 2.16: The insect flies inside a flight arena whose wall carries a pattern of sinusoidal grating (*left*). The eyes of the insect see different scenes and hence register different optic flows. The optic flow signals on the left and right eyes are integrated over time (*right*). When the accumulated signal on one eye exceeds a specified threshold, the insect generates a saccade in the opposite direction in order to prevent a collision into the wall on that side.

In order to reproduce the collision avoidance behavior in flying insects, a circular flight arena is simulated (see the left panel of Figure 2.16). The inner wall of the arena is decorated with a pattern of sinusoidal grating. An insect flies in segments of straight flight inside the arena and it generates a sharp steering maneuver, called a saccade (a turn of approximately 90° in less than 100 ms), only when it senses an imminent collision into the arena wall, as observed from the free flight patterns in fruit flies [99]. When the insect is initially far from the rim of the arena, its eyes do not see significant changes in the optic flows. However, as the insect flies toward the wall, the magnitudes of the optic flow on its eyes rise quickly. If the insect comes really close to the wall on one side, the time-accumulated optic flow signal on that side will soar. Therefore, when a threshold value is specified for the two eyes, the insect would make a right turn if the accumulated signal on its left eye reaches the threshold first. Conversely, it would make a left turn if the accumulated signal on its right eye reaches the threshold first. The right panel of Figure 2.16 shows the accumulated optic flows on the left and right eyes as the insect makes several saccades inside the arena. Following a saccade, the signals on both eyes will be cleared, and the insect will continue to fly along a straight trajectory until the accumulated signal on either

side increases again to a level at which another saccade is triggered [99].

Furthermore, experiments using freely flying fruit flies discovered that when the fly was placed in an arena whose wall carried a textured pattern, it would initiate saccades more frequently and hence its flight trajectory was confined in the central region of the arena. However, when the fly was placed in an arena whose wall carried a uniform pattern, it would initiate saccades less frequently and hence it would wander around a larger region of the arena [99]. This behavior is due to the fact that the textured pattern on the wall could induce a greater optic flow than that induced by the uniform pattern across the eyes of the fly as it navigated in the arena. As a result, the time-accumulated signal on the eyes would exceed the threshold more quickly in the textured arena than in the uniform arena. The same kind of landscape-dependent steering behavior in flying insects is reproduced in the simulation.

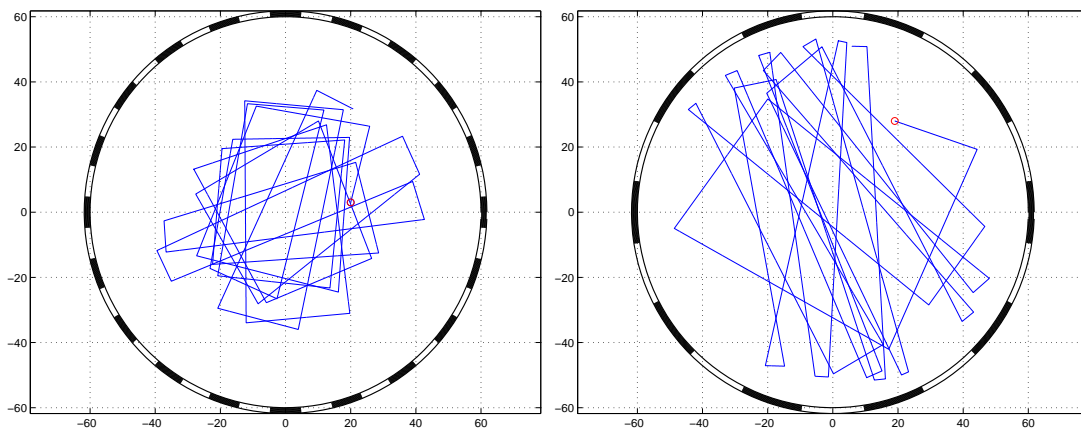


Figure 2.17: The insect initiates saccades at different frequencies dependent on the spatial content on the arena wall. The insect makes turns more quickly when the grating on the wall has a higher spatial frequency (*left*). The insect makes turns less frequently when the grating on the wall has a lower spatial frequency (*right*). The circle indicates the initial location of the insect.

As shown in Figure 2.17, the insect generates saccades less frequently in an arena whose wall carries a grating of low spatial frequency than in an arena whose wall carries a grating of high spatial frequency. In addition to the environmental stimuli, this steering behavior can also be tuned by adjusting the threshold value for the accumulated optic flow signal on the sensors. When the threshold is set to a small value, the time-accumulated output of the sensors will reach this level quickly and hence the insect has to make turns even when it is still far from the wall. As the threshold value increases, it will take longer

time for the accumulated output of the sensors to reach the threshold. Therefore, the insect can fly closer to the rim and explore a larger region of the arena (see Figure 2.18). These experimental results suggest that different collision avoidance behaviors in robot navigation may be achieved by adjusting a single parameter (the threshold value) of the visual sensors in the control system. It is not known, however, whether real insects use a similar strategy (i.e., adaptively varying the threshold value of their eyes) to prevent collisions when exploring or searching for objects in a complex environment.

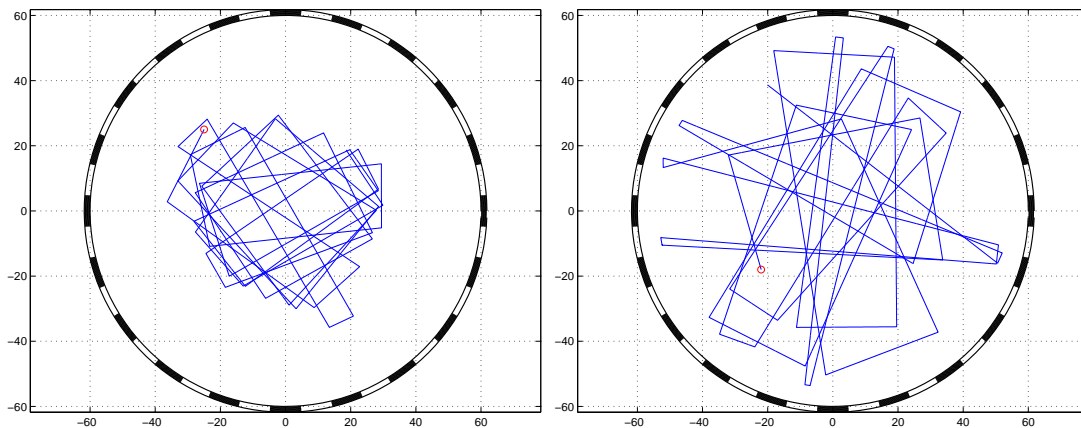


Figure 2.18: The insect initiates saccades at different frequencies dependent on the specified threshold for the time-integrated optic flow signals. The insect responds quickly to the rising optic flow signal and generates turns more frequently if the threshold for the accumulated sensor output is set to a smaller value (*left*). If the threshold is increased to a larger value, the insect has a slower response and hence generates turns less frequently (*right*).

2.4.4 Landing Response and Terrain Following

In addition to the obstacle avoidance reaction, a pattern of image expansion in an insect's visual field plays the major role in mediating other types of flight maneuvers, such as landing responses and terrain following. Experiments using tethered fruit flies found that when confronted with an expanding object, the flies either turned away from it or prepared to land [98]. If image expansion was in the lateral portion of the fly's field of view, the fly exhibited a saccadic maneuver. In contrast, image expansion in the frontal portion of the fly's view primarily triggered leg extension and a decrease in forward thrust, indicative of a landing response. Moreover, because the collision avoidance and landing responses are all-or-nothing events, both are likely to be elicited when some neural signal reaches a threshold.

Therefore, temporal integration of the optic flow signals, as in Equations (2.9) and (2.10), may also account for the mechanism underlying the landing response. The differences between the latencies of these two systems, however, may be explained by different threshold levels and/or leak rates in the temporal integration processes [98].

In the simulation of the landing response, an insect is assumed to fly over a terrain of hills and valley. A forward-facing visual sensor is placed at the front end of the insect. The sensor is tilted downward by 60° and its sensing direction is parallel to the longitudinal axis of the insect body. When the insect approaches a hill, the optic flow induced by the pattern on the ground accumulates rapidly. If the insect decides to land when this signal reaches a certain threshold level, it will decelerate quickly in order to prevent crash landing. Srinivasan observed that honeybees land by keeping the optic flow on the landing surface constant (v/d is constant where v is the speed of the insect and d is the distance to the landing site) [93]. In the simulation, the deceleration of the insect is proportional to the level of the accumulated signal such that the perceived optic flow decreases to zero immediately before touchdown, as illustrated in Figure 2.19.

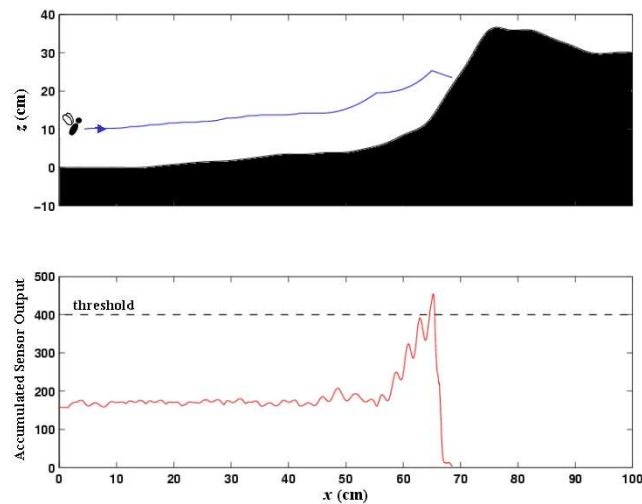


Figure 2.19: The insect releases a landing response when the time-accumulated optic flow signal exceeds a threshold. The insect decelerates such that the perceived optic flow reduces quickly as it approaches the landing site.

An extension to the landing response is the terrain following maneuver in flying insects. When searching for a landing site, a flying insect must navigate through its environment, avoid obstacles, and eventually approach the desired location. Therefore, before its brain issues a landing command, the insect will not attempt to land even if the optic

flow signal accumulates to the level sufficient to trigger a landing response. As shown in Figure 2.20, the insect follows a simple topography of the ground. When the insect is closer to the ground, the pattern on the ground cause the optic flow to rise. An upper threshold for the perceived optic flow is selected such that when this value is reached, the insect will ascend in order to maintain a safe distance to the ground. On the other hand, when the insect is at a higher position, the pattern on the ground does not induce significant optic flow, resulting in the accumulated signal to decrease due to the leakage. Accordingly, the insect will descend when a preset lower threshold is attained. In real insects, the activation of the motor system upon receiving an ascending or descending command is much faster than the visual processing time. In robot navigation, the choices of the upper and lower threshold levels will depend on the responsiveness of the motor system in order to properly follow the topography of the terrain.

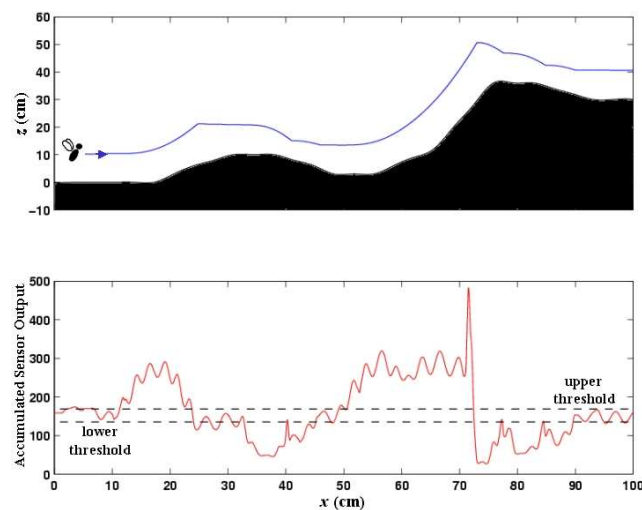


Figure 2.20: The insect follows the topography of the terrain based on the perceived optic flow during its flight. The insect ascends when the accumulated signal exceeds an upper threshold and descends when the accumulated signal drops below a lower threshold. As a result, the insect is able to maintain a fairly constant distance above the ground.

2.5 Elementary Motion Detectors for Obstacle Avoidance

In the previous sections, it has been demonstrated that optic flow sensors are useful for a number of applications in robot navigation. However, for the current application of the MFI, an optic flow sensor on a simple scale will be sufficient for use in obstacle

avoidance. When the raw optic flow measured by the sensor reaches a predetermined value, this indicates that an object is close and the MFI can use such a signal to perform necessary maneuvers (e.g., steering away from the object or decreasing forward speed). To this end, a minimum number of photoreceptors is used in the realization of such a sensor. Specifically, the EMD architecture described in Section 2.2 has been implemented. The left panel of Figure 2.21 shows the completed EMDs consisting of a two-by-two photodiode array for use on the MFI.

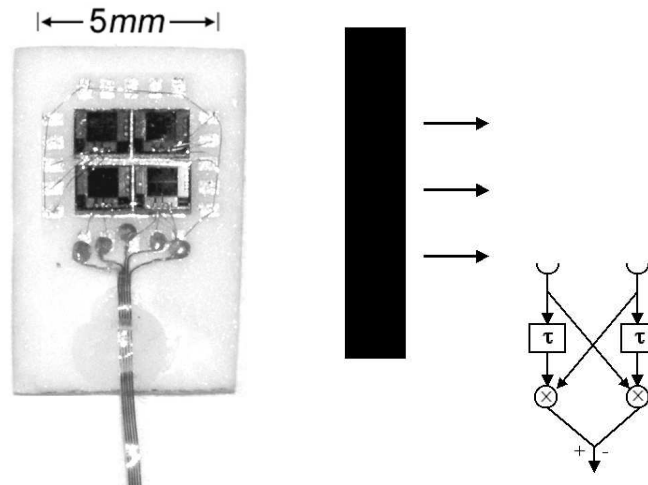


Figure 2.21: Photo of the EMDs consisting of a two-by-two photodiode array (*left*). Test setup for the EMDs to a simulated obstacle (*right*). A black stripe on a white background is moving toward the EMDs, mimicking an approaching object.

In order to test whether this simple device can detect the optic flow induced by a moving object, a black stripe on a white background is used to simulate an approaching obstacle. It is moved across the EMDs as illustrated in the right panel of Figure 2.21. Signals from the individual photodiodes are recorded and processed off-line using the delay-and-correlate operation. The response can be seen in Figure 2.22. This result shows a successful measurement of the optic flow by the EMDs and thus it should be useful in simple tasks such as obstacle avoidance. Furthermore, although only one dimensional test is performed, the two dimensional arrangement of the photodiodes allows the MFI to avoid collision when moving in space because the sensor can detect optic flow induced by approaching objects in orthogonal directions.

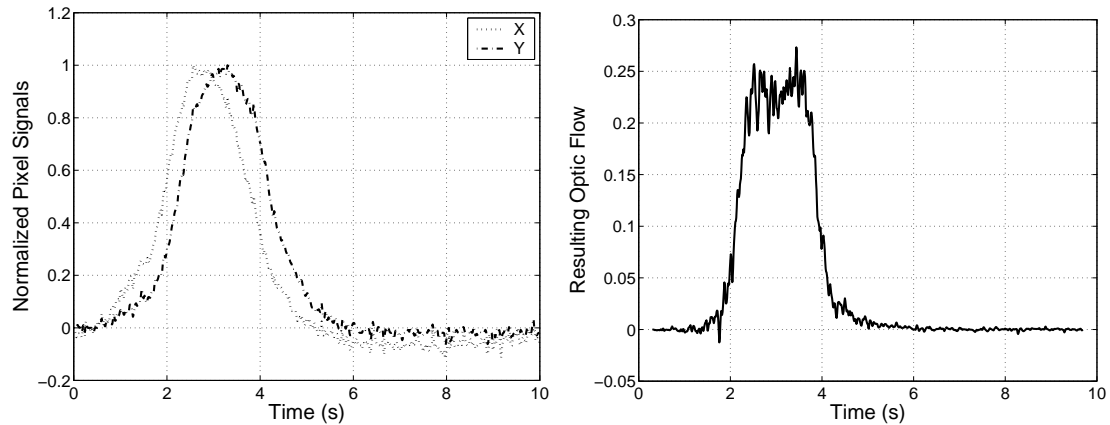


Figure 2.22: Signals registered by the individual photodiodes as the black stripe approaches the EMDs (*left*). The resulting optic flow measurement by the EMDs (*right*).

2.6 Chapter Summary and Discussion

Image motion seen by an insect's eyes is encoded in the optic flow. In this chapter, optic flow sensors based on the visual system of flying insects are modeled and simulated. The sensor consists of a one dimensional array of elementary motion detectors (EMDs) which use the Hassenstein-Reichardt correlation type of motion detection algorithm to compute optic flow, a local measurement of light intensity motion across the photoreceptors. This correlation-based model has been proven to be an excellent description of the motion detection mechanism in both insects and vertebrates. It exhibits the characteristics of strong directional selectivity of image motion and robustness against noisy stimuli. In addition, it is capable of encoding image speed using a slightly modified version (i.e., the half-detector configuration). These properties of the sensor model enables the reproduction of many visually mediated flight behaviors observed in real insects. Therefore, vision sensors of this type may be potentially useful in robot navigation for which conventional motion detection systems are not suitable. Table 2.1 summarizes the simulations of insect flight behaviors and their sensing techniques presented in this chapter. In addition, a simple optic flow sensor has been created for use on the MFI in tasks such as obstacle avoidance. This sensor, based on the presented EMD architecture, consists of a two-by-two photodiode array. Despite simplicity, the experimental result shows an excellent response of the sensor to the optic flow induced by a simulated obstacle.

While a one dimensional array of EMDs is sufficient to measure optic flow induced

	Detector Type	Signal Type	Operation
Optomotor Response	standard detector	instantaneous	Reduce the combined outputs from the left and right sensors
Centering Response	half detector	instantaneous	Balance the outputs between the left and right sensors
Regulation of Flight Speed	half detector	instantaneous	Hold constant the outputs from the left and right sensors
Visual Odometry	half detector	accumulated	Estimate the distance flown using the integrated outputs from the left and right sensors
Obstacle Avoidance	standard detector	accumulated	Turn away from the side of the sensor whose integrated output exceeds a threshold
Landing Response	half detector	accumulated	Land on the object when the integrated output from the downward-facing sensor exceeds a threshold

Table 2.1: Summary of the visual sensing schemes in the simulations of the insect flight behaviors.

by planar motion, a two dimensional array of EMDs is necessary to detect optic flow induced by motion in space. In order to reduce computational load in extracting self-motion information from a two dimensional optic flow sensor, an additional stage of matched filters, each of which is tuned to a particular feature of the optic flow pattern as that seen in an insect’s tangential neurons [30, 65], needs to be implemented before the spatial summation step. Therefore, as more stages of pixel-parallel processing are incorporated in the design, two dimensional neuromorphic vision systems are primarily being fabricated in a modular multi-chip architecture which uses a type of interchip communications protocol envisioned as a circuit analogy to the optic nerve (a review can be found in [41]). Furthermore, the field of view of such visual system is determined by the lens mounted over the sensor chip, which is much smaller than the visual field seen by a compound eye of real insects. Chahl

and Srinivasan [14] have developed a specially shaped mirror assembly which can provide a panoramic view of the environment to a camera. This technique may also be applied to neuromorphic vision systems to increase the effective field of view of the sensor chip. Finally, insects possess high level visual capacities, such as pattern recognition and color perception, in addition to the optic flow perception. Honeybees, for example, can learn rather general features of flowers and landmarks and apply them to distinguish between objects that they have never previously encountered [87]. They can learn to negotiate complex mazes with the aid of landmarks or symbolic signposts [115]. Honeybees are also capable of associative recall, a whiff of a scent can trigger recall of an associated color or vice versa [96]. All of these capabilities would certainly be of value in assisting navigation and should not be overlooked when considering complex visually-mediated behaviors in insects.

Chapter 3

Orientation Sensors

Flying insects maintain their spatial orientation about the roll, pitch, and yaw axes using a variety of sensory systems which include inertial organs, aerodynamic sense organs, and visual systems. In addition to the compound eyes, the visual systems of many adult insects include three smaller simple eyes called ocelli (see Figure 3.1). Unlike the compound eyes, each ocellus has only one cuticular lens which produces an under-focused image on the retina [17]. Additionally, the neural elements which are involved in conveying visual information from the ocelli to descending neurons are more simply arranged than the corresponding compound eye elements [107]. Therefore, ocelli do not detect images nor sense anything other than changes in the level of illumination in the surrounding. Nonetheless, ocelli have large, overlapping visual fields, and they are oriented in such a way that they receive illumination from different regions of the environment. The arrangement of ocelli in different insect species varies. In locusts and dragonflies, the ocelli are located in the frontal part of the head, whereas those in flies and bees are located in the dorsal part. Such a morphological difference may imply different functions of the ocelli in these insects (see [103] for a review). Although the contribution of ocelli in insect flight is not as well characterized as that of compound eyes, it is generally accepted that ocelli play a fundamental role in assisting visual flight stabilization, as they are better developed in strongly flying insect species [17, 45, 100, 101, 107].

3.1 Observations of Ocellar Contribution

Experimental observations on several insect species suggest that ocelli collaborate synergistically with compound eyes to mediate visual head stabilization over a wide range

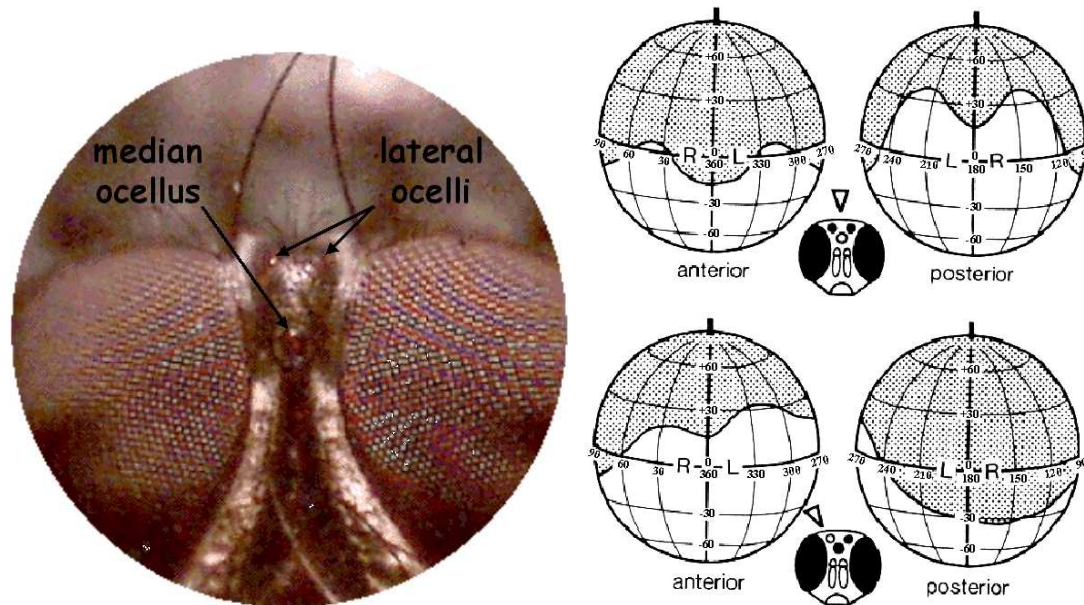


Figure 3.1: Ocelli of the blowfly *Calliphora*. (Left) Upper part of the head viewed from the front with a pair of large multi-faceted compound eyes at either side and three simple eyes (ocelli) arranged in a triangle on top of the head between the compound eyes. Courtesy of D.A. Kendall; <http://www.kendall-bioresearch.co.uk/>. (Right) The stippled areas represent the visual fields of the median ocellus (top) and right lateral ocellus (bottom) in a blowfly. On the left is represented the part of the visual field within the anterior hemisphere, and on the right the part in the posterior hemisphere. Adapted from [80].

of conditions. When an insect is presented with a moving artificial horizon, it first tries to rotate its head in order to fixate the horizon on its retinas. Only afterwards does it change its wingbeat pattern to realign its abdomen with its head. Taylor [100] observed that cauterization of ocelli doubles the latency between the horizon motion and the compensatory head movement in locusts. Schuppe and Hengstenberg [80] showed that ocelli contribute to the control of the initial phase of the dorsal light response in blowflies, whereas the compound eyes mediate mainly the steady state phase. Moreover, in dimly lit environments or when no sharp horizontal boundary is present, ablation of ocelli also reduce the insect's sensitivity to horizon motion, resulting in a delayed head motion and a smaller mean amplitude of the response [100]. It should be pointed out that under heavily overcast conditions, as in forests, or in dark nights when many insects fly, the sharpness of the horizon border is considerably reduced. The ability of ocelli to distinguish “up” on these occasions may be an important reason for their apparent duplication of compound eye function. Ocelli seem to be designed for high sensitivity and speed of response at the expense of visual acuity.

Therefore, it can be stated that ocelli are especially useful for stabilization of the retinal image of the compound eyes during flight when disturbances are sudden and frequent or at low level of illumination.

Two additional findings are particularly relevant to the modeling of an ocelli system. First, in the case of ablated compound eyes and intact ocelli, an inverted horizon corresponding to an upside down insect orientation caused no head motion unless the two lateral ocelli were unequally illuminated, unlike insects with intact compound eyes. This observation is consistent with the mathematical modeling of ocelli developed in the following section, which predicts an unstable equilibrium configuration for the upside down orientation. Second, insects with compound eyes disconnected and intact ocelli responded quickly to sudden horizon displacements, but then soon relaxed toward the rest position even when the horizon remained displaced. In other cases, insects with intact compound eyes maintained a rotated head position. This observation suggests that the ocelli behave similarly to a high pass filter. This can be motivated by the fact that the light distribution in the surrounding can change substantially during the course of a day due to the change in sun position, atmospheric variation, or simply because the insect traverses shady trees or urban environments during its flight. Nonetheless, these variations have a long timescale when compared to the timescale of insect motion and can be compensated for by the signals from the compound eyes. From an engineering perspective, flying insects combine low bandwidth, high resolution compound eyes with high bandwidth, low resolution ocelli to obtain an optimal visual sensory system for attitude stabilization over a large frequency domain.

Biologists believe that insects use the different photoreceptors in their ocelli to detect the brightness in the corresponding visual fields so that the insects can estimate their orientation relative to the sky. Their argument is based on the assumption that, as a first approximation, the intensity of light I measured by the photoreceptors is mainly a function of the latitude θ relative to the light source (i.e., the sky). Thus, by turning their dorsal side toward the brightest region, insects can maintain a right-side up posture during flight in natural environments.

Although the ocelli of real insects consist of three photoreceptors, an ocelli system that uses four photoreceptors is considered in this chapter because the design concept is intuitive and the mathematical modeling becomes elegant. Nevertheless, all the results derived for the four-photoreceptor ocelli system can be modified to describe the three-

photoreceptor configuration as well.

3.2 Ocelli Modeling

It is necessary to introduce the coordinate transformation scheme used in the ocelli modeling before entering the discussion. The matrix $R \in SO(3) = \{R \in \mathbb{R}^{3 \times 3} : R^T R = I, \det R = +1\}$ is a rotation matrix representing the orientation of the insect's body frame \mathcal{B} relative to a fixed frame \mathcal{A} . In particular, let $\mathbf{v}^b = [x^b, y^b, z^b]^T$ and $\mathbf{v}^a = [x^a, y^a, z^a]^T$ be the coordinates of a vector $\mathbf{v} \in \mathbb{R}^3$ relative to the body frame \mathcal{B} and the fixed frame \mathcal{A} , respectively. Then, the coordinate transformations of vectors between the body frame and the fixed frame are given by:

$$\begin{aligned}\mathbf{v}^a &= R\mathbf{v}^b \\ \mathbf{v}^b &= R^T\mathbf{v}^a\end{aligned}$$

For example, let $\mathbf{e}_3 = [0, 0, 1]^T$ represent a z -axis unit vector, then the coordinates of the z -axis unit vector in the body frame relative to the fixed frame can be computed by:

$$P_z^a = R\mathbf{e}_3 = [r_{13}, r_{23}, r_{33}]^T \quad (3.1)$$

and the coordinates of the z -axis unit vector in the fixed frame relative to the body frame can be computed by:

$$P_z^b = R^T\mathbf{e}_3 = [r_{31}, r_{32}, r_{33}]^T \quad (3.2)$$

where r_{ij} is the $i-j$ entry of the rotation matrix R . Furthermore, $P_z^b \neq P_z^a$ in general. Also, an important property of such a transformation, which follows directly from the definition of the rotation matrix R , is that it preserves length. Specifically:

$$\begin{aligned}\|P_z^a\|^2 &= r_{13}^2 + r_{23}^2 + r_{33}^2 = 1 \\ \|P_z^b\|^2 &= r_{31}^2 + r_{32}^2 + r_{33}^2 = 1\end{aligned}$$

Any point P in the sky can be represented in spherical coordinates (r, θ, ψ) where $r \in [0, +\infty)$ is the radius of the celestial sphere, $\theta \in [0, \pi]$ is the latitude, and $\psi \in [0, 2\pi]$ is the longitude, relative to the fixed frame \mathcal{A} . Alternatively, this same point can be written in Cartesian coordinates as $P = [x_P, y_P, z_P]^T$. The transformation from spherical to Cartesian coordinates is given by:

$$\begin{aligned}x_P &= r \sin \theta \cos \psi \\ y_P &= r \sin \theta \sin \psi \\ z_P &= r \cos \theta\end{aligned} \quad (3.3)$$

Without loss of generality, the radius of the celestial sphere can be normalized to unity (i.e., $r = 1$). The ocelli sensory system is modeled as four ideal photoreceptors, denoted by P_1, P_2, P_3 , and P_4 , which are fixed with respect to the insect's body frame \mathcal{B} . They measure the intensity of light averaged over their visual field in the sky. They are arranged symmetrically with the same latitude such that if their axes are drawn, one would see that the axes form an inverted pyramid whose top vertex is placed at the center of the insect's head. Formally, their orientation relative to the body frame can be represented in Cartesian coordinates as follows:

$$\begin{aligned} P_1^b &= [\sin \alpha, 0, \cos \alpha]^T, & P_2^b &= [-\sin \alpha, 0, \cos \alpha]^T \\ P_3^b &= [0, \sin \alpha, \cos \alpha]^T, & P_4^b &= [0, -\sin \alpha, \cos \alpha]^T \end{aligned} \quad (3.4)$$

where the parameter $\alpha \in (0, \pi)$ sets the latitude of the photoreceptors. Every photoreceptor collects light from a conic region A_i in the sky as shown in Figure 3.2.

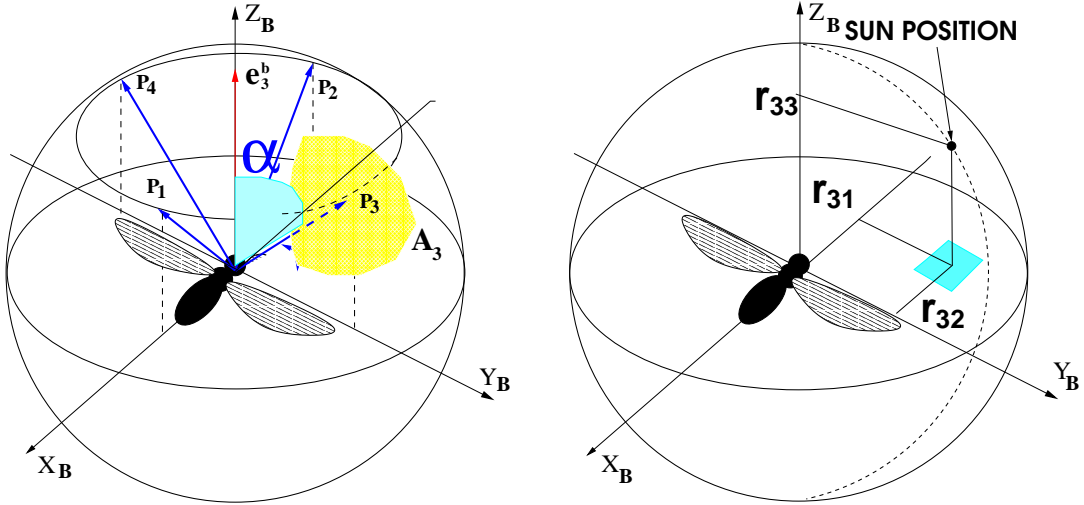


Figure 3.2: (Left) Four photoreceptors, P_1, P_2, P_3 , and P_4 , are fixed with respect to the insect's body frame (x^b, y^b, z^b) . The shadowed area, A_3 , represents the receptive field of P_3 . (Right) The projection of the light source onto the $x - y$ plane of the insect's body frame. The shadowed area represents the region enclosed by the inequalities in Equation (3.10).

The most important assumption made in the ocelli modeling is that the intensity of light I measured by the photoreceptor P_i is *independent* of its longitude and is a *strictly monotonically decreasing* function of its latitude relative to the fixed frame. Formally, it can be written as:

$$\begin{aligned} I(P_i) &= I(\psi_i, \theta_i) = I(\theta_i) \\ \theta_1 < \theta_2 &\Rightarrow I(\theta_1) > I(\theta_2) \end{aligned} \quad (3.5)$$

where, with an abuse of notation, the position of the photoreceptor is identified by its latitude θ , which is the angle between the z -axis of the fixed frame and the orientation of the photoreceptor on the celestial sphere.

The assumption of monotonic distribution of light intensity on the celestial sphere can only be satisfied in an ideal environment where the landscape is uniform and the light is diffused uniformly around its generating source. However, in real world environments, it is more common to find less than ideal conditions such as time-varying atmospheric conditions, shade from trees or buildings, or multiple light sources indoor. In order to investigate how the ocelli system will perform under real world conditions, a photodiode is placed about 50 *cm* above the ground in three different environments that represent typical scenarios: inside a room illuminated by multiple lamps on the ceiling, outdoor between buildings that are blocking the sunlight, and outdoor in an open space at daytime. The output from this photodiode faced at different orientations is then used to generate the light intensity map of the celestial sphere as shown in Figure 3.3. To facilitate the comparison of light intensity for heterogeneous environments, the light intensity in these three plots is normalized so that $I_{max} = 1$ and $I_{min} = -1$. Although the light intensity is not strictly monotonic and it is not independent of the longitude, it is still possible to spot a bright portion in the upper hemisphere opposed to a dark one in the lower hemisphere in all three scenarios.

In the indoor environment, the orientation of the brightest region is exactly perpendicular to the horizontal plane, whereas in the outdoor scenarios this orientation is slightly tilted. In the case of urban environment, the bright region is tilted because a large building is screening the sunlight, while in the open space environment, the tilt is caused by the position of the sun close to the horizon (see the photos in Figure 3.3). The consequences on the orientation estimation of ocelli caused by these non-ideal scenarios will be addressed in Section 3.2.1.

The measurements from the four photoreceptors in the ocelli system are simply subtracted pairwise and these two signals are the outputs from the ocelli:

$$\begin{aligned} y_1^o &= I(P_1^a) - I(P_2^a) \\ y_2^o &= I(P_3^a) - I(P_4^a) \end{aligned} \tag{3.6}$$

where P_i^a is the orientation of the photoreceptor in Cartesian coordinates relative to the fixed frame. Given the orientation $R \in SO(3)$ of the insect's body frame \mathcal{B} relative to the fixed frame \mathcal{A} , the orientation of the photoreceptor P_i relative to the fixed frame is $P_i^a = RP_i^b$. Since the orientation of the photoreceptors is fixed with respect to the body

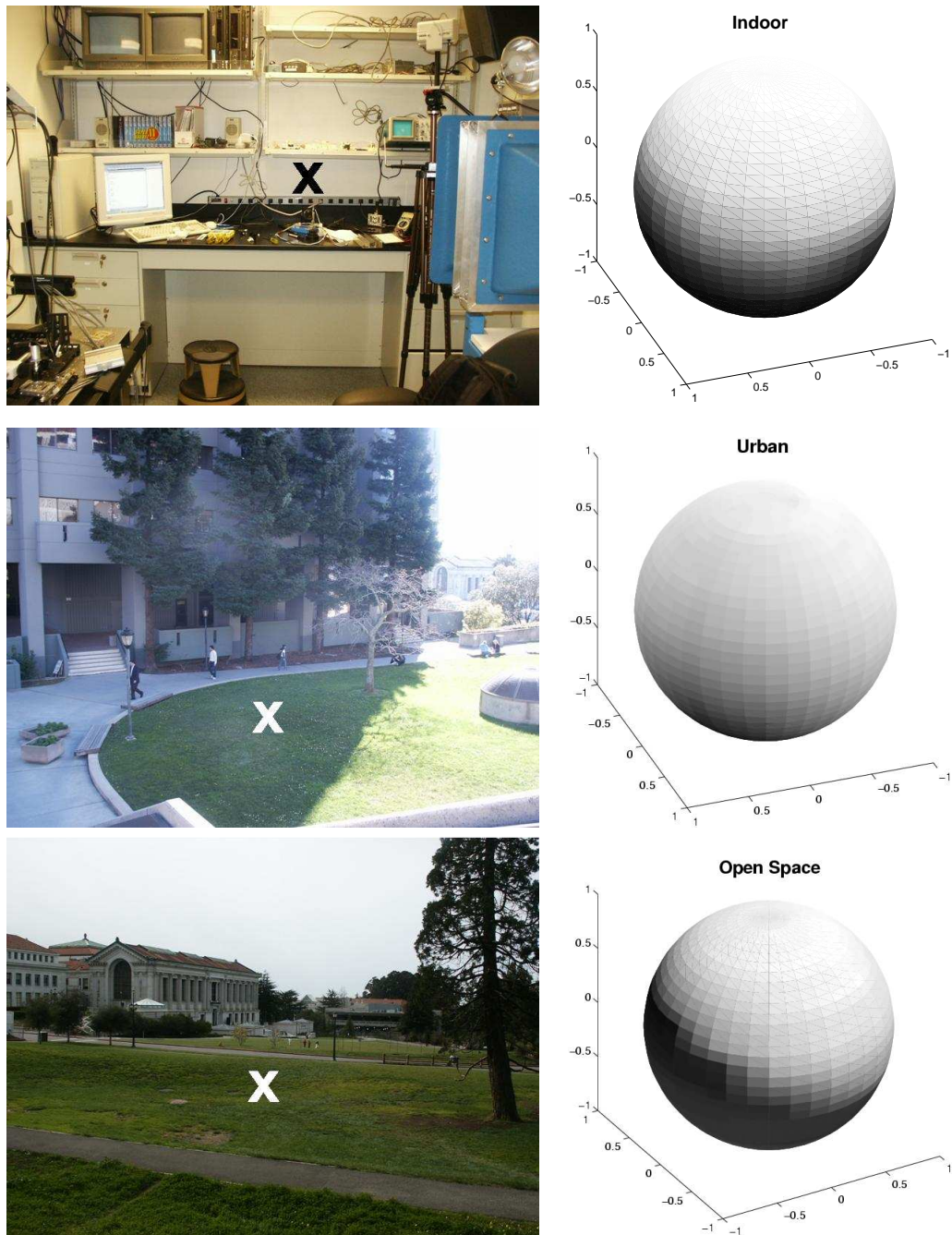


Figure 3.3: Light intensity distributions over the celestial sphere: indoor environment (*top*), urban environment (*middle*), and open space environment (*bottom*). Data is obtained from the measurements using a single photodiode, shown in Figure 3.12, faced at different orientations. The plots on the right hand side are generated by interpolating (but not smoothing) the light intensity data on a uniform grid of 100 points collected at locations marked by “X” in the pictures on the left hand side.

frame, the outputs from the ocelli are dependent only on the insect orientation R . From a mathematical point of view, the operation of the ocelli system can be considered as a nonlinear function $f : SO(3) \rightarrow \mathbb{R}^2$ of the insect orientation.

3.2.1 Orientation Estimation

It will be necessary to study the general properties of the map $f(\cdot)$ in order to understand how much information about the insect orientation can be extracted from the ocellar outputs. First, a special case, where the light intensity measured by the photoreceptors is $I(\theta) = \cos \theta$, will be examined. This instance clearly highlights the relation between the insect orientation R and the ocellar outputs y_i^o . The general case, where $I(\theta)$ is simply monotonic, will be considered next.

Proposition 3.2.1. *Suppose that the light intensity measured by the photoreceptors is $I(\theta) = \cos \theta$, and let the orientation of the photoreceptors be such that $\alpha = \frac{\pi}{6}$ in Equations (3.4). Then the outputs from the ocelli are $y_1^o = r_{31}$ and $y_2^o = r_{32}$, where r_{ij} is the $i - j$ entry of the insect orientation matrix R .*

Proof. Substituting $I(\theta) = \cos \theta$ into Equations (3.6):

$$\begin{aligned}
 y_1^o &= I(P_1^a) - I(P_2^a) = \cos \theta_{P_1^a} - \cos \theta_{P_2^a} \\
 &= \mathbf{e}_3^T P_1^a - \mathbf{e}_3^T P_2^a = \mathbf{e}_3^T R P_1^b - \mathbf{e}_3^T R P_2^b \\
 &= \mathbf{e}_3^T R (P_1^b - P_2^b) \\
 &= \mathbf{e}_3^T R \left[\sin \frac{\pi}{6}, 0, \cos \frac{\pi}{6} \right]^T - \left[-\sin \frac{\pi}{6}, 0, \cos \frac{\pi}{6} \right]^T \\
 &= \mathbf{e}_3^T R \mathbf{e}_1 = r_{31} \\
 y_2^o &= \dots = \mathbf{e}_3^T R (P_3^b - P_4^b) = \mathbf{e}_3^T R \mathbf{e}_2 = r_{32}
 \end{aligned}$$

where $\mathbf{e}_1 = [1, 0, 0]^T$, $\mathbf{e}_2 = [0, 1, 0]^T$, and $\mathbf{e}_3 = [0, 0, 1]^T$. The second line follows from the fact that $\cos \theta_{P_i^a} = z_{P_i} = \mathbf{e}_3^T P_i^a$ and $P_i^a = R P_i^b$. \square

From Equation (3.2), r_{31} and r_{32} correspond to the x and y coordinates of the z -axis of the fixed frame \mathcal{A} relative to the body frame \mathcal{B} . In other words, the ocelli can measure the x and y positions of the light source relative to the insect's body frame (the square region shown in the left panel of Figure 3.2). Intuitively, this information can be exploited to rotate the insect body toward the light source.

When the light intensity $I(\theta)$ measured by the photoreceptors is just a *monotonically decreasing* function of the latitude, the ocelli do not estimate the exact orientation of

the light source relative to the insect's body frame, but they can still retrieve the approximate direction, as shown in the following proposition:

Proposition 3.2.2. *Suppose that the light intensity, $I(\theta)$, measured by the photoreceptors is an unknown, monotonically decreasing function of the latitude θ . Then the outputs from the ocelli have the following properties:*

$$\begin{aligned} y_1^o = 0 &\iff r_{31} = 0; & y_1^o \neq 0 &\implies y_1^o r_{31} > 0 \\ y_2^o = 0 &\iff r_{32} = 0; & y_2^o \neq 0 &\implies y_2^o r_{32} > 0 \end{aligned} \quad (3.7)$$

Proof. First recall that $\cos^{-1}(\cdot)$ is a strictly monotonically decreasing function of its argument on the interval $(-1, 1)$, and that the composition of two monotonically decreasing functions is a monotonically increasing function. Therefore, $\tilde{I}(\theta) = I \circ \cos^{-1}(\theta)$ is a monotonically increasing function. Consider the first ocellar output y_1^o :

$$\begin{aligned} y_1^o &= I(\theta_{P_1^a}) - I(\theta_{P_2^a}) \\ &= I(\cos^{-1}(\mathbf{e}_3^T P_1^a)) - I(\cos^{-1}(\mathbf{e}_3^T P_2^a)) \\ &= \tilde{I}(\mathbf{e}_3^T P_1^a) - \tilde{I}(\mathbf{e}_3^T P_2^a) \\ &= \tilde{I}(\mathbf{e}_3^T R P_1^b) - \tilde{I}(\mathbf{e}_3^T R P_2^b) \\ &= \tilde{I}(r_{31} \sin \alpha + r_{33} \cos \alpha) - \tilde{I}(-r_{31} \sin \alpha + r_{33} \cos \alpha) \end{aligned} \quad (3.8)$$

where the second line follows from $\cos \theta_{P_i^a} = z_{P_i} = \mathbf{e}_3^T P_i^a$, and the orientations P_i^b of the photoreceptors are given by Equations (3.4). Since the function \tilde{I} is monotonically increasing, it follows that:

$$\begin{aligned} y_1^o > 0 &\implies \tilde{I}(r_{31} \sin \alpha + r_{33} \cos \alpha) > \tilde{I}(-r_{31} \sin \alpha + r_{33} \cos \alpha) \\ &\implies r_{31} \sin \alpha + r_{33} \cos \alpha > -r_{31} \sin \alpha + r_{33} \cos \alpha \\ &\implies 2 r_{31} \sin \alpha > 0 \implies r_{31} > 0 \end{aligned}$$

where the second line uses the fact that \tilde{I} is monotonically increasing and that $\sin \alpha > 0$. Analogously, it is easy to verify that $y_1^o < 0 \implies r_{31} < 0$. From monotonicity of \tilde{I} , it also follows that $y_1^o = 0 \implies r_{31} = 0$. Trivially, from Equation (3.8) it follows that $r_{31} = 0 \implies y_1^o = 0$. Finally, the same arguments can be applied to prove the properties of the second ocellar output y_2^o . \square

This proposition indicates that the ocelli still give an approximate orientation of the light source regardless of the exact orientation of the photoreceptors relative to the insect

body and regardless of the specific light intensity distribution as long as it is monotonic. Moreover, the outputs of the ocelli are zero if and only if the z -axes of the fixed and body frames are aligned. A more intuitive understanding of the ocellar processing is given by the following lemma:

Lemma 3.2.1. *Suppose that the light intensity, $I(\theta)$, measured by the photoreceptors is an unknown smooth differentiable, monotonically decreasing function of the latitude θ . Let $P_z^b = [r_{31}, r_{32}, r_{33}]^T$ represent the orientation of the z -axis unit vector of the fixed frame relative to the body frame, and let ψ^b and θ^b represent the longitude and latitude of the vector P_z^b relative to the body frame, respectively. Also let $\hat{\psi}^b$ represent the longitude of the vector $\mathbf{y}_O = [y_1^o, y_2^o, 0]^T$. Then:*

$$|\hat{\psi}^b - \psi^b| < \frac{\pi}{2}, \quad \text{for } \mathbf{y}_O \neq \mathbf{0} \quad (3.9)$$

$$\underline{a} r_{31} \leq y_1^o \leq \bar{a} r_{31}; \quad \underline{a} r_{32} \leq y_2^o \leq \bar{a} r_{32} \quad (3.10)$$

$$\theta^b \rightarrow 0 \implies \begin{cases} y_1^o \rightarrow a r_{31} \\ y_2^o \rightarrow a r_{32} \\ \hat{\psi}^b \rightarrow \psi^b \\ \|\mathbf{y}_O\| \rightarrow a \sin \theta^b \end{cases} \quad (3.11)$$

where $0 < \underline{a} \leq a \leq \bar{a} < \infty$

Proof. According to the transformation from spherical to Cartesian coordinates given in Equations (3.3), it can be written as:

$$\begin{aligned} \sin \psi^b &= \frac{r_{31}}{\sqrt{r_{31}^2 + r_{32}^2}}; & \cos \psi^b &= \frac{r_{32}}{\sqrt{r_{31}^2 + r_{32}^2}} \\ \sin \hat{\psi}^b &= \frac{y_1^o}{\sqrt{y_1^{o2} + y_2^{o2}}}; & \cos \hat{\psi}^b &= \frac{y_2^o}{\sqrt{y_1^{o2} + y_2^{o2}}} \end{aligned}$$

Therefore, if $(y_1^o, y_2^o) \neq (0, 0)$,

$$\begin{aligned} \cos(\psi^b - \hat{\psi}^b) &= \cos \psi^b \cos \hat{\psi}^b + \sin \psi^b \sin \hat{\psi}^b \\ &= \frac{r_{31}y_1^o + r_{32}y_2^o}{\sqrt{(y_1^{o2} + y_2^{o2})(r_{31}^2 + r_{32}^2)}} > 0 \end{aligned} \quad (3.12)$$

where the inequality follows from Proposition 3.2.2, and it implies Equation (3.11). For $\mathbf{y}_O = \mathbf{0}$, the longitude is ill-defined because it corresponds to a point of singularity of the spherical coordinate representation.

If $r_{31} > 0$, it follows from Equation (3.8):

$$\begin{aligned}
y_1^o &= \tilde{I}(r_{33} \cos \alpha) + r_{31} \sin \alpha \frac{d\tilde{I}(\xi_1)}{d\theta} - [\tilde{I}(r_{33} \cos \alpha) - r_{31} \sin \alpha \frac{d\tilde{I}(\xi_2)}{d\theta}] \\
&= r_{31} \sin \alpha \left[\frac{d\tilde{I}(\xi_1)}{d\theta} + \frac{d\tilde{I}(\xi_2)}{d\theta} \right] \\
\implies 2\underline{a} r_{31} \sin \alpha &\leq y_1^o \leq 2\bar{a} r_{31} \sin \alpha
\end{aligned} \tag{3.13}$$

where $\xi_1 \in [r_{33} \cos \alpha, r_{33} \cos \alpha + r_{31} \sin \alpha]$ and $\xi_2 \in [r_{33} \cos \alpha - r_{31} \sin \alpha, r_{33} \cos \alpha]$ come from the mean value function theorem and the inequalities are due to the assumption that $0 < \underline{b} \leq \frac{d\tilde{I}}{d\theta} \leq \bar{b} < \infty$ is smooth with nonnegative bounded first derivative. These inequalities lead directly to Equations (3.10).

According to Equations (3.3), $r_{33} = \cos \theta^b$, $|r_{31}| \leq \sin \theta^b$, $|r_{32}| \leq \sin \theta^b$. Therefore, $(\theta^b \rightarrow 0) \Rightarrow (P_z^b = [r_{31}, r_{32}, r_{33}]^T \rightarrow \mathbf{e}_3 = [0, 0, 1]^T)$. Also, $(\theta^b \rightarrow 0) \Rightarrow (\xi_1 \rightarrow \cos \alpha; \xi_2 \rightarrow \cos \alpha)$. Therefore, from Equation (3.13), $(y_1^o \rightarrow ar_{31})$ where $a = 2 \frac{d\tilde{I}(\cos \alpha)}{d\theta} \sin \alpha$. Analogously, $(\theta^b \rightarrow 0) \Rightarrow (y_2^o \rightarrow ar_{32})$.

Equation (3.12) can be expanded in Taylor's series with respect to the variables $P_z^b = [r_{31}, r_{32}, r_{33}]^T$ at the point \mathbf{e}_3 :

$$\begin{aligned}
\cos(\psi^b - \hat{\psi}^b) &= \frac{ar_{31}^2 + ar_{32}^2}{\sqrt{a^2(r_{31}^2 + r_{32}^2)(r_{31}^2 + r_{32}^2)}} + o(\|P_z^b - \mathbf{e}_3\|) \\
&= 1 + o(\|P_z^b - \mathbf{e}_3\|)
\end{aligned}$$

Therefore, $\theta^b \rightarrow 0 \Rightarrow \|P_z^b - \mathbf{e}_3\| \rightarrow 0 \Rightarrow \cos(\psi^b - \hat{\psi}^b) \rightarrow 1 \Rightarrow (\psi^b - \hat{\psi}^b) \rightarrow 0$. Finally, the magnitude of the output vector can be written as:

$$\begin{aligned}
\|\mathbf{y}_O\| &= \sqrt{y_1^{o2} + y_2^{o2}} = a\sqrt{r_{31}^2 + r_{32}^2} + o(\|P_z^b - \mathbf{e}_3\|) \\
&= a\sqrt{1 - r_{33}^2} + o(\|P_z^b - \mathbf{e}_3\|) \\
&= a\sqrt{1 - \cos^2 \theta^b} + o(\|P_z^b - \mathbf{e}_3\|) \\
&= a \sin \theta^b + o(\|P_z^b - \mathbf{e}_3\|)
\end{aligned}$$

where the identity $r_{31}^2 + r_{32}^2 + r_{33}^2 = 1$ is used. Therefore, $\theta^b \rightarrow 0 \Rightarrow \|P_z^b - \mathbf{e}_3\| \rightarrow 0 \Rightarrow \|\mathbf{y}_O\| \rightarrow a \sin \theta^b$. \square

This lemma highlights several important features of the ocellar outputs. First, according to Equation (3.11), the ocelli *always* give an approximate estimation of the latitude of the light source relative to the insect body, in the sense that if the insect rotates toward the apparent position of the light source, it will eventually align the z -axes of the body and

fixed frames. In addition, for small latitudes θ^b , the longitude estimation error of the light source decreases to zero and the magnitude of the output vector \mathbf{y}_O becomes proportional to the latitude. This means that the ocellar outputs can be used to estimate not only the direction of the light source but also the distance in terms of the latitude.

Figure 3.4 gives a pictorial representation of the ocellar outputs for the light intensity function $I(\theta) = \cos^5 \theta$. The plot on the top displays the longitude estimation error $\Delta\psi^b$ against the latitude for different longitudes, and the plot at the bottom displays the magnitude of the output vector as a function of the latitude for different longitudes. As expected, the longitude estimation error is always smaller than 90° and goes to zero as the latitude goes to zero. The magnitude of the output vector is always positive except for the two points $\theta^b = \{0, \pi\}$, and it is clearly proportional to the *sine* of the latitude for small angles.

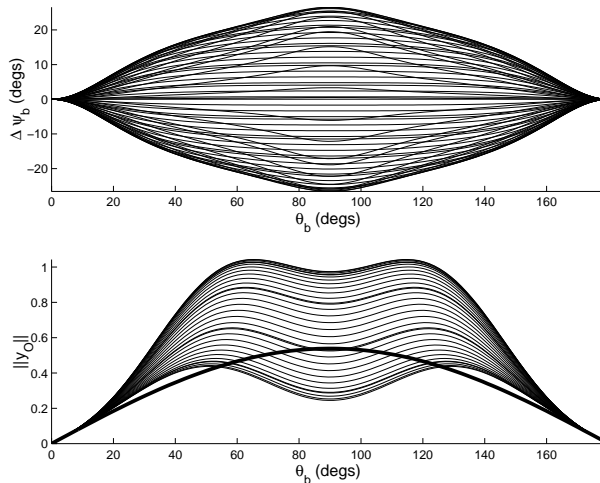


Figure 3.4: Longitude estimation error, $\Delta\psi^b = \psi^b - \hat{\psi}^b$, and the magnitude of the ocellar output vector, $\|\mathbf{y}_O\|$, as a function of the latitude θ of the light source position relative to the insect body for the light intensity $I(\theta) = \cos^5(\theta)$. Each trace corresponds to a different longitude ψ . The thick line in the lower plot is given by the function $f = a \sin \theta^b$ in Equation (3.11).

3.2.2 Simulation

A graphical representation of the ocelli performance as it seeks the light source position is given by the virtual torque field induced by the ocellar outputs. This is visualized as if the z -axis of the insect's body frame is being attracted toward the apparent light source

position with magnitude of attraction proportional to the ocellar outputs. Formally, this induced force field can be written as:

$$\begin{aligned}\boldsymbol{\tau}_y &= -\mathbf{e}_3 \times \mathbf{y}_O = [-y_2^o, y_1^o, 0]^T \\ \mathbf{F}_y &= P_z^b \times \boldsymbol{\tau}_y\end{aligned}\tag{3.14}$$

The upper plots of Figure 3.5 show the virtual force field induced by the ocellar outputs for the ideal light intensity function $I(\theta) = \cos\theta$. Clearly, the ocelli estimate the exact orientation of the light source relative to the insect body and hence they can steer the insect’s body frame directly toward the north pole, as suggested by Proposition 3.2.1. When the light intensity function is given by $I(\theta) = \cos^5\theta$, as depicted in the lower plots of Figure 3.5, the magnitude and direction of the induced force vectors change for different latitudes and longitudes. Nevertheless, this field would still be able to move the insect’s body frame toward the light source position, as suggested by Proposition 3.2.2.

The force fields using the light intensity distributions in the three real world scenarios shown in Figure 3.3 are also calculated. The force field for the indoor setting is similar to the ideal case where all vectors are pointing directly to the north pole (see the upper plot of Figure 3.6). In the outdoor settings, the vector fields point to the positions of the apparent light sources, as can be seen in the middle and lower plots of Figure 3.6. However, the positions of the apparent light sources in the outdoor environments do not coincide with the azimuth of the celestial sphere as in the indoor setting. As a consequence, the insect would rotate according to the ocellar outputs such that its body posture would be tilted and would not be parallel to the ground plane. However, this tilted attitude can be adjusted, by adding an offset to the ocellar outputs, so that the z -axes of the insect’s body and the fixed frames are realigned. This would be possible if other sensory systems, such as the compound eyes or the gravity detecting apparatus described in [44], which can provide the correct information about the ground azimuthal axis are involved. After the ocelli system is properly biased, it would still be able to respond to sudden changes in the body orientation due to external disturbances.

Another way to evaluate the ocelli performance under non-ideal conditions is to introduce random noise to the light intensity function $I(\theta) = \cos\theta$. As can be seen from the upper plot of Figure 3.7, the mosaic-like distribution differs from those in the real world environments presented in Figure 3.3 in the sense that the light intensity in a “spot” is rather uncorrelated with the light intensity in the neighboring spots. This kind of light distribution may correspond to the situation in which the insect navigates in the forest

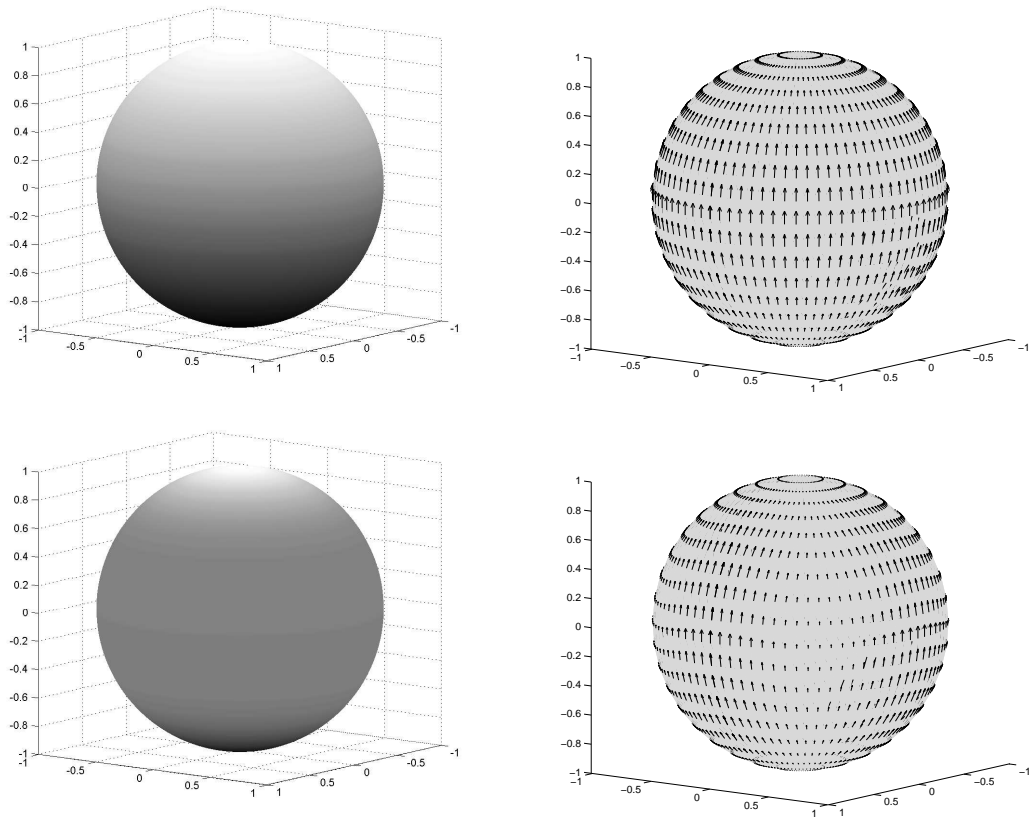


Figure 3.5: Light intensity distributions and the corresponding force fields relative to the insect's body frame induced by the ocellar outputs. The force field is uniform for the light intensity function $I(\theta) = \cos \theta$ (*upper plots*). However, the magnitude and direction of the vectors vary for the light intensity function $I(\theta) = \cos^5 \theta$ (*lower plots*).

where the light from the sky is scattered by the branches and leaves. In this case, the force field induced by the ocellar outputs converges to a larger region of the celestial sphere, rather than to a small brightest spot, as indicated by the circle in the lower right plot of Figure 3.7, with the region of convergence being dependent on the level of noisiness. Despite their inability to stabilize the insect toward a certain orientation, the ocelli can still unambiguously distinguish the ground from the sky and turn the insect to a right-side up attitude due to their wide receptive fields and high sensitivity to small variation in light intensity.

From the above simulation results, it can be seen that the orientation estimation strategy using an ocelli system is consistent with the observations on real insects that the ocelli serve as a rough and ready complement to the fine control provided by a global frame

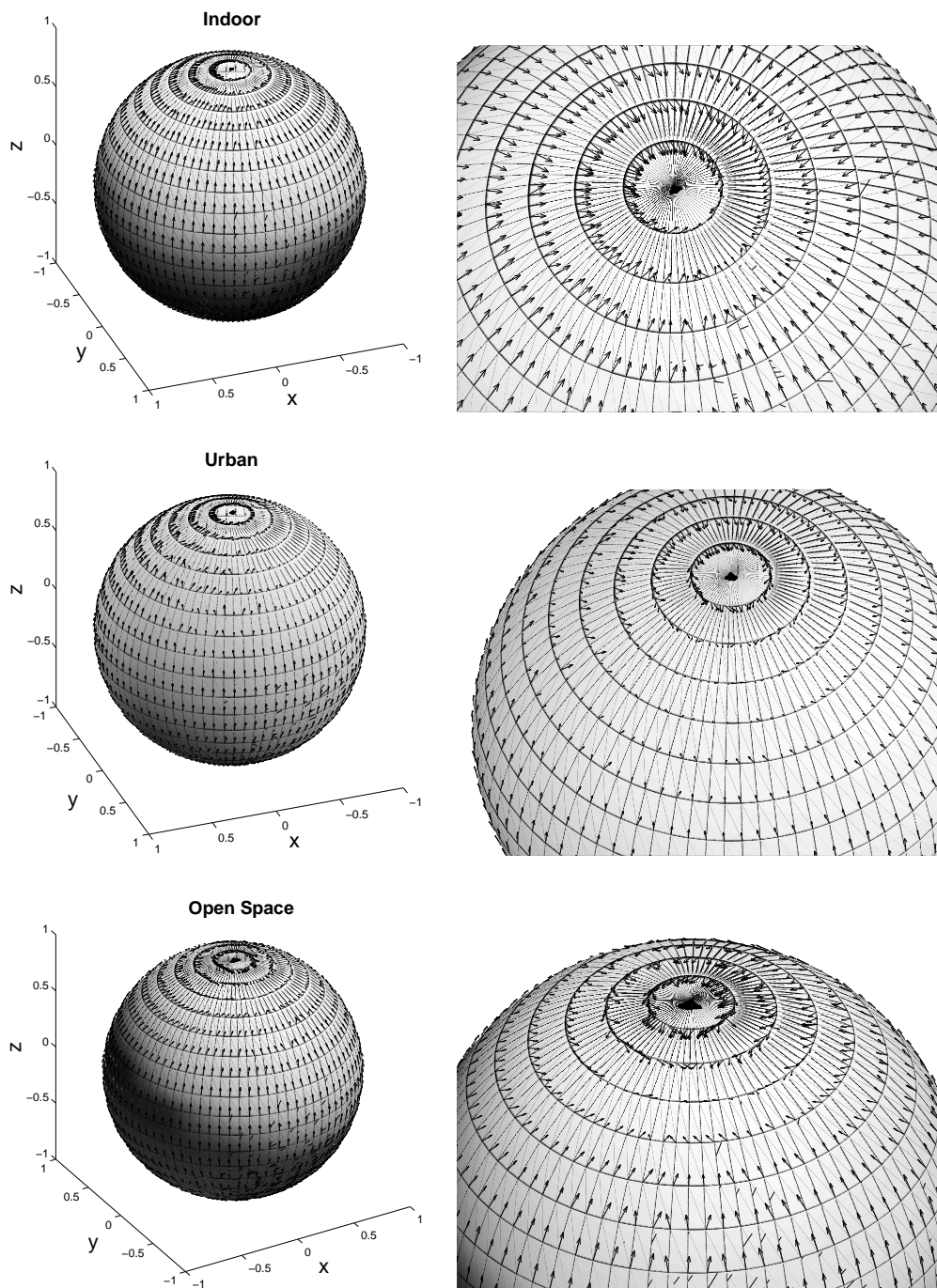


Figure 3.6: Induced force fields for different light intensity distributions: indoor environment (*top*), urban environment (*middle*), and open space environment (*bottom*). The plots on the right hand column show the close-up view around the brightest region in each case. The light intensity distributions in these real world environments are the same as those shown in Figure 3.3.

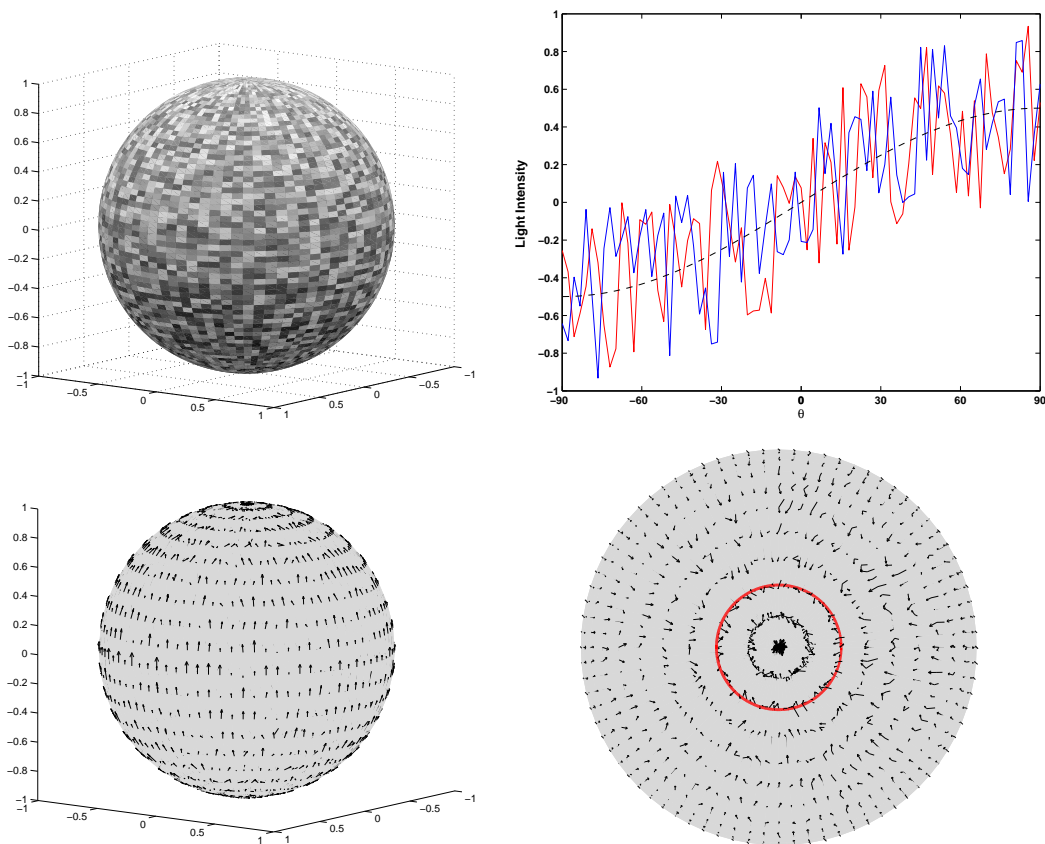


Figure 3.7: Light intensity $I(\theta) = \cos \theta$ with random noise at $\text{SNR} = 0 \text{ dB}$ (*upper left*), and the light intensity profiles at adjacent longitudes (*upper right*). The dashed line in the plot represents the noiseless intensity profile. The induced force field under the noisy condition (*lower left*), and a close-up view of the field from the north pole (*lower right*). The circle represents the region of convergence in which vectors inside this circle essentially point to random directions.

reference system, as described in Section 3.1. To this end, a simple imaging system or an electromechanical gravity sensor should be sufficient to provide the corrective signal for the ocelli system in order to achieve adequate attitude stabilization, and hence allowing the insect to adapt to a variety of heterogenous, time-varying environments while maintaining high responsiveness to quick external disturbances.

In addition to the orientation stabilization, the ocelli system may also contribute to the control of the phototactic reaction in insects. Kastberger and Schuhmann [46] observed that when flying through a tunnel, fully sighted honeybees exhibit positive phototactic reactivity toward stationary side-light illumination, while ocelli-occluded bees are photo-

tactically negative. In the simulation, the ocelli system is used to reproduce the observed phototactic behavior in insects. Figure 3.8 shows the response of an ocelli sensor to two stationary light sources of different brightness positioned above the $x - y$ plane. When the sensor is far away from the light sources, all the photoreceptors receive little light and the ocelli produce very weak response. However, as the sensor moves within a certain region around the light sources, the photoreceptors will be unequally illuminated and hence the ocelli produce strong outputs. The difference in the illumination of the photoreceptors becomes zero only when the sensor is directly underneath the brightest spot. As a result, the ocellar outputs y_1^o and y_2^o can be used as an indication of the direction of the light sources relative to the insect's position, a scheme similar to the one used in the orientation estimation. Clearly, the ocelli sensor will track the brighter light source in a neighborhood, and hence manifesting the phototactic behavior in real insects. Figure 3.9 shows snapshots of a flying insect seeking the light source using the ocelli sensor. The flight trajectory is generated by the VIFS.

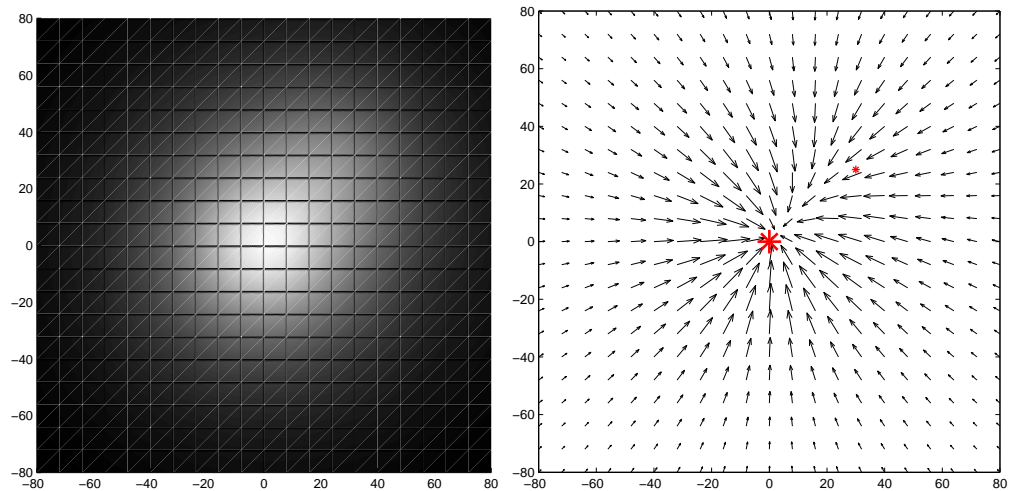


Figure 3.8: The response of an ocelli sensor to multiple light sources. The sensor produces only weak output when it is far away from the light sources. However, when the sensor is in the neighborhood of the light sources, it produces strong response due to the unequal illumination of the photoreceptors. Therefore, the insect would be attracted toward the bright region according to the ocellar outputs. The left plot shows the light distribution generated by two light sources. The asterisks in the right plot indicate the positions and relative brightness (3:1) of these two light sources.

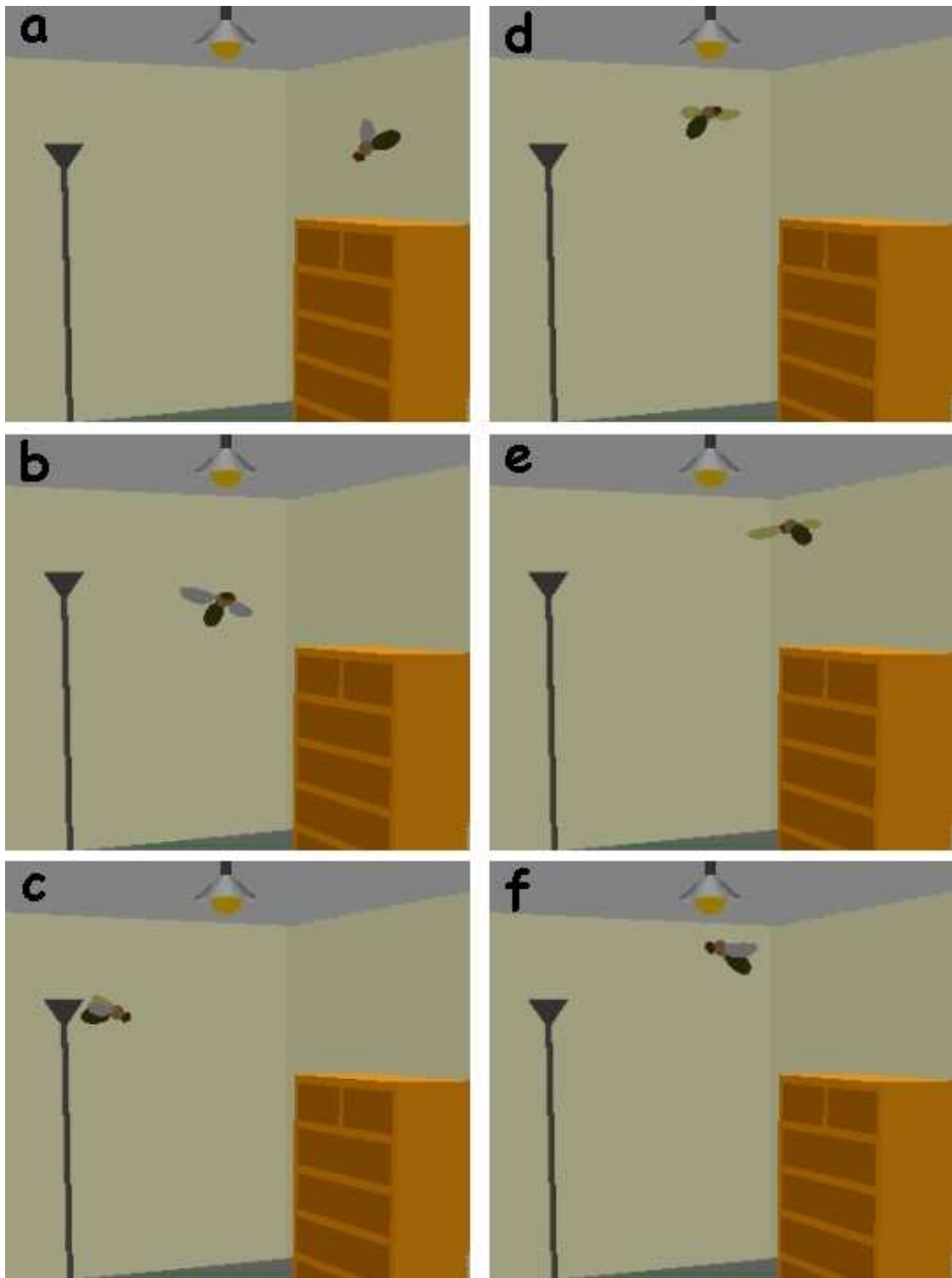


Figure 3.9: Snapshots of an insect being attracted toward the light source according to the output from the ocelli sensor. The trajectory of the insect is generated by the VIFS.

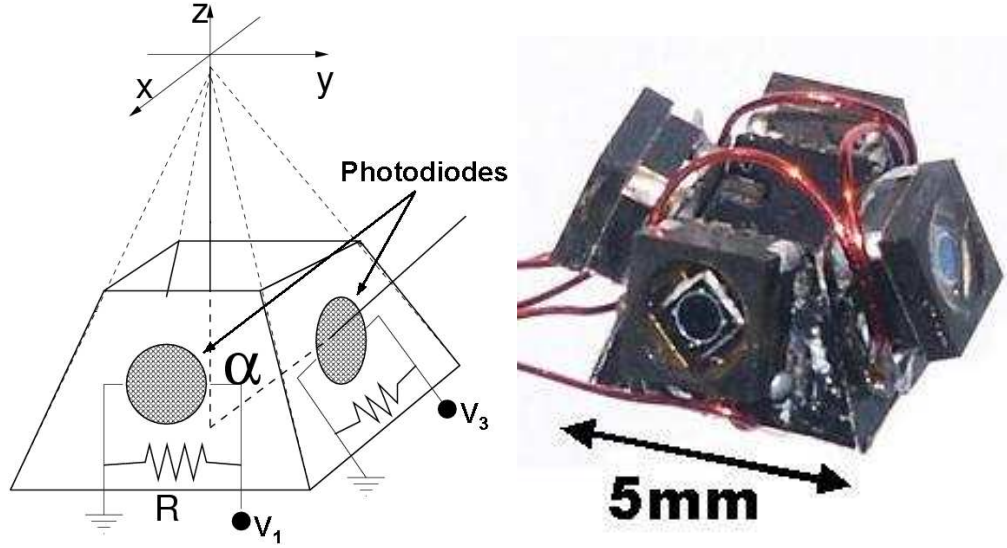


Figure 3.10: Schematic of the ocelli system design (*left*). Each face of the pyramidal structure contains one photodiode. The output voltages from these photodiodes are subtracted pairwise to give the two ocellar outputs. Photo of a prototype ocelli (*right*).

3.3 Ocelli System Design

Based on the mathematical modeling presented in the previous section, prototypes of the biomimetic ocelli system have been constructed. These devices use off-the-shelf IR photodiodes with peak sensitivity at light wavelength of 880 nm , a conic field of view of 60° , and 0.75 mm^2 active area. The photodiode is soldered onto a millimeter-scale circuit board which is created by laser micromachining $5\text{ }\mu\text{m}$ thick copper traces onto an electrically insulated trapezoidal carbon fiber layer. Four of these trapezoidal layers are joined together to form a square pyramid as shown in Figure 3.10, and several pyramidal structures with different angle α 's are made. Each photodiode collects light radiation, which induces electric current that is proportional to the intensity of light collected and the active area of the photodiode. Each photodiode is placed in parallel with a small resistor and the voltage drop across the resistor is measured. The output voltages from the four photodiodes are combined differentially to give the two ocellar outputs:

$$y_1^o = V_1 - V_2$$

$$y_2^o = V_3 - V_4$$

In order to test the sensitivity and output range of the prototype ocelli, the devices are allowed to move in a $6 \times 8\text{ cm}$ region centered at the origin $O = [0, 0, 0]^T$. An IR lamp is

positioned at $P_{source} = [0, 0, z]^T$, where $z \approx 10 \text{ cm}$ is the height from the plane of the ocelli structure to the light source. The orientation of the pyramid is kept constant such that photodiodes 1 and 2 are parallel to the x -axis, while photodiodes 3 and 4 are parallel to the y -axis. Then, the ocelli structure is moved to different $x - y$ positions and the recorded output signals are shown in Figure 3.11. The ocellar outputs give an excellent estimate of the distance from the ocelli structure to the origin. Among the structures tested, the pyramid with angle $\alpha = 40^\circ$ shows the best performance in terms of range and linearity with distance for this particular model of photodiodes. In addition, the measurements did not use any kind of noise filtering and the results were repeatable. The size of the whole structure shown on the right in Figure 3.10 is about $5 \times 5 \times 5 \text{ mm}$. However, this size can be further reduced if bare photodiodes are used.

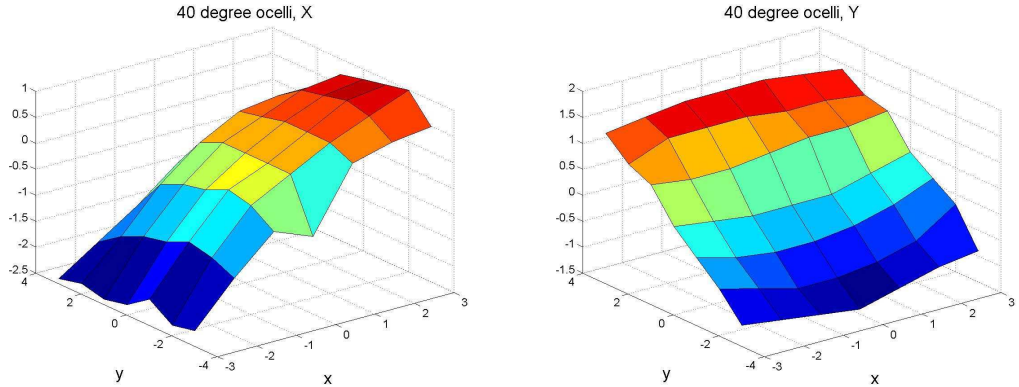


Figure 3.11: Sensitivity of the ocelli system. The ocelli sensor is allowed to move in a $6 \times 8 \text{ cm}$ region centered at the origin. The y_1^o (left) and y_2^o (right) measurements of the ocelli structure with $\alpha = 40^\circ$.

The left panel of Figure 3.12 shows a customized photodiode containing two separate receptive areas of sizes $250 \times 250 \mu\text{m}$ and $750 \times 750 \mu\text{m}$. The right panel of Figure 3.12 shows an ocelli structure using these photodiodes. The setup to test this miniaturized ocelli is illustrated on the left in Figure 3.13. The ocelli sensor is rotated around one axis under a light source and because the two axes of sensing in this structure are decoupled, the results can be extrapolated to the two axes. The individual photodiode signals are recorded as a function of the rotation angle and these pairwise signals are subtracted to give the output in one dimension. The results can be seen on the right in Figure 3.13. The ocellar output exhibits a monotonic correlation with the rotation angle, and hence it allows the

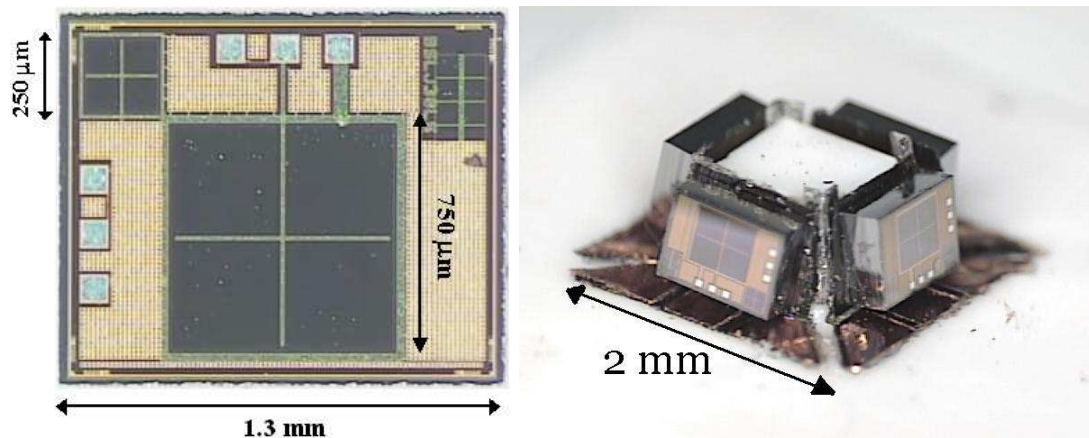


Figure 3.12: Customized photodiode containing two receptive areas of different sizes (*left*). The desired signals of either regions can be obtained directly from the corresponding built-in resistors. The miniaturized ocelli structure using the customized photodiodes (*right*).

estimation of the sensor’s orientation with respect to the light source. Moreover, the light intensity distributions in the real world environments shown in Figure 3.3 are measured using the $250 \times 250 \mu m$ portion of this customized photodiode, suggesting that micro-scale ocelli should be able to perform reliably under real world conditions.

3.4 Magnetic Field Sensor

Although the ocelli system provides a means to reorient the insect body toward a specific orientation, the insect’s heading remains arbitrary. Since maintaining the heading is fundamental for forward flight and maneuvering, it is necessary to implement a sensory system for the insect to reference the direction of its flight. While optic flow sensors can help the insect keep a straight course by compensating for undesired deviations during flight via the optomotor response, they can not “look for” a specific direction in which the insect is flying. In addition, the performance of optic flow sensors may decrease considerably in dimly lit and featureless environments. Animals may need to depend upon other sensory modalities, such as a magnetic compass, to infer their heading direction. For example, it is well established that migratory animals including birds, sea turtles, salmon, and whales rely on the magnetoreception to aid in navigation during their seasonal migration. It has been shown that honeybees also possess a magnetic organelle that can sense geomagnetic field [47]. Recent studies on insect behaviors are indicating that some insects use their

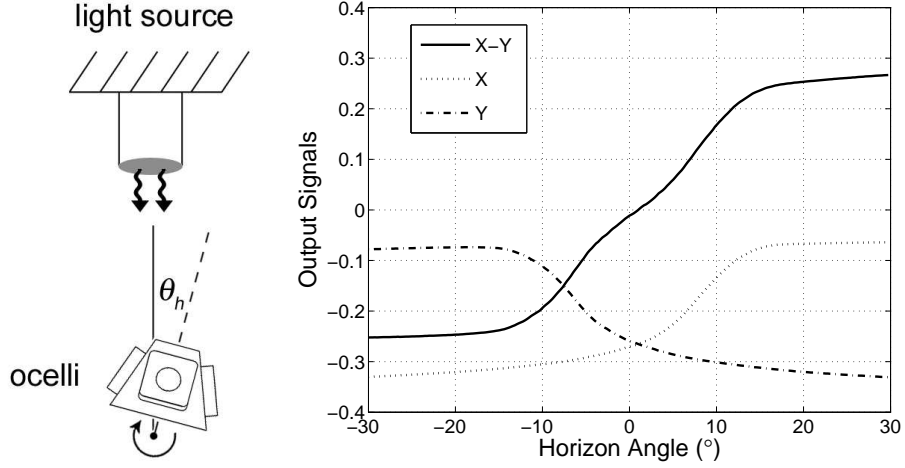


Figure 3.13: (*Left*) The setup for ocelli verification. Courtesy of R.J. Wood. The ocelli structure is rotated around one axis only and the signals from the pairwise photodiodes are recorded. (*Right*) The individual photodiode signals (broken lines) and the resulting ocellar output (solid line) in one dimension.

magnetic sense to inform them of their heading direction and help them navigate long distances [4, 97]. Following this concept, a magnetic field sensory system is proposed for the insect to reference directional information. It should be mentioned, however, that little is known about the methods in which animals detect magnetic fields. Therefore, the magnetic sensing mechanism presented in this section does not draw any analogy from a biological counterpart.

The magnetic field sensor estimates the heading of the insect based on the terrestrial geomagnetic field. The sensor consists of a U-shaped suspended structure (see the left panel of Figure 3.14), similar to the one proposed in [8]. Electric current flows through this structure, interacting with the terrestrial geomagnetic field, and induces the Lorentz force which is given by:

$$\mathbf{F}_{Lorentz} = L_o \mathbf{i} \times \mathbf{B}$$

where $\mathbf{F}_{Lorentz}$ is the force exerted at the free end of the cantilever, L_o is the length of the outer segment of the loop, \mathbf{i} is the electric current, and \mathbf{B} is the terrestrial geomagnetic field. The deflection of the cantilever, which is proportional to the force perpendicular to the cantilever, is sensed at the base by strain gauges:

$$F_{beam} = \mathbf{F}_{Lorentz} \cdot \mathbf{n}$$

where \mathbf{n} is the sensing direction of the strain gauge. Therefore, the outputs from these

strain gauges can be used to estimate the heading of the insect relative to the geomagnetic field and it is given by:

$$y^c = k_c F_{beam} = k_c L_o (\mathbf{i} \times \mathbf{B}) \cdot \mathbf{n} = k_c L_o f(R)$$

where k_c is a constant that depends on the size of the cantilever structure and the strain gauges used and $f(R)$ is a linear function of the body rotation matrix R and can be computed easily once the orientation of the electric current vector \mathbf{i}^b , the sensing direction of the strain gauges \mathbf{n}^b with respect to the insect's body frame, and the orientation of the Earth's geomagnetic field \mathbf{B}^a relative to the fixed frame are known.

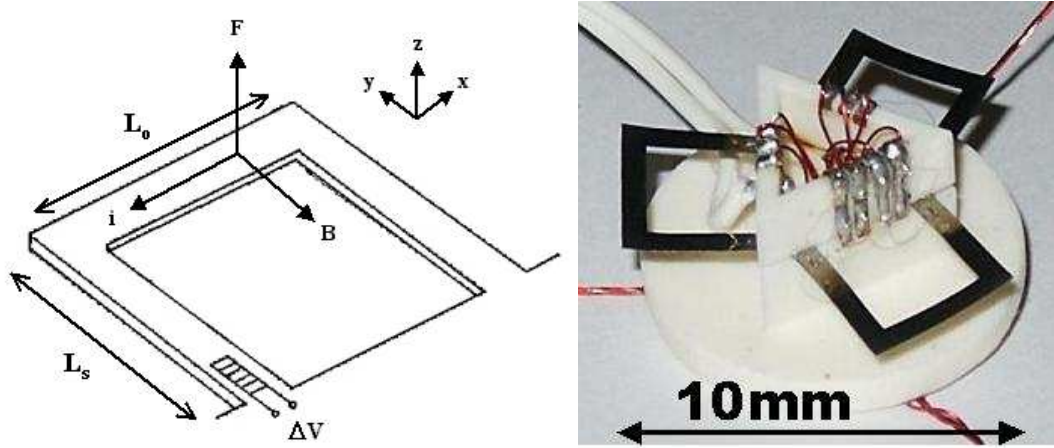


Figure 3.14: Schematic of the magnetic field sensor design (*left*). Photo of the prototype magnetic field sensor with three metal loops (*right*).

Considering the stringent requirements imposed by a micro robotic insect, design specifications are set forth for the magnetic field sensor. It needs to have a small size, a resolution $-1^\circ < \delta\gamma < 1^\circ$ for $-60^\circ < \gamma < 60^\circ$, a bandwidth exceeding 500 Hz , and power consumption less than 1 mW . First, the resolution relates to the geometric design variables of the sensor as follows:

$$\begin{aligned} iL_o B \sin \gamma &= \frac{EI\epsilon}{zL_s} \\ iL_o B \sin \gamma &= \frac{E2wh^2\epsilon}{6L_s} \end{aligned} \quad (3.15)$$

where E is the Young's modulus of the material used, L_s is the length of the side segment of the loop, $I = wh^3/12$ is the cross sectional moment of inertia, $z = h/2$ is the distance from the neutral axis to the strain gauge, w is the width, h is the thickness of the cantilever beam,

and ϵ is the strain in the beam. There is a factor of two for the width in Equation (3.15) because there are two cantilevers in parallel in the structure. Using the approximation $\sin \delta\gamma \approx \delta\gamma$ for small $\delta\gamma$ and converting from radian to degree, the sensitivity of the sensor follows from Equation (3.15) and it is given by:

$$\delta\gamma = \frac{180Ewh^2\epsilon_{min}}{3\pi iBL_oL_s} \quad (3.16)$$

where ϵ_{min} is the minimum sensitivity of the strain gauge used. Next, the bandwidth of the sensor is given by:

$$\text{Bandwidth} = \frac{1}{2\pi} \sqrt{\frac{2k}{m_{eff}}} = \frac{1}{2\pi} \sqrt{\frac{Ewh^3}{2L_s^3m_{eff}}} \quad (3.17)$$

where k is the stiffness (again there are two cantilevers in parallel) and m_{eff} is the effective mass of the loop, which can be calculated as follows [70]:

$$m_{eff} = m_o + 2 \cdot \frac{m_s}{4}$$

where m_o is the mass of the outer segment and m_s is the mass of the side segment of the loop. Thus, Equation (3.17) can be written as:

$$\text{Bandwidth} = \frac{h}{2\pi} \sqrt{\frac{E}{2\rho L_s^3(L_o + \frac{L_s}{2})}} \quad (3.18)$$

where ρ is the density of the material. Finally, the power consumption of the sensor is given by:

$$\text{Power} = Ri^2 = 3 \cdot \frac{\varrho i^2 (L_o + 2L_s)}{wh} \quad (3.19)$$

where ϱ is the resistivity of the material.

Since there are several performance metrics that can be considered in Equations (3.16), (3.18), and (3.19), the sensitivity of the sensor is chosen to be optimized while satisfying the constraints on size, power consumption, and bandwidth. Moreover, electric current and cantilever thickness are fixed, while cantilever width and length are the design variables. Table 3.1 summarizes the fixed parameters, the optimal width and length of the cantilever, and the achieved performance in terms of resolution, power consumption, and bandwidth. These design specifications show feasibility because they can satisfy the stringent requirements imposed by micro robotic insects, while provide a simple way to estimate the heading of these devices. The right panel of Figure 3.14 shows a prototype of the magnetic field sensor. The three metal sections of this sensor are $12.5 \mu\text{m}$ stainless steel

which are laser micromachined into the desired shape. The surface of the stainless steel is coated with a thin insulating layer, and semiconductor strain gauges are fixed to the base of the three sections using an automated micro-assembly stage [74, 102].

Parameter	Value	Unit
B	50	μT
ρ	9,000	kg/m^3
ϱ	$1.7 \cdot 10^{-8}$	$\Omega \cdot m$
E	120	GPa
ϵ_{min}	10^{-8}	
i	100	mA
h	12.5	μm
L_o	4	mm
L_s	3	mm
w	25	μm
$\delta\gamma$	± 1.5	deg
Bandwidth	422	Hz
Power	0.02^1	mW

1. Not including the power used by strain gauge sampling.

Table 3.1: Design specifications of a magnetic field sensor using copper as the material. Fixed parameters are on top and optimized variables are at bottom.

3.5 Chapter Summary and Discussion

In this chapter, sensory systems that are used to estimate the orientation of the insect are modeled and their prototypes have been constructed and tested. The ocelli sensor, inspired by the ocelli of real insects, comprises of four photodiodes arranged symmetrically in the dorsal portion of the insect's head such that each photodiode collects light from a different region of the surrounding. The measurements from these photodiodes are compared pairwise so that the sensor can estimate the roll and pitch angles of the ocelli reference frame relative to a fixed frame. It has been shown that if the light intensity in the surrounding

is monotonically decreasing away from the generating source, the ocelli sensor can stabilize the attitude of the insect with respect to that light source. Although the light intensity distributions in real world environments do not appear monotonic and can be noisy to some extent, the simulation using experimental data suggests that the ocelli sensor can still reorient the insect body toward the brightest spot under non-ideal conditions. However, the ocelli sensor alone can not achieve adequate attitude stabilization when the light source is not at the zenith. Signals from other sensory organs, such as compound eyes and gravity detecting ciliary cells, are necessary to offset the biasing effect of the tilted light source position.

It is worth mentioning that some horizon sensors for attitude stabilization are commercially available. The FMA Co-Pilot ¹ and the Futaba PA-2 ² for radio-controlled aircraft are based on four optical sensors on two-axis planar configuration that detect the difference in infrared signature between the ground and the carbon dioxide in the atmosphere to provide day or night roll-pitch stabilization. Despite the fact that the designs of these devices are not available to the public, they can be compared to the ocelli sensor as they also rely on the differential measurements of a monotonic function of the vertical latitude. Therefore, they should fall within the mathematical modeling of ocelli developed in this chapter. Another type of horizon sensor based on the dragonfly ocelli has been developed independently by Chahl *et al.* [13] for Mars exploration applications. This system contains two sets (UV/green) of four photodiodes which allow the spectral opponent processing of UV and green radiation to eliminate false attitude signals caused by the sun when it is near the horizon. While these horizon sensors perform well in open space environments, they do not work indoors and their mechanisms may become unreliable in urban or shady environments where large parts of the horizon or sky are obscured.

In addition to the ocelli system, a magnetic field sensor is modeled for the insect to reference the heading direction. This sensor consists of three U-shaped cantilever beams which conduct electric current. The interaction between the external magnetic field and these current loops induces the Lorentz force that deflects the beams. Semiconductor strain gauges are placed at the base of the cantilever to detect such deflections and hence inferring the change in the direction of the sensor relative to the magnetic field. Although insects have been shown to possess magnetic sense, the mechanisms by which they detect the magnetic field are not known. Therefore, the magnetic sensing strategy developed in this

¹FMA Direct, <http://www.fnadirect.com/>

²Futaba, <http://www.futaba-rc.com/>

chapter is mainly an engineering approach and may not be very efficient, which is a major characteristic of biological systems. Interestingly, insects are able to infer their heading via another sense. The dorsally directed regions of the compound eyes of many insects are equipped with specialized photoreceptors that are sensitive to the polarized light pattern generated as sunlight scatters through the atmosphere [106, 108]. These photoreceptors feed into polarization-sensitive interneurons that function as “celestial compasses,” which can inform the insect about the direction in which it is travelling [51]. Nonetheless, navigation based on polarized light pattern is not possible when the sky is not visible to the insect (e.g., flying in a cave or crawling under ground). In these cases, possessing magnetic sense may be advantageous for the insect to reference directional information.

Chapter 4

Angular Rate Sensors

In addition to the photoreceptor-based sense organs, flying insects possess numerous mechanoreceptor-based sense organs that are important for flight stabilization. These organs contain arrays of tiny, hair-like sensors (e.g., cilia and sensilla) that are distributed on the head, neck, appendages, and other surfaces of the body. When deformed, these sensors trigger neural impulses. By pooling the signals from a group of these sensors in a region, local force/pressure applied to that part of the body can be measured. Examples of such mechanosensory systems include gravity detecting ciliary cells, air current sensitive hairs, wing force sensors, and inertial force sensors.

Flying insects of order Diptera possess a pair of unique mechanoreceptor-based sense organs, called halteres, that can detect body rotational velocities via gyroscopic forces [39]. The halteres of dipterous insects are derived through evolutionary transformation of the hind wings and they no longer serve any aerodynamic function. They are situated in the space between the thorax and abdomen so that air current has negligible effect on them during flight. Free flight of the insect seems to be controlled by a combination of visual and vestibular sensor organs. The haltere afferents have been shown to mediate compensatory flight control reflexes through their connections with thoracic motor neurons innervating control muscles of the wings and neck in *Drosophila* [20] and *Calliphora* [27, 62, 64]. Motor neurons of the haltere muscles also receive excitatory input from directionally sensitive visual interneurons, and subsequently altering the haltere kinematics [15]. These findings suggest that visual input can influence the activity of wing steering muscles. The effect, however, takes place via the haltere-mediated equilibrium reflexes.

Although the vast majority of insects can fly quite well without halteres, the

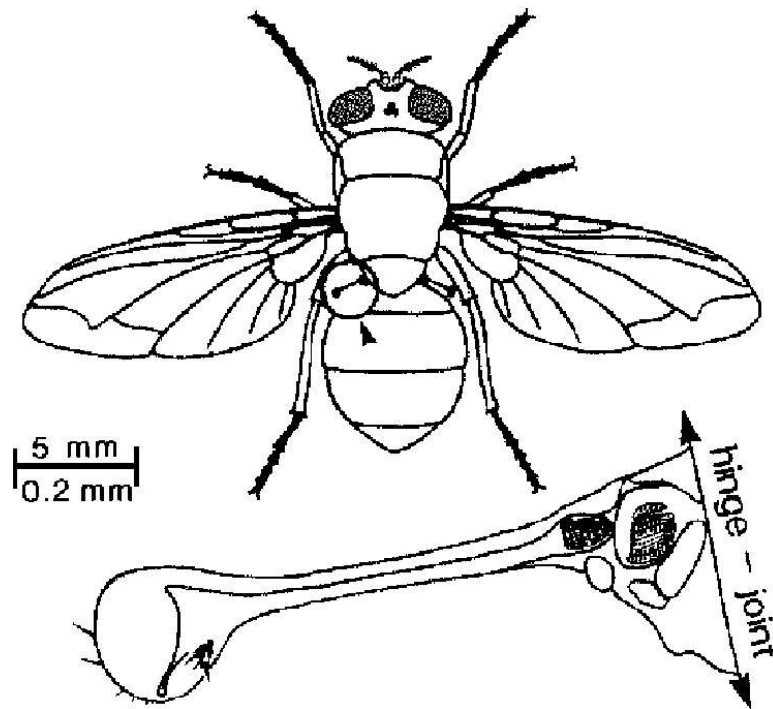


Figure 4.1: Halteres of the blowfly *Calliphora*. There are about 335 campaniform sensilla embedded in the haltere joint to detect the Coriolis force exerted on the haltere. During flight the halteres beat up and down through an angle of approximately 180° anti-phase to the wings at the wingbeat frequency. Adapted from [62].

maneuverability of dipterous insects rests in large part on the integration of information from visual and mechanosensory systems. Signals from the halteres supplement those provided by the compound eyes, as the rotational frequency bandpass characteristics of each ensure that no matter how slowly or quickly the insect rotates, at least one of these two systems will be sensitive to the rotation [81, 82]. The halteres are most sensitive to fast rotations while the visual system responds better to slower rotations. However, halteres carry the advantage of being able to provide stabilizing signals in the absence of visual feedback. In addition, halteres react to body rotations much faster than does the visual system. The latencies are 5-10 *ms* for haltere-mediated reactions compared to at least 30 *ms* for visual reactions [40]. As a consequence, haltere system alone may be sufficient to mediate quick reactions which bring the insect into its working range without inputs from other sensory systems.

4.1 Haltere Morphology

Figure 4.1 illustrates the halteres of the blowfly *Calliphora*. The halteres resemble small balls at the end of thin rods. During flight the halteres beat up and down through an angle of nearly 180° anti-phase to the wings at the wingbeat frequency. There are about 335 campaniform sensilla organized in five distinct fields at the haltere base. These mechanoreceptors are embedded in the flexible exoskeleton, and function as strain gauges to detect the strains generated as the Coriolis forces cause the haltere to deviate from its stroke plane [29, 69]. When a fly's halteres are removed or immobilized, it can not maintain stable flight and quickly falls to the ground. In addition, the two halteres of a fly are non-coplanar (each is tilted backward from the body's transverse plane by about 30°). This non-coplanarity of the two halteres is essential for a fly to detect rotations about all three (the roll, pitch, and yaw) turning axes [63]. Although a fly with one haltere removed can fly almost normally, it is unable to detect rotations about an axis perpendicular to the stroke plane of the remaining haltere [62].

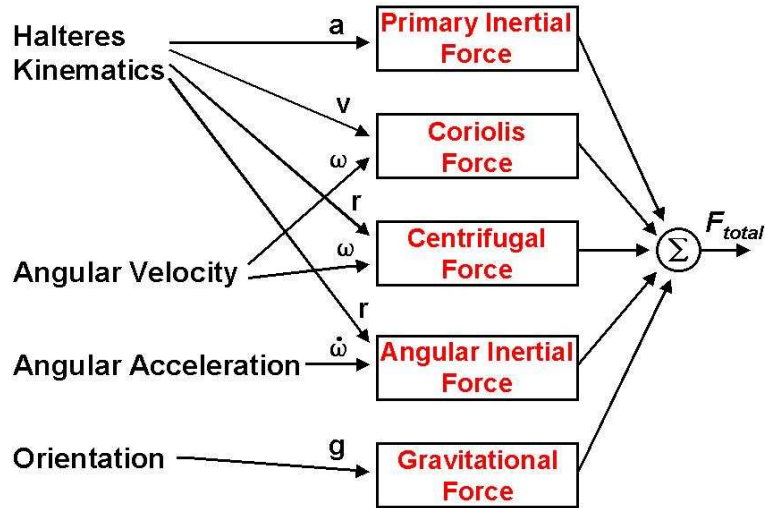


Figure 4.2: Components of the force acting on the haltere during flight.

A complex force, as a result of insect motion and haltere kinematics, acts on the halteres during flight [62] (see Figure 4.2). Assuming no translational motion of the insect, this force can be expressed in vector notation by the following:

$$\mathbf{F}_{haltere} = m\mathbf{g} - m\mathbf{a} - m\dot{\boldsymbol{\omega}} \times \mathbf{r} - m\boldsymbol{\omega} \times (\boldsymbol{\omega} \times \mathbf{r}) - 2m\boldsymbol{\omega} \times \mathbf{v} \quad (4.1)$$

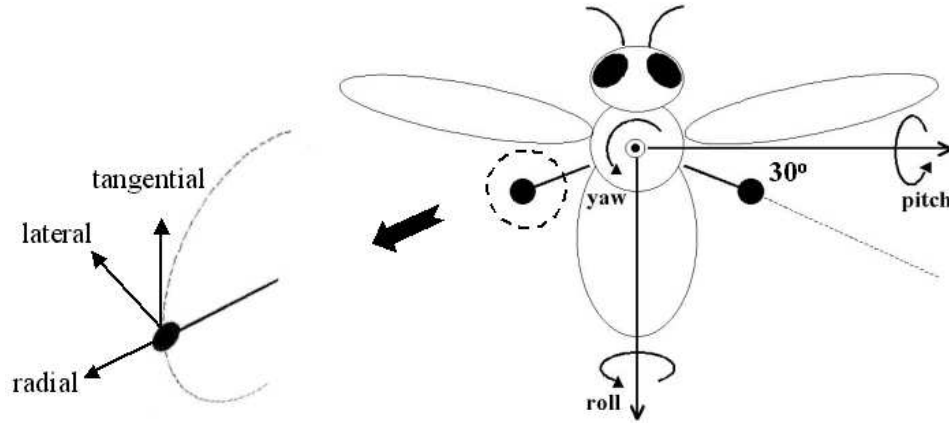


Figure 4.3: The roll, pitch, and yaw axes of the fly. The force acting on the haltere can be decomposed into three components: the lateral force is orthogonal to the haltere stroke plane, the radial force is along the longitudinal axis of the haltere, and the tangential force is in the direction of the instantaneous haltere motion.

where m is the mass of the haltere, \mathbf{r} , \mathbf{v} , and \mathbf{a} are the position, velocity, and acceleration of the haltere relative to the insect body, $\boldsymbol{\omega}$ and $\dot{\boldsymbol{\omega}}$ are the angular velocity and angular acceleration of the insect, and \mathbf{g} is the gravitational constant. In addition, an oscillating reference system is chosen for this force vector. It is described in three orthogonal components: the radial, the tangential, and the lateral components, as depicted by the exploded view of the haltere in Figure 4.3.

Insect's body rotations produce centrifugal ($-m\boldsymbol{\omega} \times (\boldsymbol{\omega} \times \mathbf{r})$) and Coriolis ($-2m\boldsymbol{\omega} \times \mathbf{v}$) forces on the halteres. The centrifugal force is generally smaller than the Coriolis force and mostly in the radial and tangential directions. Moreover, since the centrifugal force is proportional to the square of angular velocity of the insect, it provides no information on the sign of rotations. The Coriolis force, on the other hand, is proportional to the product of the angular velocity of the insect and the instantaneous haltere velocity. The Coriolis force has components in all three directions and contains information on the axis, sign, and magnitude of the insect's body rotation. The angular acceleration force ($-m\dot{\boldsymbol{\omega}} \times \mathbf{r}$) is proportional to the product of the angular acceleration of the insect and the instantaneous position of the haltere. Although the physical basis of acceleration detection was not specified, Sandeman [75] proposed that the halteres sense angular acceleration, analogous to the canal organs of vertebrates and crabs. The angular acceleration and the Coriolis force signals are distinguishable because of the 90° phase shift (they are orthogonal functions). The primary

inertial force ($-m\mathbf{a}$) depends on the haltere acceleration relative to the insect body. This force is orders of magnitude larger than the Coriolis force and has only radial and tangential components. The gravitational force ($m\mathbf{g}$) is always constant and depending on the haltere position and the insect's body orientation in space, its distribution in the three directions varies. However, the effect of this gravitational force on the angular velocity sensing is negligible because it is a tonic lateral component which can be considered as a DC offset on the Coriolis force and removed easily by the subsequent signal processing step.

4.2 Haltere Modeling

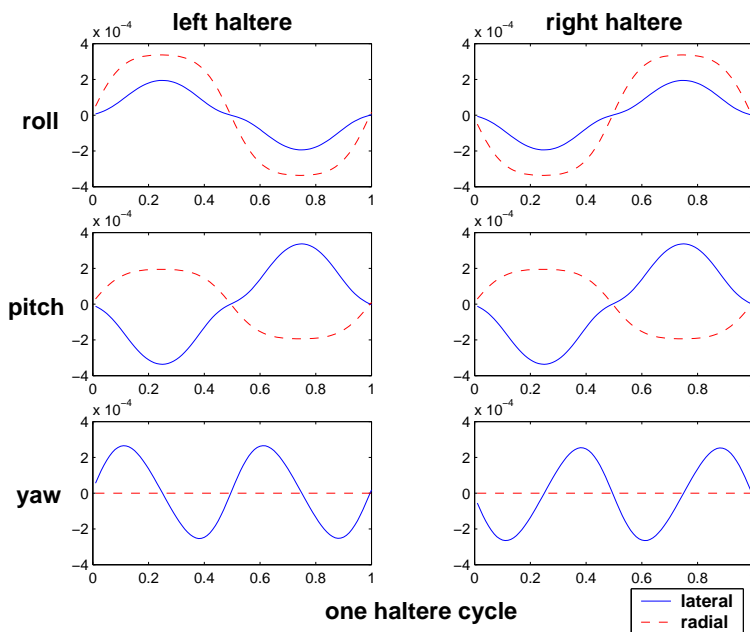


Figure 4.4: Coriolis force signals for rotations about the roll, pitch, and yaw axes.

Figure 4.4 shows the traces of the components of the Coriolis force for rotations about the roll, pitch, and yaw axes. Note that since the Coriolis force is proportional to the cross product of the insect's angular velocity and the instantaneous haltere velocity, there is no tangential component in the Coriolis force. In addition, to detect body rotations, only the lateral forces on the halteres are measured because the large primary inertial force has no contribution in the lateral direction and hence it is possible to measure the relatively strong Coriolis signal among all other interfering force signals appearing in this direction.

Because of the dependence of the Coriolis force on the haltere velocity, these force signals are modulated in time with haltere beat frequency. For a roll rotation, the signal is modulated with the haltere beat frequency and the left and right signals are 180° out-of-phase. For a pitch rotation, the signal is also modulated with the haltere beat frequency, but the left and right signals are in-phase. For a yaw rotation, the signal is modulated with double the haltere beat frequency and the left and right signals are 180° out-of-phase.

Formally, the Coriolis forces can be obtained by explicitly writing the positions and velocities of the two halteres:

$$\begin{aligned}
 \mathbf{r}_l(t) &= [\sin \varsigma \cos \beta(t) \quad -\cos \varsigma \cos \beta(t) \quad \sin \beta(t)]^T \\
 \mathbf{r}_r(t) &= [\sin \varsigma \cos \beta(t) \quad \cos \varsigma \cos \beta(t) \quad \sin \beta(t)]^T \\
 F_l(t) &= -2m\mathbf{t}_l \cdot [\boldsymbol{\omega} \times \dot{\mathbf{r}}_l(t)] \\
 F_r(t) &= -2m\mathbf{t}_r \cdot [\boldsymbol{\omega} \times \dot{\mathbf{r}}_r(t)] \\
 \beta(t) &= -\Phi \cos 2\pi\nu t
 \end{aligned}$$

where $\mathbf{r}_l(t)$ and $\mathbf{r}_r(t)$ are the position vectors of the left and right halteres, $F_l(t)$ and $F_r(t)$ are the lateral Coriolis forces measured by the left and right halteres, Φ is the stroke amplitude of the haltere, ς is the tilt angle of the halteres relative to the transverse plane, $\beta(t)$ is the angle between the haltere position vector \mathbf{r} and the roll-pitch plane of the insect, and ν is the haltere beat frequency. The unit vectors, $\mathbf{t}_l = [-\cos \varsigma, -\sin \varsigma, 0]$ and $\mathbf{t}_r = [-\cos \varsigma, \sin \varsigma, 0]$, define the positive (forward) lateral directions of the left and right halteres, respectively (see Figure 4.3). After some straightforward but tedious manipulation, the measured Coriolis forces can be written as follows:

$$\begin{aligned}
 F_l(t) &= -[2m \sin \varsigma f_1(t)]\omega_x + [2m \cos \varsigma f_1(t)]\omega_y - [2m f_2(t)]\omega_z \\
 F_r(t) &= +[2m \sin \varsigma f_1(t)]\omega_x + [2m \cos \varsigma f_1(t)]\omega_y + [2m f_2(t)]\omega_z \\
 f_1(t) &= \dot{\beta}(t) \cos \beta(t) \\
 f_2(t) &= \dot{\beta}(t) \sin \beta(t)
 \end{aligned}$$

where the modulating signals of the roll (ω_x), pitch (ω_y), and yaw (ω_z) angular velocities are highlighted in the square brackets and plotted in Figure 4.4. A careful inspection at these modulating signals reveals specific periodicity and they can be expanded in Fourier's

series as follows:

$$f_1(t) = \sum_{n=1}^{+\infty} a_n(\Phi) \sin((2n)2\pi\nu t) \quad (4.2)$$

$$f_2(t) = \sum_{n=0}^{+\infty} b_n(\Phi) \sin((2n+1)2\pi\nu t) \quad (4.3)$$

where the coefficients, $a_n(\Phi)$ and $b_n(\Phi)$, depend on the haltere stroke magnitude Φ . Note that even in the case where the haltere motion is not perfectly sinusoidal, but it is still in phase with the wingbeat frequency, that is, $\beta(t) = -\sum_{n=1}^{+\infty} c_n \cos(2\pi n\nu t)$, the Fourier expansions in Equations (4.2) and (4.3) still hold. This includes the case more commonly observed in real insects where halteres move at a roughly constant velocity during upstroke and downstroke, resulting in a triangular-shaped motion. That is, $\dot{\beta}(t) = v_{max} \text{sign}(\sin(2\pi n\nu t))$ where $\text{sign}(x) = \frac{x}{|x|}$ and v_{max} is a constant. This fact is very important since it highlights one of the robustness properties of the haltere demodulation scheme.

Utilizing the characteristics (frequency, modulation, and phase) of these force signals on the left and right halteres, a demodulation scheme is proposed to decipher roll, pitch, and yaw rotations. First, a pitch rotation can be easily distinguished from roll and yaw rotations by noting the phases of the left and right signals. Because the left and right signals are in-phase for pitch while out-of-phase for roll and yaw, adding the left and right signals retains pitch component and eliminates roll and yaw components. If the left and right signals are subtracted instead, the pitch component is eliminated. The roll angular velocity is distinguished from the yaw angular velocity by noting that the two modulating signals are orthogonal in the Fourier space. In particular, the first coefficients of the Fourier expansions $a_1(\Phi)$ and $b_0(\Phi)$ in Equations (4.2) and (4.3) can be extracted with the following demodulation:

$$\begin{aligned} \bar{h}_y(t) &= -(F_l(t) + F_r(t)) \sin(2\pi\nu t) \\ \bar{h}_x(t) &= (F_l(t) - F_r(t)) \sin(2\pi\nu t) \\ \bar{h}_z(t) &= (F_l(t) - F_r(t)) \sin(4\pi\nu t) \end{aligned}$$

From the above equations, it is clear that when the signals \bar{h}_x , \bar{h}_y , and \bar{h}_z are averaged over one haltere cycle, a sinusoidal signal at the haltere frequency retrieves the roll component which is modulated with the haltere beat frequency, while a sinusoidal signal at double the haltere frequency retrieves the yaw component which is modulated with double the haltere beat frequency. All higher frequency components are removed by

averaging the signals over one haltere cycle:

$$\begin{aligned}
 y_1^h(t) &= \int_{t-\frac{1}{\nu}}^t \bar{h}_x(\tau) d\tau = \frac{2m a_1 \sin \varsigma}{\nu} \omega_x = \frac{1}{A_r} \omega_x \\
 y_2^h(t) &= \int_{t-\frac{1}{\nu}}^t \bar{h}_y(\tau) d\tau = \frac{2m a_1 \cos \varsigma}{\nu} \omega_y = \frac{1}{A_p} \omega_y \\
 y_3^h(t) &= \int_{t-\frac{1}{\nu}}^t \bar{h}_z(\tau) d\tau = \frac{2m b_0}{\nu} \omega_z = \frac{1}{A_y} \omega_z
 \end{aligned} \tag{4.4}$$

where the constants A_r , A_p , and A_y set the gains for the amplifiers. Therefore, this technique effectively decouples a roll rotation from a yaw rotation. Figure 4.5 illustrates graphically the proposed demodulation scheme.

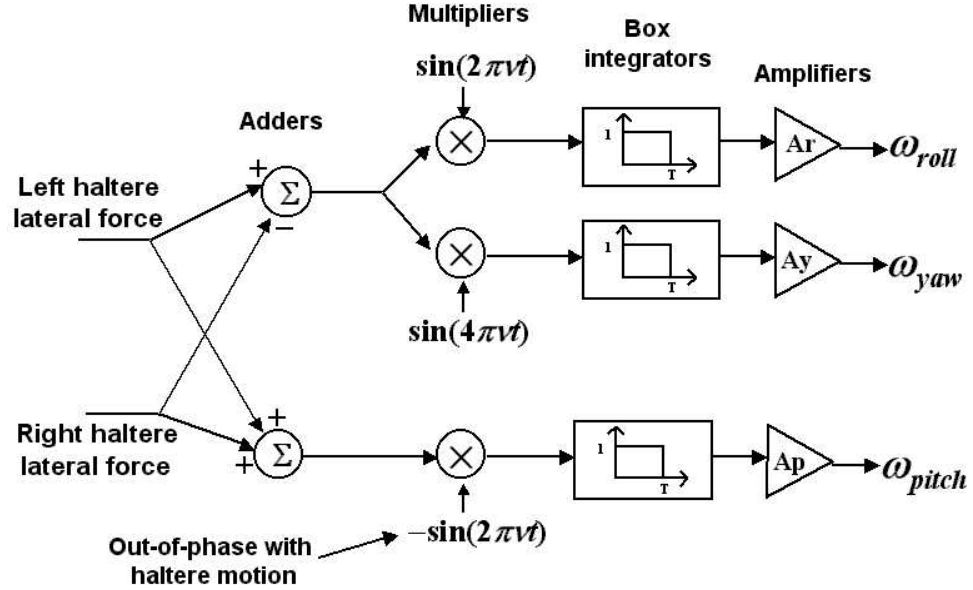


Figure 4.5: Demodulation scheme of haltere forces. The roll, pitch, and yaw angular velocities are decoupled by utilizing the phase, frequency, and modulation of the left and right Coriolis force signals. The box integrators average out the periodic disturbances caused by wing rotational motion.

4.2.1 Simulation

The mechanism by which the halteres detect angular velocities and the proposed demodulation method have been simulated for the performance of the halteres. The angular velocities of an insect under hovering mode and recovering from the upside down condition

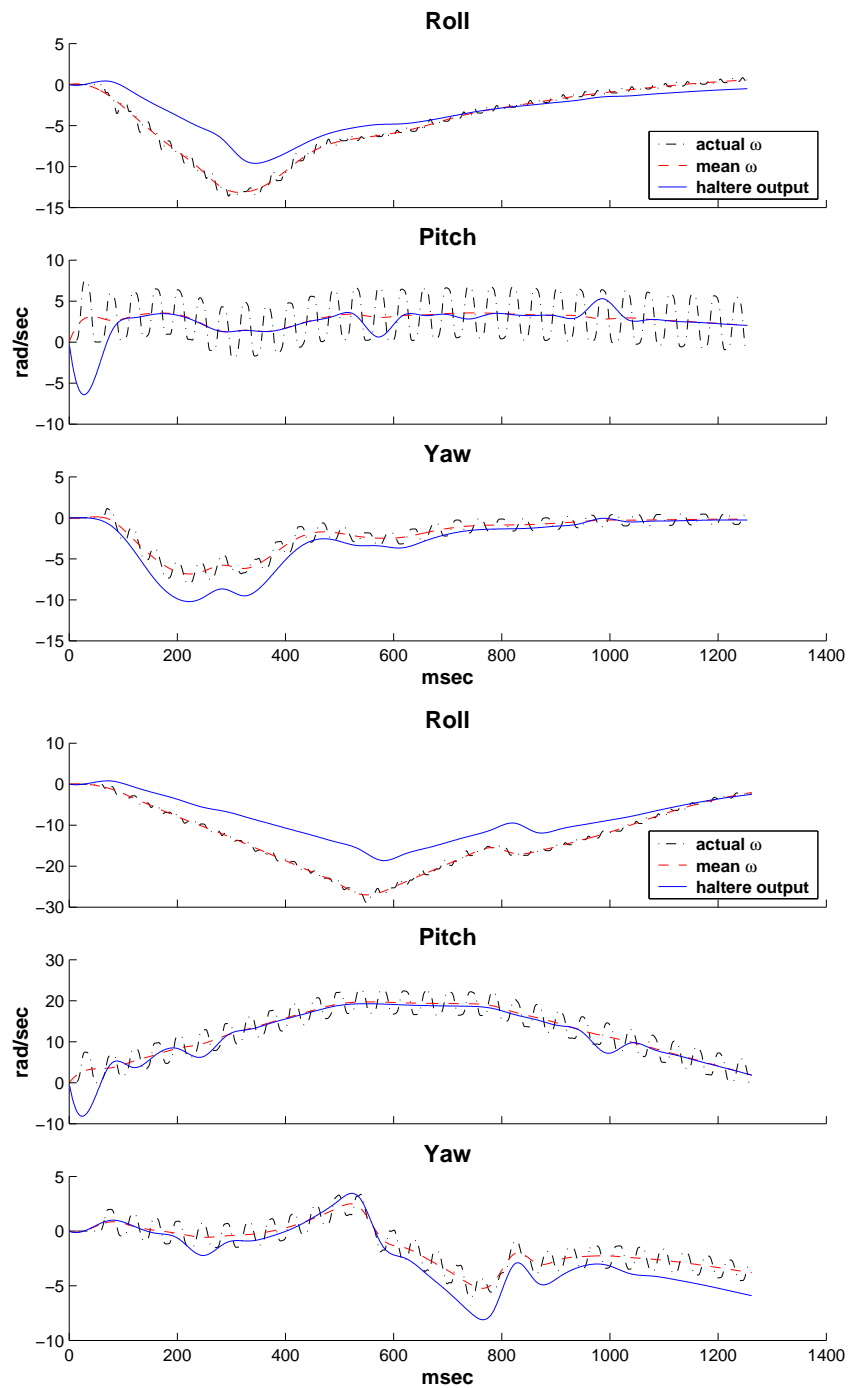


Figure 4.6: Simulation of angular velocity detection by halteres. The inset is under hovering flight mode (*top*) and recovering from the upside down orientation (*bottom*). The halteres are beating off the stroke plane of the wings and therefore the lateral directions of the halteres are not orthogonal to the wing stroke direction. It can be seen that the halteres detect false signals as a result of the common-mode body oscillations due to wing motion.

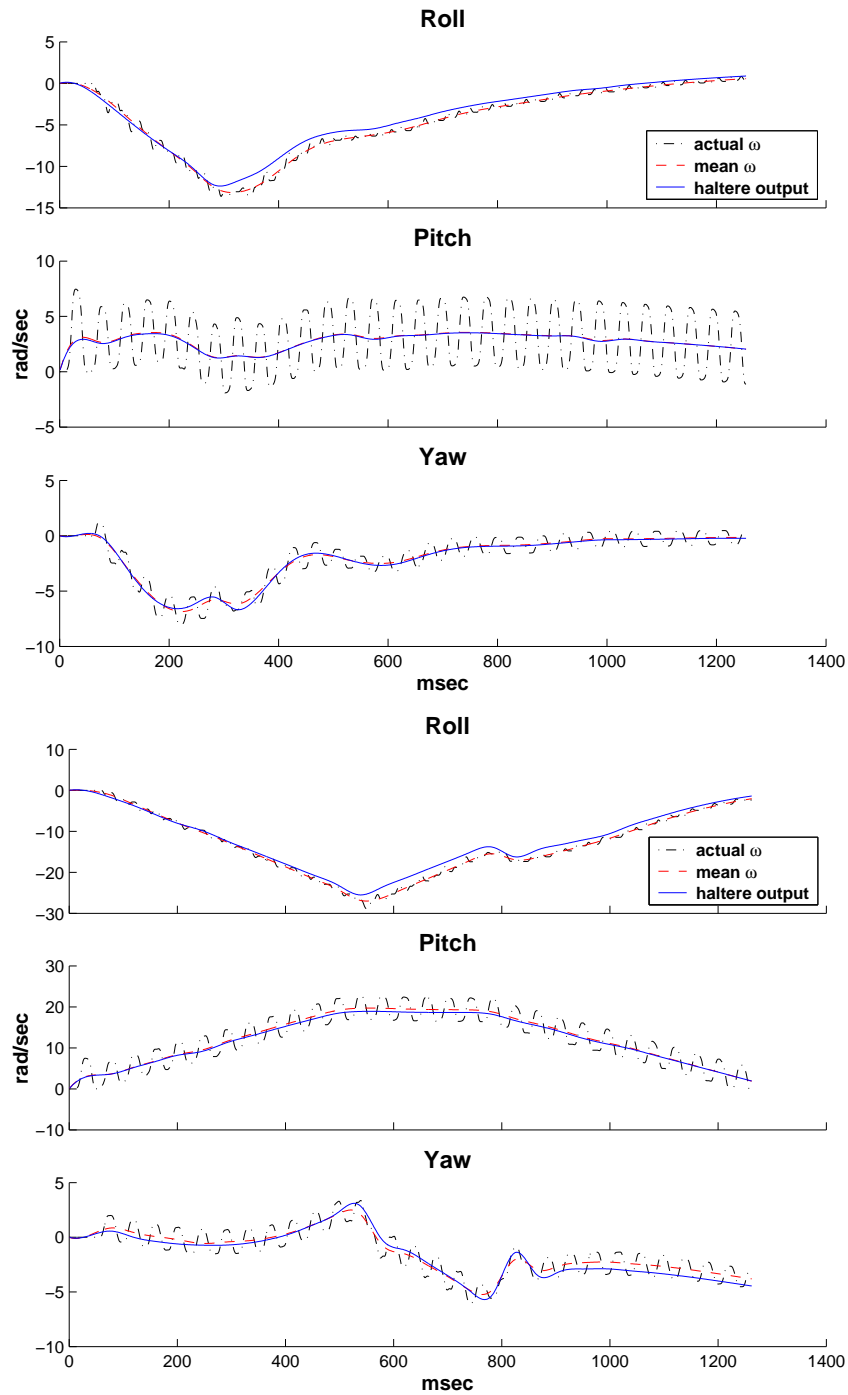


Figure 4.7: Simulation of angular velocity detection by halteres. The insect is under hovering flight mode (*top*) and recovering from the upside down orientation (*bottom*). The halteres are beating in the stroke plane of the wings and therefore the lateral directions of the halteres are orthogonal to the wing stroke direction. Compare to Figure 4.6, the common-mode error due to wing motion is greatly reduced.

are generated by the VIFS, and the results are shown in Figures 4.6 and 4.7. From the simulation, it is clear that the proposed demodulation scheme, using box integrators as low pass filters, averages out the oscillatory disturbances (the dash-dotted lines in Figures 4.6 and 4.7) due to the beating wings. From a flight control’s point of view, this is beneficial since the wingbeat kinematics of a flying insect can be controlled at most on a wingbeat-by-wingbeat basis. The halteres filter out the periodic oscillations of the angular velocity due to the wing rotational motions. Moreover, when the wings are flapping, the insect’s body would oscillate, as a result of the wing inertia, along an axis parallel to the direction of the wing stroke. If the lateral directions of the halteres are not orthogonal to the direction of this body oscillation, a false signal would be detected by the halteres. This is evidenced by the offset signals observed in Figure 4.6. However, it is possible to reduce this common-mode error by phase-locking the halteres to the wings in the stroke plane so that the body oscillations would not appear as force components in the lateral directions of the halteres. This can be seen in Figure 4.7.

4.3 Haltere System Design

The results of the simulation suggest that it is feasible to use biomimetic halteres on a robotic flying insect to measure angular velocities and prototypes of the mechanical haltere have been constructed. The key parameters for the design of the haltere system are the haltere length, mass, beat frequency, and stroke amplitude. At this stage, little attention is paid to the haltere orientation since it is assumed that the device can be arbitrarily placed upon a robotic insect.

Unlike the force sensing methods used in [1, 9, 110], the haltere must have only one sensing degree of freedom (i.e., the direction orthogonal to the haltere beating plane). The design of the haltere must allow for high stiffness in the tangential direction and compliance in the lateral direction. Therefore, the large primary inertial forces will not be sensed, and the smaller Coriolis forces can be detected. The best case mechanically for this type of structures is a flat beam with the wide face in the plane of the haltere beating. The ratio of the stiffness in the tangential and lateral directions is given by the following:

$$\frac{k_t}{k_l} = \frac{\frac{3EI_t}{l^3}}{\frac{3EI_l}{l^3}} = \frac{I_t}{I_l} = \frac{\frac{hw^3}{12}}{\frac{wh^3}{12}} = \frac{w^2}{h^2} \quad (4.5)$$

where I_t and I_l are the tangential and lateral cross sectional moments of inertia, l is the length, w is the width, and h is the thickness of the beam.

One of the major concerns with the design of the haltere is actuation. Since the Coriolis force is proportional to the haltere velocity, it is desired to have a high haltere beat frequency and a large stroke amplitude. Two methods of actuation have been tried. The simpler of the two places the haltere on a vibrating structure with a high Q compliant beam in between. The vibrating structure, in this case a piezoelectric actuator, drives the haltere into resonance, while its high Q gives large stroke amplitudes. Piezoelectric vibrating structures have been developed and have proven to be able to detect Coriolis force with high accuracy [76]. This method has the benefits of not only being simple to construct, but also this structure has the ability to be driven parasitically from the body vibrations of a robotic flying insect. The second method places the haltere on the output link of a fourbar mechanism driven by a piezoelectric actuator, similar to the method used to drive the MFI wing as described in [28, 85, 113].

4.3.1 Simple Vibrating Haltere

The first design to be discussed is the piezo-actuated vibrating haltere. The mechanical haltere measures the Coriolis force using 1 mm long \times $100\text{ }\mu\text{m}$ wide semiconductor strain gauges at its base which measure moments applied in the direction orthogonal to its beating plane. Using the haltere beat frequency of $\nu = 150\text{ Hz}$ at a stroke amplitude of $\Phi = \pi/2\text{ rad}$, and a length of $l = 5.5\text{ mm}$, the velocity of the mass is found to be 2.59 m/s . As a low-end estimate of a small angular velocity that a robotic flying insect will encounter, ω_{min} is set to 1 rad/s . Finally, the mass is set to 5 mg , so that the Coriolis force acting on the haltere at ω_{min} is roughly $25.9\text{ }\mu\text{N}$.

The haltere can be thought of as a cantilever, with one end fixed at the point of rotation. Hence, the Coriolis force acting on the mass produces a strain in the beam defined by the following:

$$F_{Coriolis} = \frac{M}{l-x} = \frac{EI\epsilon}{z(l-x)} \quad (4.6)$$

where $F_{Coriolis}$ is the Coriolis force, M is the generated moment, x is the distance from the base of the cantilever to the strain gauge, E is the Young's modulus of the haltere material, I is the cross sectional moment of inertia, z is the distance from the neutral axis to the strain gauge, and ϵ is the strain in the haltere. From Equation (4.6), it is clear that the maximum moment, and thus the maximum sensitivity will occur by placing the strain gauge as close to the point of rotation as possible. The haltere is constructed in such a way that there is a high Q compliant section to allow for rotation, and then the beam is twisted

90° to allow compliance in the lateral direction as shown in the left panel of Figure 4.8. Due to the size of the strain gauge used and the soldering process, the minimum dimension x is constrained to be 2 mm. The modulus E is given to be 193 GPa because the material used is stainless steel. The cross sectional moment of inertia is defined to be $I = wh^3/12$, and therefore the final parameters to be determined for the haltere are w and h . Using a width of $w = 0.5 \text{ mm}$ and a thickness of $h = 50 \mu\text{m}$ ($z = h/2 = 25 \mu\text{m}$), along with the generated Coriolis force on the haltere gives the minimum strain $\epsilon_{min} = 2.26 \times 10^{-6}$ which is above the noise floor for a Techkor 9000s strain gauge signal conditioner (approximately 1×10^{-6}). Additionally, from Equation (4.5), the stiffness in the tangential direction is 100 times greater than the stiffness in the lateral direction. For actuation, the haltere is connected directly to the free end of a cantilevered PZT unimorph. This is done in such a way that the Q of the haltere is sufficiently high to allow for greater motion than that of the PZT alone.

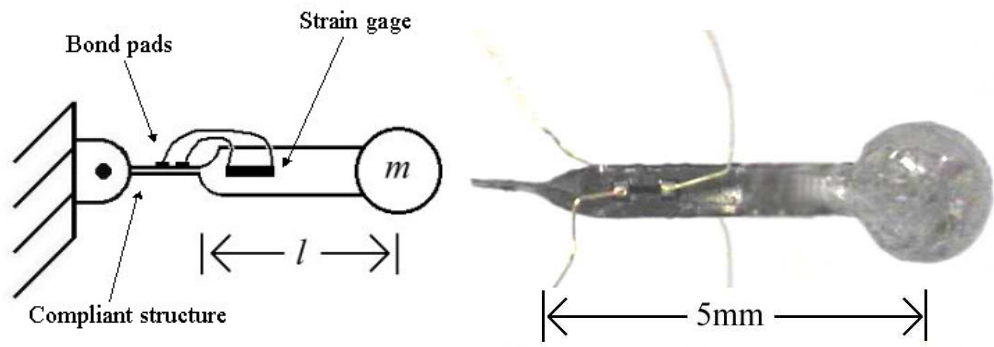


Figure 4.8: Schematic of the simple vibrating haltere (*left*). Photo of the completed haltere with half bridge strain sensor and its wires (*right*).

The last design issue is how to orient the strain gauges and deal with their wires. Since the gauges are extremely sensitive to thermal drifts, a full *Wheatstone* bridge is the most desirable configuration for the sensors. However, because of the limited surface area of the haltere, only a half bridge is possible. This is done by placing one gauge on either side of the beam so that one sensor would be in compression while the other is in tension. The main concern with the gauge placement is successfully using the delicate gold leads to bring the signal off the haltere while not damaging them or adding additional parallel stiffness to the structure. This is done by placing bond pads on the compliant end of the haltere. The lead wires are fixed to these pads and more sturdy wire is coiled and connected to the pads.

The right panel of Figure 4.8 shows the completed haltere.

To test this haltere structure, it is setup on a servo motor, oriented such that the haltere is along the axis of rotation of the motor (see the left panel of Figure 4.9). Much care is taken to ensure that the haltere is aligned directly along the axis of rotation such that when there is an applied angular velocity, the inertial force of the haltere structure would not interfere with the sensed signal. The servo motor has an angular velocity range of approximately $0.1\text{--}10\text{ rad/s}$. Ideally, the motor would be allowed to freely rotate for the haltere to sense a pure angular velocity. However, for wiring concerns, the range of motion needs to be restricted. The right panel of Figure 4.9 shows the measured angular velocity and the angular velocity of the motor. The measured signal is demodulated using the proposed demodulation technique. First, the signal is multiplied with a unity magnitude *sine* wave of precisely the haltere frequency and phase. Note that the haltere phase is not measured directly because position sensors for the haltere are difficult to implement on such a small scale. Instead, the actuator phase is measured, and since the haltere is at resonance, it is assumed that its phase lags 90° behind that of the actuator. Then, this demodulated signal is filtered with a third order *Butterworth* low pass filter with a cutoff frequency of 4 Hz to eliminate remaining high frequency noise.

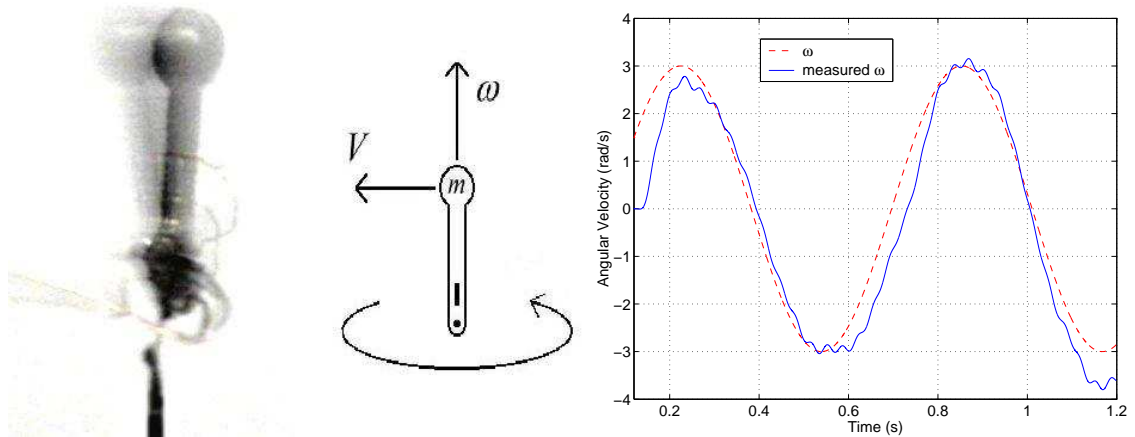


Figure 4.9: Test setup for the simple vibrating haltere (*left*). Angular velocity detection by the simple vibrating haltere (*right*).

4.3.2 Fourbar-actuated Haltere

The design of the second haltere is similar to the design of the MFI thorax structure as described in [28]. Instead of driving the haltere from a vibrating structure, it is placed on the output link of a mechanically amplifying fourbar structure, as illustrated in Figure 4.10. The haltere is constructed by laser micromachining a stainless steel to the desired dimensions and depositing a metal to the distal end to create a mass. Strain gauges are attached to the proximal end of the haltere and connected using insulated $25\ \mu m$ ribbon cable. The completed haltere is then attached to the transmission system. The fourbar and slider-crank mechanisms take the small linear displacement of the actuator and transform this into large angles at the output [28, 113]. This technique gives better control over the motion of the haltere, allowing for large stroke amplitudes at high resonant frequencies. Since the Coriolis force acting on the haltere mass is proportional to the haltere velocity, this method of actuation should give greater sensitivity for detection of body angular velocity.

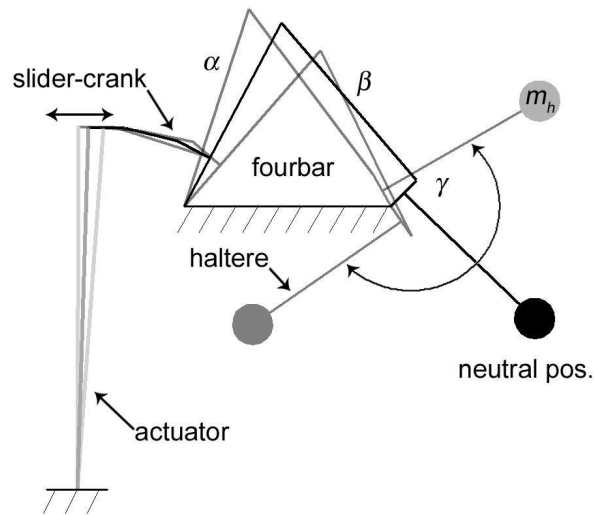


Figure 4.10: Schematic of the fourbar actuated haltere. Courtesy of R.J. Wood.

Assuming similar kinematic and dynamic constraints as the MFI thorax, 120° stroke amplitude at $150\ Hz$, and resolution constraints for sensing the forces, there are again four parameters to be determined. Three geometric parameters and the mass of the haltere are constrained by four defining equations. First, it is desired that the stiffness in the lateral direction of the haltere is significantly higher than the drive frequency so that the lateral resonant mode is not excited during actuation. Setting the lateral resonant

frequency at 500 Hz gives the following:

$$2\pi \cdot 500 = \sqrt{\frac{k_l}{m}} = \sqrt{\frac{Ewh^3}{4l^3m}} \quad (4.7)$$

where k_l is the stiffness in the lateral direction, m is the mass of the haltere (again assumed to be greater than the mass of the cantilever), E is the Young's modulus of the material used, and w , h , and l are the width, thickness, and length of the cantilever, respectively. Next, the minimum detectable Coriolis force is given as a function of the minimum detectable strain.

$$F_{Coriolis, min} = \frac{Ewh^2}{6l} \epsilon_{min} \quad (4.8)$$

For the given kinematic parameters and the desired drive frequency, the haltere velocity is $200\pi \cdot l$. Now from Equation (4.1), the minimum detectable Coriolis force can be related to the minimum detectable angular velocity (again assumed to be 1 rad/s) by the following:

$$F_{Coriolis, min} = 2m\omega_{min} \cdot v = 400\pi \cdot m \cdot l \quad (4.9)$$

Equating Equations (4.8) and (4.9) gives the following:

$$Ewh^2 \epsilon_{min} = 2400\pi \cdot m \cdot l^2 \quad (4.10)$$

where the minimum detectable strain is a known parameter. The last constraint is from the dynamics of the MFI thorax and is based upon the desired MFI wing inertia. To obtain the same resonance frequency as the MFI wing beat, the inertia of the haltere given by the following:

$$J_{haltere} = m \cdot l^2 \quad (4.11)$$

is set to $10 \text{ mg}\cdot\text{mm}^2$ which is about half the wing inertia [113] because a single fourbar will have half the parallel stiffness as the dual fourbar in the two degree-of-freedom thorax. Choosing $w = 1 \text{ mm}$ because of geometric constraints of the fourbar gives three unknown parameters to be solved from Equations (4.7), (4.10), and (4.11). However, the constraint from Equation (4.11) is relaxed for the current implementation of the prototype haltere since it can not be satisfied. Therefore, choosing $m = 4 \text{ mg}$, $l = 5 \text{ mm}$, and $h = 50 \mu\text{m}$ gives a close fit to the remaining two constraints, while still considering construction difficulties. After construction, the haltere resonant frequency is found to be 70 Hz , at a stroke amplitude of 90° . This haltere structure can be seen in Figure 4.11.

The fourbar driven haltere is tested in a similar manner to the simple vibrating haltere. However, to obtain a smoother angular velocity, the structure is placed on a

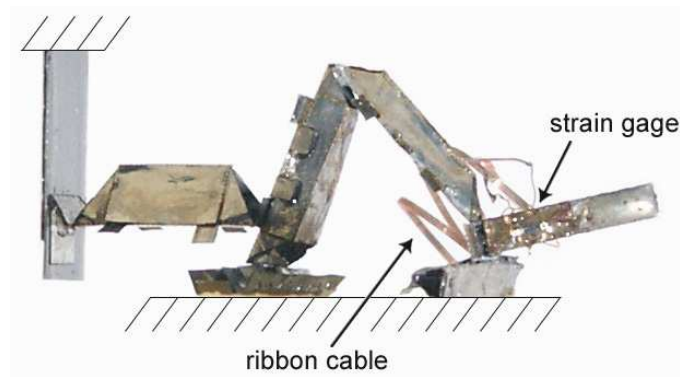


Figure 4.11: Photo of the completed fourbar actuated haltere.

damped harmonic oscillator. The position of the structure on the oscillator is determined by using high-speed video footage and some simple image processing. The results are seen in Figure 4.12. One key difference between the two haltere structures is that with the fourbar driven structure, the position of the haltere can be sensed using actuator-mounted strain sensors as described in [110]. After testing, this position is normalized to yield a unity magnitude *sine* wave which represents the haltere phase. This is then used to demodulate the signals using the same demodulation scheme.

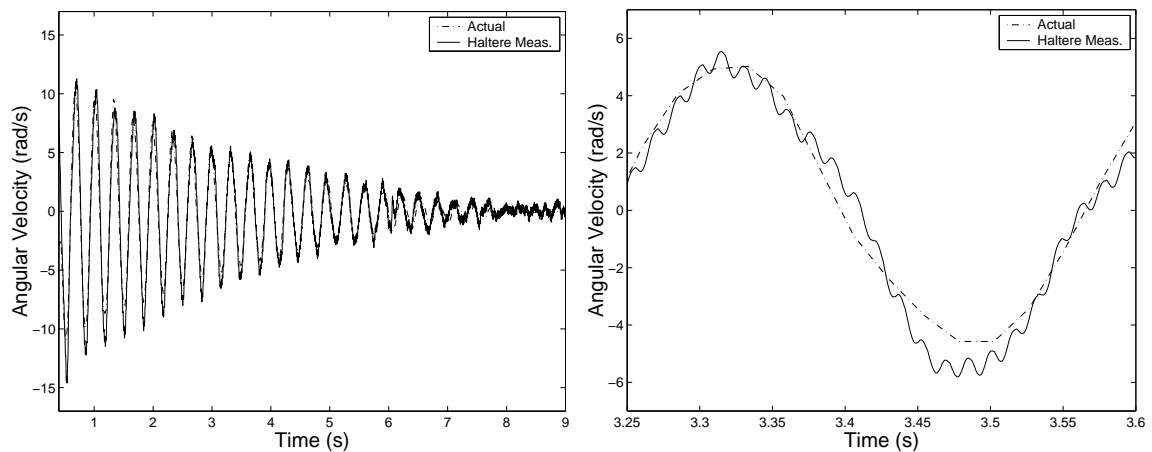


Figure 4.12: Angular velocity detection by the fourbar actuated haltere (*left*). Zoomed in to show accuracy (*right*).

4.4 Attitude Stabilization for the MFI Using Ocelli and Halteres

Thus far, four individual sensory systems (optic flow sensors, ocelli, magnetic field sensors, and halteres) have been presented and their contributions to insect flight have been discussed. In order to perform complex behaviors, such as navigation and search, real insects depend on the synergistic interaction of signals from various sensory modalities. Research on sensor integration in insects revealed several instances in which signals from different sense organs are combined to generate behavioral responses that are accurate and reliable. For examples, bees and ants are able to navigate by dead reckoning, a process whereby information on heading direction (obtained from the celestial compass) is combined with information on distance travelled to estimate an animal's position relative to its nest in terms of distance and direction [26, 89]. For *Drosophila*, visuo-olfactory integration is particularly important for search behavior. They readily localize an odor source against a textured background, but fail to do so when the target is presented within a uniform visual surround [31, 32]. In cicadas *Magicicada cassini*, visual and phonotactic orientation occur simultaneously for synchronized adult emergence and aggregation of millions of individuals during feeding, chorusing, and mating [60].

In this section, a simple example of sensor integration for the insect flight control is presented. Specifically, an attitude stabilization law, using the outputs from the ocelli and halteres, is proposed to align the z -axis of the body frame of a flying insect with the z -axis of the fixed frame. To this end, the dynamics of the attitude of a flying insect are modeled as follows [78]:

$$\begin{aligned}
 \dot{R} &= R\hat{\omega}^b \\
 \dot{\omega}^b &= J_{body}^{-1}(\tau^b - \omega^b \times J_{body}\omega^b) \\
 \tau^b &= \mathbf{u} \\
 \hat{\omega}^b &= \begin{bmatrix} 0 & \omega_z^b & -\omega_y^b \\ -\omega_z^b & 0 & \omega_x^b \\ \omega_y^b & -\omega_x^b & 0 \end{bmatrix}
 \end{aligned} \tag{4.12}$$

where R is the body rotation matrix, $\omega^b = [\omega_x^b, \omega_y^b, \omega_z^b]^T$ is the angular velocity of the insect body relative to the body frame, $\tau^b \in \mathbb{R}^3$ is the total external torque relative to the body frame attached to the center of mass of the insect body, $J_{body} \in \mathbb{R}^{3 \times 3}$ is the moment of inertia of the insect body relative to the body frame, and $\mathbf{u} \in \mathbb{R}^3$ is the control input

vector.

The z -axes of the body and fixed frames are aligned if and only if the angle, θ , between them is zero. This angle can be computed from the rotation matrix, R , by recalling that the cosine of the angle between two unit vectors is given by their inner product, i.e., $\cos \theta = \mathbf{e}_3^T P_z^a = \mathbf{e}_3^T R \mathbf{e}_3 = r_{33}$ where P_z^a represents the z -axis unit vector of the body frame relative to the fixed frame. Based on the idea that the insect would rotate its body such that the angle θ_z would decrease, the input torque is given by the following:

$$\mathbf{u} = -k_\theta [y_2^o, -y_1^o, 0]^T - k_\omega [y_1^h, y_2^h, y_3^h]^T \quad (4.13)$$

where k_θ and k_ω are scalar, y_1^o and y_2^o are the outputs from the ocelli in Equations (3.6), and y_1^h , y_2^h , and y_3^h are the haltere outputs in Equations (4.4). This control law stabilizes the insect orientation as shown in the following theorem [79]:

Theorem 4.4.1. *If the light intensity function is $I = f(\theta) = \cos(\theta)$ and $k_\theta, k_\omega > 0$, then the control law (4.13) aligns the z -axes of the fixed and body frames, i.e., all trajectories of System (4.12) approach the set $M = \{(R, \boldsymbol{\omega}) \mid P_z^b = (0, 0, \pm 1), \boldsymbol{\omega} = 0\}$. However, only the point $M_1 = \{(R, \boldsymbol{\omega}) \mid P_z^b = (0, 0, 1), \boldsymbol{\omega} = 0\}$ is locally asymptotically stable.*

This theorem states that a simple proportional feedback law of the ocelli and haltere outputs can steer the insect orientation such that the z -axis of the body frame will always point toward the light source, i.e., the point M_1 , regardless of the initial condition. Although from a theoretical point of view some trajectories converge to the point M_2 , in practice all trajectories converge to the stable point M_1 since M_2 is unstable. Theorem 4.4.1 can be generalized to simply monotonically decreasing light intensity function although it is necessary to add an additional constraint [79].

Theorem 4.4.2. *If the intensity function $I = f(\theta)$ is a differentiable, monotonically decreasing function, then there exist positive constants $\lambda > 0$ such that for $(k_\omega > \lambda k_\theta > 0)$, the control law (4.13) aligns the z -axes of the fixed and body frames, i.e., all trajectories of System (4.12) approach the set $M = \{(R, \boldsymbol{\omega}) \mid P_z^b = (0, 0, \pm 1), \boldsymbol{\omega} = 0\}$. However, only the point $M_1 = \{(R, \boldsymbol{\omega}) \mid P_z^b = (0, 0, 1), \boldsymbol{\omega} = 0\}$ is locally asymptotically stable.*

Theorem 4.4.2 states that if the damping gain k_ω is sufficiently large and the dynamics of the insect is slow enough, the field generated by the ocelli feedback $\mathbf{u}_\theta = -k_\theta [y_2^o, -y_1^o, 0]^T$ steers in practice all trajectories toward the stable orientation M_1 . It is remarkable that a simple proportional feedback control law based on the ocelli and haltere

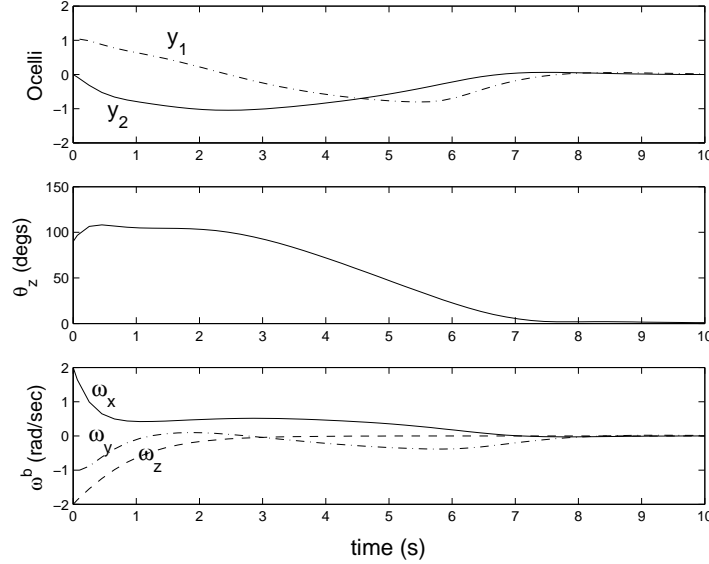


Figure 4.13: Simulation result of insect dynamics using control law (4.13). It can be seen that the insect stabilizes toward the orientation of the light source (i.e., $\theta_z = 0$ and $\boldsymbol{\omega} = [0, 0, 0]^T$).

outputs can reorient the insect toward the light source without knowing the exact light intensity function or the ocelli latitude. Moreover, the set of stabilizing gains (k_θ , k_ω) can be optimized with respect to some performance metrics, such as settling time or minimal input torque.

Simulation of control law (4.13) with light intensity function $I = \cos^5 \theta$ and initial conditions ($\theta_z = \pi/2$, $\boldsymbol{\omega} = [2, -1, -2]^T$) is shown in Figure 4.13. As expected, the angle between the z -axes of the fixed and body frames as well as the insect angular velocities and the ocelli outputs go to zero.

Control law (4.13) is very attractive for three main reasons. First, it is *simple*: the input control is simply some proportional feedback of the sensor outputs. This is very important in terms of the implementation of control laws for micro robots since they have very limited computational power. Second, it is *robust*: despite its simplicity, this control law does not depend on the exact light intensity function, as long as it is a monotonically decreasing function of the latitude. Finally, it is *globally stabilizing*: remarkably, this control law guarantees the alignment of the insect vertical axis with the light source from any initial condition including the upside down orientation which is likely to occur in the presence of strong wind gusts.

4.5 Chapter Summary and Discussion

In this chapter, the mechanism by which real flying insects use to detect body angular velocities are modeled and simulated. The result suggests that it is possible to build an angular rate sensor based upon such a biological mechanism. The haltere sensor, mimicking the haltere of real flies, comprises of a mass at the tip of a compliant beam. It oscillates up and down at a high frequency so that when there is an applied angular velocity to the sensor, there will be the Coriolis force exerted on the mass. The haltere sensor measures this Coriolis force using strain gauges at its base. By exploiting the characteristics (i.e., frequency, phase, and modulation) of the Coriolis force signal, the applied angular velocity can be extracted from the measured signals. Two types of biomimetic halteres have been constructed and tested. The first device is connected directly to a compliant cantilever driven by a piezoelectric actuator. The second device is placed on a mechanically amplifying fourbar structure driven by a piezoelectric actuator. Experiments on both devices demonstrate successful measurements of the applied angular velocities. Although test on rotations about one axis is performed, the haltere sensors are capable of detecting rotations about two independent axes in the haltere stroke plane using the proposed demodulation scheme.

Making a gyroscope based on a biological mechanism by itself is not a big gain. However, there are several advantages for a robotic flying insect in using halteres instead of MEMS gyroscopes as angular rate sensors. First, the haltere uses very little power because it might not need active actuation. Being designed as a high Q system, the haltere can be driven parasitically from the body vibrations of the robotic flying insect. Second, the haltere has a large dynamic range. It can detect angular velocities from as low as tens of degrees per second to as high as thousands of degrees per second, which is often encountered during sharp turns of flying insects. Finally, when the wings of a flying insect are flapping, the wing inertia will cause the insect body to oscillate along an axis parallel to the wing stroke direction. The haltere can reduce the error caused by these common-mode oscillations by phase-locking to the wing in the stroke plane. Table 4.1 gives a comparison of the fourbar-actuated haltere to commercially-available MEMS gyroscopes.

At the end of the chapter, a sensor integration strategy is investigated. A close-loop control law using the outputs from the halteres and ocelli as feedback is proposed to stabilize the attitude of a flying insect. It has been shown that this control technique is able to steer the insect such that the vertical axis of the insect body is aligned with the

	Haltere ¹	ADXRS300 ²	KGF01-1002 ³	Silicon MicroRing Gyro ⁴
Weight (<i>mg</i>)	30 ⁵	< 500 ⁶	< 600 ⁷	< 600 ⁷
Sensitivity ($\frac{mV}{\circ/s}$)	0.1	5.0	8.0	25.0
Max Rate (\circ/s)	$\pm 300,000$	± 300	± 250	± 60
Bandwidth (<i>Hz</i>)	15	40	75	10
Power (<i>mW</i>)	1	30	125	75
Sensing Axis	Dual	Single	Single	Single

1. Assuming parasitic drive and 1% duty cycle strain gauge sampling.
2. Analog Devices, Inc., <http://www.analog.com/>
3. Kionix, Inc., <http://www.kionix.com/>
4. MicroSensors, Inc., <http://www.microsensors.com/>
5. Including the weight of the fourbar structure.
6. Including the weight of the 16-pin BGA surface-mount package ($7mm \times 7mm \times 3mm$).
7. Including the weight of the 24-pin SOIC package ($7.52mm \times 15.36mm \times 2.35mm$).

Table 4.1: Comparison of the fourbar-actuated haltere to commercially-available silicon micromachined angular rate sensors.

direction of the light source regardless of the initial body orientation and angular velocities, as long as the light intensity distribution of the surrounding is a monotonically decreasing function of the latitude. The presented sensor integration scheme is promising because it not only is simple, in terms of sensor architectures and proportional feedback control, to be implemented on a robotic flying insect, but also can achieve robust global stability while directing the insect toward the orientation of the light source.

Chapter 5

Conclusions

Despite the limited neural processing power, flying insects exhibit excellent capabilities in traversing constricted environments. This is due not only to the exceptional flight maneuverability, but also to a set of simple and effective sensory systems. In this dissertation, the sensing mechanisms of compound eyes, ocelli, and halteres of a fly were described and based on these biological principles, formal models of biomimetic sensors were developed. The optic flow sensor, consisting of an array of EMDs using the delay-and-correlate algorithm, detects optic flow in the visual field to estimate the insect's self-motion and to track moving objects in the environment. The ocelli sensor, consisting of four photoreceptors facing at different orientations, compares the light intensity measured by the pairwise photoreceptors to estimate the insect's body attitude with respect to a light source. The haltere sensor, consisting of a mass at the tip of a cantilever oscillating at a high frequency, detects the Coriolis force produced by the insect's rotational motion to decipher the angular velocities of the insect. Using the proposed models of these sensors, it is possible to recreate, in simulation, a number of interesting insect flight behaviors including centering response, obstacle avoidance, terrain following, and phototactical reactivity for the MFI. It is also remarkable that many of these behavioral responses can be reproduced using simple control schemes such as proportional feedback control and switching control. An example of attitude stabilization was given in which a close-loop control law using outputs from the ocelli and halteres as feedback could stabilize the MFI toward the upright posture from any initial body orientation and angular velocities.

While the simulation showed the feasibility of using biological sensing mechanisms for flight control of the MFI, prototypes of these biomimetic sensors were constructed and

tested. To its simplest form, the optic flow sensor contained a two-by-two array of photodiodes soldered onto a millimeter-scale circuit board. When a black stripe was moved across the receptive field of the sensor, signals from the individual photodiodes were recorded and processed off-line using the delay-and-correlate operation. The result showed an excellent measurement of optic flow induced by the black stripe and hence demonstrating the sensor's ability to detect moving objects. The ocelli sensor used four photodiodes, each of these was soldered onto one face of a square pyramidal structure. The sensor was rotated under a light source and signals from the photodiodes were recorded. The pairwise subtraction of the opposing signals exhibited a monotonic correlation with the rotation angle, allowing the estimation of the sensor's orientation with respect to the light source. The haltere sensor was a piezoelectrically actuated vibrating cantilever with a mass at the distal end. Two strain gauges were placed, one on either side of the cantilever, at the proximal end to measure the strain in the structure as the Coriolis force causes the haltere to deviate from its stroke plane. Using the proposed demodulation scheme, the haltere sensor was able to detect angular velocities generated by a servo motor and by a harmonic oscillator. In addition to the three biomimetic sensors, a magnetic field sensor consisting of three metal loops was designed to imitate the magnetoreception in real insects. This sensor would allow the MFI to reference directional information during navigation.

Although existing off-the-shelf micro sensors have performance exceeding that of the sensors described in this dissertation, the figure of merit here is that without complex device structure and extensive signal processing, these biomimetic sensors are still capable of providing adequate sensory information for flight control of a robotic flying insect. They also exhibit some features that are particularly appropriate for the MFI. The halteres have high sensitivity at high angular rates ($> 1000^\circ/s$) which are often encountered during saccades. Furthermore, these sensors dissipate very little power. The ocelli essentially use no power. The halteres will not need active actuation when mounted on the MFI airframe because small body vibrations should be sufficient to excite this high Q system.

5.1 Future Direction

While the preliminary results of these prototype sensors showed promising performance, the next step will be to incorporate these sensors to the MFI in order to investigate their performance on a flapping robotic platform. To do this, it is necessary to further reduce the size and weight of these devices. This can be done without significant revisions

to the design of the devices. Integration of these sensors to the MFI will also allow different control strategies to be evaluated using outputs from these sensors. Moreover, two halteres should be used together and oriented in such a way that the three body angular velocities can be detected.

Another important issue regarding insect flight is how to combine sensory information from different sensory modalities to assist in flight control and navigation. Although there has been extensive research on the sensory motor reflexes involving a single sensory system, less is known about the convergence of multiple sensory modalities onto a common motor pathway. Experiments on insect behavior and neurophysiology have revealed that halteres and ocelli mediate reflexive responses while compound eyes are used mainly for fine control in real insects, and the visual system can influence the haltere system when performing voluntary maneuvers. For the MFI, this requires implementing control algorithms that can weigh the outputs from various sensory systems differently under different situations so that the MFI can generate goal-oriented maneuvers while preserving proper equilibrium reflexes.

Bibliography

- [1] K. Abe, T. Miwa, and M. Uchiyama. Development of a 3-axis planar force/torque sensor for very small force/torque measurement. *Transaction of the Japanese Society of Mechanical Engineers*, 42(2):376–382, 1999.
- [2] E.H. Adelson and J.R. Bergen. Spatiotemporal energy models for the perception of motion. *Journal of the Optical Society of America A*, 2(2):284–299, 1985.
- [3] A.G. Andreou and K. Strohhahn. Analog VLSI implementation of the Hassenstein-Reichardt-Poggio models for vision computation. In *Proceedings of IEEE International Conference on Systems, Man and Cybernetics*, pages 707–710, New York, NY, 1990.
- [4] A.N. Banks and R.B. Srygley. Orientation by magnetic field in leaf-cutter ants, *Atta colombica* (Hymenoptera: Formicidae). *Ethology*, 109:835–846, 2003.
- [5] H.M. Barkla and L.J. Auchterlonie. The Magnus or Robins effect on rotating spheres. *Journal of Fluid Mechanics*, 47:437–447, 1971.
- [6] H.B. Barlow and W.R. Levick. The mechanism of directionally selective units in the rabbit’s retina. *Journal of Physiology*, 178:447–504, 1965.
- [7] G. Barrows and C. Neely. Mixed-mode VLSI optic flow sensors for in-flight control of a micro air vehicle. *Proceedings of SPIE, Critical Technologies for the Future of Computing*, 4109:52–63, November 2000.
- [8] V. Beroulle, Y. Bertrand, L. Latorre, and P. Nouet. Test and testability of a monolithic MEMS for magnetic field sensing. *Journal of Electronic Testing: Theory and Applications*, 17:439–50, 2001.

- [9] A. Bicchi, A. Caiti, and D. Prattichizzo. Optimal design of a multi-axis force/torque sensor. In *Proceedings of the IEEE International Conference on Decision and Control*, pages 2981–2986, Phoenix, AZ, December 1999.
- [10] F. Bohorquez, P. Samuel, J. Sirohi, D. Pines, L. Rudd, and R. Perel. Design, analysis and performance of a rotary wing MAV. *Journal of the American Helicopter Society*, 48(2):80–90, April 2003.
- [11] A. Borst and S. Bahde. Visual information processing in the fly’s landing system. *Journal of Comparative Physiology A*, 163:167–173, 1988.
- [12] A. Borst and M. Egelhaaf. Principles of visual motion detection. *Trends in Neuroscience*, 12(8):297–306, 1989.
- [13] J. Chahl, S. Thakoor, N. Le Bouffant, G. Stange, M. V. Srinivasan, B. Hine, and S. Zornetzer. Bioinspired engineering of exploration systems: A horizon sensor/attitude reference system based on the dragonfly ocelli for Mars exploration applications. *Journal of Robotic Systems*, 20(1):35–42, January 2003.
- [14] J.S. Chahl and M.V. Srinivasan. Reflective surfaces for panoramic imaging. *Applied Optics*, 36:8275–8285, 1997.
- [15] W.P. Chan, F. Prete, and M.H. Dickinson. Visual input to the efferent control system of a fly’s “gyroscope”. *Science*, 280:289–292, April 1998.
- [16] R.F. Chapman. *The Insects: Structure and Function*. Cambridge University Press, New York, fourth edition, 1998.
- [17] P.B. Cornwell. The functions of the ocelli of *Calliphora* (Diptera) and *Locusta* (Orthoptera). *Journal of Experimental Biology*, 32:217–237, 1955.
- [18] A. Cox, D.J. Monopoli, M. Goldfarb, and E. Garcia. Development of piezoelectrically actuated micro-aerial vehicles. In *SPIE Microrobotics and Microassembly*, pages 101–108, Boston, MA, September 1999.
- [19] C.T. David. Compensation for height in the control of groundspeed by *Drosophila* in a new, ‘Barber’s Pole’ wind tunnel. *Journal of Comparative Physiology A*, 147:485–493, 1982.

- [20] M.H. Dickinson. Haltere-mediated equilibrium reflexes of the fruit fly, *Drosophila melanogaster*. *Philosophical Transactions of the Royal Society of London B*, 354:903–916, 1999.
- [21] M.H. Dickinson, F.-O. Lehmann, and S.P. Sane. Wing rotation and the aerodynamic basis of insect flight. *Science*, 284(5422):1954–1960, June 1999.
- [22] M.H. Dickinson, L.F. Tammervo, and M. Tarstino. Sensory fusion in free-flight search behavior of fruit flies. In J.L. Davis, A. Rudolph, and J. Ayers, editors, *Neurotechnology for Biomimetic Robots*, pages 573–591. The MIT Press, Cambridge, MA, 2002.
- [23] M. Egelhaaf and A. Borst. Transient and steady-state response properties of movement detectors. *Journal of the Optical Society of America A*, 6:116–127, 1989.
- [24] M. Egelhaaf, A. Borst, and W. Reichardt. Computational structure of a biological motion-detection system as revealed by local detector analysis in the fly’s nervous system. *Journal of the Optical Society of America A*, 6(7):1070–1087, 1989.
- [25] C.P. Ellington, C. van den Berg, A.P. Willmott, and A.L.R. Thomas. Leading-edge vortices in insect flight. *Nature*, 384:626–630, December 1996.
- [26] H. Esch and J. Burns. Distance estimation by foraging honeybees. *Journal of Experimental Biology*, 199:155–162, 1996.
- [27] A. Fayyazuddin and M.H. Dickinson. Haltere afferents provide direct, electrotonic input to a steering motor neuron of the blowfly, *Calliphora*. *Journal of Neuroscience*, 16(16):5225–5232, August 1996.
- [28] R.S. Fearing, K.H. Chiang, M.H. Dickinson, D.L. Pick, M. Sitti, and J. Yan. Wing transmission for a micromechanical flying insect. In *Proceedings of the IEEE International Conference on Robotics and Automation*, pages 1509–1516, San Francisco, CA, April 2000.
- [29] G. Fraenkel and J.W.S. Pringle. Halteres of flies as gyroscopic organs of equilibrium. *Nature*, 141:919–921, 1938.
- [30] M.O. Franz and H.G. Krapp. Wide-field, motion-sensitive neurons and matched filters for optic flow fields. *Biological Cybernetics*, 83:185–197, 2000.

- [31] M.A. Frye and M.H. Dickinson. Motor output reflects linear superposition of visual and olfactory input in *Drosophila*. *Journal of Experimental Biology*, 207:123–131, 2004.
- [32] M.A. Frye, M. Tarsitano, and M.H. Dickinson. Odor localization requires visual feedback during free-flight in *Drosophila melanogaster*. *Journal of Experimental Biology*, 206(5):843–855, 2003.
- [33] J.M. Grasmeyer and M.T. Keennon. Development of the Black Widow micro air vehicle. Presented at the 39th AIAA Aerospace Sciences Meeting and Exhibit, AIAA Paper No. AIAA-2001-0127, Reno, NV, January 2000.
- [34] W.E. Green, P.Y. Oh, K. Sevcik, and G. Barrows. Autonomous landing for indoor flying robots using optic flow. In *ASME Proceedings of International Mechanical Engineering Congress*, Washington, DC, November 2003.
- [35] J. Haag and A. Borst. Encoding of visual motion information and reliability in spiking and graded potential neurons. *Journal of Neuroscience*, 17:4809–4819, 1997.
- [36] R.R. Harrison. *An analog VLSI motion sensor based on the fly visual system*. PhD thesis, California Institute of Technology, Pasadena, May 2000.
- [37] B. Hassenstein and W. Reichardt. Systemtheoretische analyse der Zeit-, Reihenfolgen- und Vorzeichenbewertung bei der Bewegungsperzeption des Rüsselkäfers *Chlorophanus*. *Z. Naturforsch.*, 11b:513–524, 1956.
- [38] D.J. Heeger. Model for the extraction of image flow. *Journal of the Optical Society of America A*, pages 1455–1471, 1987.
- [39] R. Hengstenberg. Mechanosensory control of compensatory head roll during flight in the blowfly *Calliphora erythrocephala* Meig. *Journal of Comparative Physiology A*, 163:151–165, 1988.
- [40] R. Hengstenberg. Gaze control in the blowfly *Calliphora*: a multisensory, two-stage integration process. *Neuroscience*, 3:19–29, 1991.
- [41] C.M. Higgins and C. Koch. A modular multi-chip neuromorphic architecture for real-time visual motion processing. *Analog Integrated Circuits and Signal Processing*, 24(3):195–211, September 2000.

- [42] G.A. Horridge and L. Marcelja. On the existence of fast and slow directionally sensitive motion detector neurons in insects. *Proceedings of the Royal Society of London B*, 248(1321):47–54, 1992.
- [43] SRI International. Artificial muscle transducers. Available online at <http://www.sri.com/esd/automation/actuators.html>.
- [44] W.L. Jongebloed, E. Rosenzweig, D. Kalicharan, J.J.L. van der Want, and J.S. Ishay. Ciliary hair cells and cuticular photoreceptor of the hornet *Vespa orientalis* as components of a gravity detecting system: an SEM/TEM investigation. *Journal of Electron Microscopy*, 48(1):63–75, 1999.
- [45] G. Kastberger. The ocelli control the flight course in honeybees. *Physiological Entomology*, 15:337–346, 1990.
- [46] G. Kastberger and K. Schuhmann. Ocellar occlusion effect on the flight behavior of homing honeybees. *Journal of Insect Physiology*, 39(7):589–600, 1993.
- [47] J.L. Kirschvink. The horizontal magnetic dance of the honeybee is compatible with a single-domain ferromagnetic magnetoreceptor. *Biosystems*, 14(2):193–203, 1981.
- [48] T.J. Koo, B. Sinopoli, A. Sangiovanni-Vincentelli, and S. Sastry. A formal approach to reactive system design: A UAV flight management system design example. In *Proceedings of IEEE International Symposium on Computer-Aided Control System Design*, Kohala Coast, HI, 1999.
- [49] H.G. Krapp and R. Hengstenberg. Estimation of self-motion by optic flow processing in single visual interneurons. *Nature*, 384:463–466, 1996.
- [50] I. Kroo et al. The mesicopter: A meso-scale flight vehicle. Available online at <http://aero.stanford.edu/mesicopter/>.
- [51] T. Labhart. How polarization-sensitive interneurons of crickets perform at low degrees of polarization. *Journal of Experimental Biology*, 199:1467–1475, 1996.
- [52] M.F. Land. Visual acuity in insects. *Annual Review of Entomology*, 42:147–177, 1997.
- [53] S.C. Liu. A neuromorphic aVLSI model of global motion processing in the fly. *IEEE Transactions on Circuits and Systems II: Analog and Digital Signal Processing*, 47(12):1458–1467, December 2000.

- [54] S.C. Liu and A. Usseglio-Viretta. Fly-like visuomotor responses of a robot using aVLSI motion-sensitive chips. *Biological Cybernetics*, 85:449–457, 2001.
- [55] L. Matthies, E. Gat, R. Harrison, B. Wilcox, R. Volpe, and T. Litwin. Mars microrover navigation: performance evaluation and enhancement. *Autonomous Robots*, 2:291–311, 1995.
- [56] J.M. McMichael and M.S. Francis. Micro air vehicles - toward a new dimension in flight. *Unmanned Systems*, 15(3):10–17, 1997.
- [57] C. Mead. *Analog VLSI and neural systems*. Addison-Wesley, Reading, Massachusetts, 1989.
- [58] R.C. Michelson. The entomopter. In J.L. Davis, A. Rudolph, and J. Ayers, editors, *Neurotechnology for Biomimetic Robots*, pages 481–509. The MIT Press, Cambridge, MA, 2002.
- [59] A. Moini. *Vision chips*. Kluwer Academic, Boston, Massachusetts, 2000.
- [60] T.E. Moore, F. Huber, T. Weber, U. Klein, and C. Bock. Interaction between visual and phonotactic orientation during flight in *Magicalicada cassini* (Homoptera: Cicadidae). *The Great Lakes Entomologist*, 26(3):199–221, 1993.
- [61] K. Nakayama. Biological image motion processing: a review. *Vision Research*, 25:625–660, 1985.
- [62] G. Nalbach. The halteres of the blowfly *Calliphora*: I. kinematics and dynamics. *Journal of Comparative Physiology A*, 173(3):293–300, 1993.
- [63] G. Nalbach. Extremely non-orthogonal axes in a sense organ for rotation: behavioural analysis of the dipteran haltere system. *Neuroscience*, 61(1):149–163, 1994.
- [64] G. Nalbach and R. Hengstenberg. The halteres of the blowfly *Calliphora*: II. three-dimensional organization of compensatory reactions to real and simulated rotations. *Journal of Comparative Physiology A*, 175(6):695–708, 1994.
- [65] D.C. O’Carroll, N.J. Bidwell, S.B. Laughlin, and E.J. Warrant. Insect motion detectors matched to visual ecology. *Nature*, 382(6586):63–66, 1996.

- [66] P.Y. Oh, W.E. Green, and G. Barrows. Closed quarter aerial robot prototype to fly in and around buildings. In *Proceedings of International Conference on Computer, Communication and Control Technologies*, pages 302–307, Orlando, FL, July 2003.
- [67] T.N. Pornisn-Sirirak, S.W. Lee, H. Nassef, J. Grasmeyer, Y.C. Tai, C.M. Ho, and M. Keennon. MEMS wing technology for a battery-powered ornithopter. In *Proceedings of IEEE 13th Annual International Conference on MEMS*, pages 799–804, Piscataway, NJ, January 2000.
- [68] T.N. Pornisn-Sirirak, Y.C. Tai, H. Nassef, and C.M. Ho. Titanium-alloy MEMS wing technology for a micro aerial vehicle application. *Journal of Sensors and Actuators A*, 89:95–103, March 2001.
- [69] J.W.S. Pringle. The gyroscopic mechanism of the halteres of Diptera. *Philosophical Transactions of the Royal Society of London B*, 233:347–384, 1948.
- [70] U. Rabe, K. Janser, and W. Arnold. Vibrations of free and surface-coupled atomic force microscope cantilevers: Theory and experiment. *Review of Scientific Instruments*, 67(9):3281–3293, 1996.
- [71] W. Reichardt. Autocorrelation, a principle for relative movement discrimination by the central nervous system. In W. Rosenblith, editor, *Sensory Communication*, pages 303–317. MIT Press, New York, 1961.
- [72] W. Reichardt. Movement perception in insects. In W. Reichardt, editor, *Processing of optical data by organisms and machines*, pages 465–493. Academic, New York, 1969.
- [73] W. Reichardt and M. Egelhaaf. Properties of individual movement detectors as derived from behavioural experiments on the visual system of the fly. *Biological Cybernetics*, 58(5):287–294, 1988.
- [74] R. Sahai and R.S. Fearing. Towards automatic assembly of sub-centimeter millirobot structures. In *The Third International Workshop on Microfactories*, Minneapolis, MN, September 2002.
- [75] D.C. Sandeman. Angular acceleration, compensatory head movements and the halteres of flies (*Lucilia sericata*). *Journal of Comparative Physiology*, 136:361–367, 1980.

- [76] H. Sato, T. Fukuda, F. Arai, H. Iwata, and K. Itoigawa. Analysis of parallel beam gyroscope. In *Proceedings of the IEEE International Conference on Robotics and Automation*, pages 1632–1637, Detroit, MI, May 1999.
- [77] L. Schenato, X. Deng, W.C. Wu, and S. Sastry. Virtual insect flight simulator (VIFS): a software testbed for insect flight. In *Proceedings of the IEEE International Conference on Robotics and Automation*, pages 3885–3892, Seoul, South Korea, May 2001.
- [78] L. Schenato, W.C. Wu, and S.S. Sastry. Attitude control for a micromechanical flying insect via sensor output feedback. In *The Seventh International Conference on Control, Automation, Robotic and Vision*, pages 1031–1036, Singapore, December 2002.
- [79] L. Schenato, W.C. Wu, and S.S. Sastry. Attitude control for a micromechanical flying insect via sensor output feedback. *IEEE Transactions on Robotics and Automation*, 20(1):93–106, February 2004.
- [80] H. Schuppe and R. Hengstenberg. Optical properties of the ocelli of *Calliphora erythrocephala* and their role in the dorsal light response. *Journal of Comparative Biology A*, 173:143–149, 1993.
- [81] A. Sherman and M.H. Dickinson. A comparison of visual and haltere-mediated equilibrium reflexes in the fruit fly *Drosophila melanogaster*. *Journal of Experimental Biology*, 206:295–302, 2003.
- [82] A. Sherman and M.H. Dickinson. Summation of visual and mechanosensory feedback in *Drosophila* flight control. *Journal of Experimental Biology*, 207:133–142, 2004.
- [83] S. Single and A. Borst. Dendritic integration and its role in computing image velocity. *Science*, 281(5384):1848–1850, 1998.
- [84] J. Sirohi, M. Tishchenko, and I. Chopra. Design and testing of a micro-aerial vehicle with a single rotor and turning vanes. In *Proceedings of 61st Annual Forum of the American Helicopter Society*, Grapevine, TX, June 2004.
- [85] M. Sitti, D. Campolo, J. Yan, R.S. Fearing, T. Su, and D. Taylor. Development of PZT and PZN-PT based unimorph actuators for micromechanical flapping structures. In *Proceedings of the IEEE International Conference on Robotics and Automation*, pages 3839–3846, Seoul, South Korea, May 2001.

- [86] M.V. Srinivasan. How insects infer range from visual motion. In F.A. Miles and J. Wallman, editors, *Visual Motion and its Role in the Stabilization of Gaze*, pages 139–156. Elsevier, Amsterdam, The Netherlands, 1993.
- [87] M.V. Srinivasan. Pattern recognition in the honeybee: recent progress. *Journal of Insect Physiology*, 40:183–194, 1994.
- [88] M.V. Srinivasan, J.S. Chahl, K. Weber, S. Venkatesh, M.G. Nagle, and S.W. Zhang. Robot navigation inspired by principles of insect vision. *Robotics and Autonomous Systems*, 26:203–216, 1999.
- [89] M.V. Srinivasan, J.S. Chahl, and S.W. Zhang. Robot navigation by visual dead-reckoning: Inspiration from insects. *International Journal of Pattern Recognition and Artificial Intelligence*, 11(1):35–47, 1997.
- [90] M.V. Srinivasan, M. Poteser, and K. Kral. Motion detection in insect orientation and navigation. *Vision Research*, 39:2749–2766, 1999.
- [91] M.V. Srinivasan and S.W. Zhang. Visual control of honeybee flight. In M. Lehrer, editor, *Orientation and Communication in Arthropods*, pages 95–113. Birkhauser Verlag, Basel, 1997.
- [92] M.V. Srinivasan, S.W. Zhang, M. Altwein, and J. Tautz. Honeybee navigation: Nature and calibration of the odometer. *Science*, 287:851–853, 2000.
- [93] M.V. Srinivasan, S.W. Zhang, and J.S. Chahl. Landing strategies in honeybees, and possible applications to autonomous airborne vehicles. *The Biological Bulletin*, 200:216–221, 2001.
- [94] M.V. Srinivasan, S.W. Zhang, and K. Chandrashekhara. Evidence for two distinct movement-detecting mechanisms in insect vision. *Naturwissenschaften*, 80:38–41, 1993.
- [95] M.V. Srinivasan, S.W. Zhang, M. Lehrer, and T.S. Collett. Honeybee navigation *en route* to the goal: visual flight control and odometry. *Journal of Experimental Biology*, 199:237–244, 1996.
- [96] M.V. Srinivasan, S.W. Zhang, and H. Zhu. Honeybees link sights to smells. *Nature*, 396:637–638, 1998.

- [97] R.B. Srygley and E.G. Oliveira. Sun compass and wind drift compensation in migrating butterflies. *Journal of Navigation*, 54:405–417, 2001.
- [98] L.F. Tammero and M.H. Dickinson. Collision avoidance and landing responses are mediated by separate pathways in the fruit fly, *Drosophila melanogaster*. *Journal of Experimental Biology*, 205(18):2785–2798, 2002.
- [99] L.F. Tammero and M.H. Dickinson. The influence of visual landscape on the free flight behavior of the fruit fly *Drosophila melanogaster*. *Journal of Experimental Biology*, 205(3):327–343, 2002.
- [100] C.P. Taylor. Contribution of compound eyes and ocelli to steering of locusts in flight: I. behavioural analysis. *Journal of Experimental Biology*, 93:1–18, 1981.
- [101] C.P. Taylor. Contribution of compound eyes and ocelli to steering of locusts in flight: II. timing changes in flight motor units. *Journal of Experimental Biology*, 93:19–31, 1981.
- [102] J.A. Thompson and R.S. Fearing. Automating microassembly with ortho-tweezers and force sensing. In *Intelligent Robots and Systems*, Maui, HI, 2001.
- [103] Y. Toh and H. Tateda. Structure and function of the insect ocellus. *Zoological Science*, 8:395–413, 1991.
- [104] B.A. Wandell. *Foundations of vision*. Sinauer Associates, Sunderland, Massachusetts, 1995.
- [105] Z.J. Wang, J.M. Birch, and M.H. Dickinson. Unsteady forces and flows in low Reynolds number hovering flight: two-dimensional computations *vs* robotic wing experiments. *Journal of Experimental Biology*, 207:449–460, 2004.
- [106] R. Wehner. Polarized-light navigation by insects. *Scientific American*, 23(1):106–115, 1976.
- [107] M. Wilson. The functional organization of locust ocelli. *Journal of Comparative Physiology*, 124:297–316, 1978.
- [108] R. Wolf, B. Gebhard, R. Gademann, and M. Heisenberg. Polarization sensitivity of course control in *Drosophila melanogaster*. *Journal of Comparative Physiology*, 139:177–191, 1980.

- [109] F. Wolf-Oberhollenzer and K. Kirschfeld. Motion sensitivity in the nucleus of the basal optic root of the pigeon. *Journal of Neurophysiology*, 71:1559–1573, 1994.
- [110] R.J. Wood and R.S. Fearing. Flight force measurement for a micromechanical flying insect. In *Intelligent Robots and Systems*, Maui, HI, 2001.
- [111] W.C. Wu, R.J. Wood, and R.S. Fearing. Halteres for the micromechanical flying insect. In *Proceedings of the IEEE International Conference on Robotics and Automation*, pages 60–65, Washington, DC, May 2002.
- [112] W.C. Wu, R.J. Wood, L. Schenato, and R.S. Fearing. Biomimetic sensor suite for flight control of a micromechanical flying insect: Design and experimental results. In *Proceedings of the IEEE International Conference on Robotics and Automation*, Taipei, Taiwan, September 2003.
- [113] J. Yan, R.J. Wood, S. Avadhanula, R.S. Fearing, and M. Sitti. Towards flapping wing control for a micromechanical flying insect. In *Proceedings of the IEEE International Conference on Robotics and Automation*, pages 3901–3908, Seoul, South Korea, May 2001.
- [114] J.M. Zankar, M.V. Srinivasan, and M. Egelhaaf. Speed tuning in elementary motion detectors of the correlation type. *Biological Cybernetics*, 80:109–116, 1999.
- [115] S.W. Zhang, K. Bartsch, and M.V. Srinivasan. Maze learning by honeybees. *Neurobiology of Learning and Memory*, 66(3):267–282, 1996.
- [116] L. Zhou, J.M. Kahn, and K.S.J. Pister. Corner-cube reflectors based on structure-assisted assembly for free-space optical communication. *Journal of Microelectromechanical Systems*, 12(3):233–242, June 2003.
- [117] J.C. Zufferey and D. Floreano. Fly-inspired visual steering of an ultralight indoor aircraft. *IEEE Transactions on Robotics*, 22(1):137–146, February 2006.